Novel Wing Designs for Tractor-Propeller Aircraft: Theory, CFD and Wind Tunnel Test Results

A Thesis

Submitted for the Degree of

Doctor of Philosophy

by

Rakshith Raghavan Belur

Engineering Mechanics Unit
Jawaharlal Nehru Centre for Advanced Scientific Research
(A Deemed University)
Bangalore – 560 064

JANUARY 2013

To

my wife Shwetha

and

my Parents

DECLARATION

I hereby declare that the matter embodied in the thesis entitled "**Novel Wing Designs for Tractor-Propeller Aircraft: Theory, CFD and Wind Tunnel Test Results**" is the result of investigations carried out by me at the Engineering Mechanics Unit, Jawaharlal Nehru Centre for Advanced Scientific Research, Bangalore, India under the supervision of Prof. Roddam Narasimha and Prof. Suresh Madusudhan Deshpande and that it has not been submitted elsewhere for the award of any degree or diploma.

In keeping with the general practice in reporting scientific observations, due acknowledgment has been made whenever the work described is based on the findings of other investigators.

Rakshith Raghavan Belur

CERTIFICATE

We hereby certify that the matter embodied in this thesis entitled "**Novel Wing Designs for Tractor-Propeller Aircraft: Theory, CFD and Wind Tunnel Test Results**" has been carried out by Mr. Rakshith Raghavan Belur at the Engineering Mechanics Unit, Jawaharlal Nehru Centre for Advanced Scientific Research, Bangalore, India under our supervision and that it has not been submitted elsewhere for the award of any degree or diploma.

Prof. Roddam Narasimha
(Research Supervisor)

Prof. Suresh Madusudhan Deshpande
(Research Supervisor)

List of Figures

Acknowledgements

I would like to thank *Roddam Narasimha* for being a friend, philosopher and a guide. His unending passion and a spirit of adventure towards research has helped me grow as a researcher. It was his insight that served as the building block for this dissertation. His attitude towards not only science but also towards various other things has helped me grow as an individual. I would like to thank him for that.

To *S. M. Deshpande* I am grateful for his unique, insightful discussions on topics like CFD and optimization. The wittiness in him made the interactions enjoyable, eventful and memorable.

I would like to thank *C. Praveen* for helping me develop optimization and Euler codes. I appreciate his meticulousness in writing CFD codes.

For helping me pursue my passion, I am immensely grateful to *Rama Govindarajan*.

I would like to thank *Josy P. Pullockara* for sharing the propeller slipstream data during the initial stages of this work, *Partha Mondal* for discussions on parallelization and *Allama Prabhu* for discussions on Fluent.

I would like to thank *K. Yegnanarayan* who took the initiative to set up the wind tunnel test programme. I would also like to thank the teams from C-CAD, NAL, and IISc for carrying out the wind tunnel tests.

Thanks to *Sukruth* for his help during the wind tunnel tests.

Thanks to *JNCASR*, *DST* for providing financial support for attending conferences and workshops.

Stay in JNC was indeed memorable. Thanks to -

Rahul, *Vivek*, *Aditya*, *Vini* for being partners in crime and for the fun times during my MS days. *Saikishan*, *Rajesh*, *Prasanth* for the lunch table discussions. *Ponnu* for

sponsoring my dinners during the final stages of my thesis. *Anubhab* for foodie discussions. *Sumesh, Gayathri* for their help in fixing my codes. *Sourabh* for discussions on life. *Srikanth, Subrahmanyam, Croor, Jose, Rohith, Mamta, Sunil, Shashank, Siddharth, Navaneeth, Shahjahan, Dhiraj, Milind, Chakri, Vybhav, Vishwanath, Deepak, Rohan, Ujjayan, Ashish* for making EMU eventful.

I thank *my parents* for their unconditional support and encouragement. Thanks to my brother-in-law and sister for gifting me a laptop which was used extensively for my thesis.

Finally, thanks to my wife, *Shwetha* for her sacrifices and support. I owe her big time.

Abstract

This thesis proposes novel wing designs with lower drag for propeller/rotor driven aircraft in tractor configuration with particular emphasis on a method of designing wings with lower induced drag by exploiting the propeller slipstream.

With the increasing dynamism in short-haul regional air traffic, which tends to be inherently more expensive compared to inter-continental flights on larger aircraft on a passenger-km basis, it becomes necessary to explore new designs that may cut down fuel burn. In this scenario a turboprop is a particularly attractive option, as a propeller is an inherently more efficient producer of thrust than a turbojet or even turbofan. Beginning in the early 1990's there was a decline in the usage of turboprops in civil aviation because of the availability of cheap oil, and jets have been preferred as they became affordable, faster and quieter, there is now a revival of interest in turboprops owing to climate change concerns and connectivity demands. Turboprops continue to be favoured for large cargo transport aircraft, military or civil, and for unmanned air vehicles requiring long endurance. There is therefore a need to explore new technologies associated with turboprops and other rotor-driven aircraft and optimize them for better performance. In particular, technologies associated with current propeller-driven aircraft do not take adequate account of the potential to exploit the effects of the propeller slipstream to design better wings; more generally the benefits of taking an integrated view of propeller and air frame together have not been fully realized.

The aerodynamic interaction between the propeller slipstream and the wing is of great significance, in particular when the propeller(s) is/are situated in front of the wing, as for example in a turboprop aircraft in tractor configuration. During operation propellers not only produce thrust but also accelerate and impart a swirl to the flow downstream. Due to the swirl there is an additional change in the local angle of attack of the wing. Consequently there is a corresponding deformation of the lift distribution on the wing, as a result of which the induced drag of the wing is affected.

This thesis addresses the question of exploiting the propeller slipstream for designing more efficient wings. The first step is an extension of lifting line theory to include propeller effects, and coupling it to an optimizer. For this purpose a software package that it

will be called PROWING has been developed as part of this thesis. The classical lifting line theory is modified by treating the local approach velocity, at the leading edge of the wing, as a function of the spanwise coordinate because of the presence of the slipstream. The propeller slipstream is obtained using a validated blade element module coupled to an Euler solver through a software package called PROP-EULER. Following the classical lifting line theory approach, the load distribution is expanded in Fourier series. Because of the spanwise variation of the approach velocity the number of Fourier coefficients and collocation points required to represent the load distribution accurately is much higher than usual. In the present case satisfactory results were obtained with 48 Fourier coefficients and 320 collocation points after a convergence study. During the optimization, the influence of the wing on the propeller is neglected. To generate smooth shapes and/or curves, chord and twist distributions are parameterized using Bézier curves. With a MATLAB optimizer, PROWING generates novel wing planforms which offer better aerodynamic performance such as lower drag by optimizing the chord and/or twist distributions, subject to whatever other constraints (in particular wing area and aspect ratio, but in some cases structural parameters as well) may be prescribed.

A total of 10 optimal wing planform shapes so obtained are reported in this thesis, including one in which a modest change in the planform of a wing of aspect ratio 12 is found to reduce induced drag by 9.15%. Other examples include (i) a wing in which wing thickness at two prescribed chordwise stations varies linearly in y, to accommodate spars with linearly varying depth along the span, (ii) an optimized wing with special aerofoil sections designed to ensure that no concavities occur on the upper surface of the wing, and (iii) a wing whose trailing edge is a series of straight segments. In general, all these planforms have straight leading edges and shaped trailing edges.

Amongst earlier works, those of Kroo (1986) and Veldhuis (2005) are the most relevant for the present study. Both of them suggest the inclusion of propellers in the wing design process. Kroo presents an optimization model to reduce the wing induced drag, and comments that certain changes in the propeller can also lead to better performance. His optimization model does not explore local optima en route to the global optimum which he obtains by a variational method, and does not present any specific results on wing planform. Veldhuis proposes a different optimization model using which he concludes that changing wing planform results in unrealistic optimized shapes. It is shown here that these 'unrealistic planforms' are due to certain errors in problem formulation, handling certain integrals, and in the optimization strategy adopted.

The approach followed in this thesis explores local optima in obtaining realistic wing planforms and assesses them in part by their closeness to the global optimum.

In order to assess the accuracy of the various assumptions made in PROWING lifting line solutions, the PROP-EULER code with a propeller module has been used. In this model, an Euler solution for the wing-propeller system is obtained by replacing the propeller by a rotating actuator disc in the Euler field. The Euler code uses the KFVS (Kinetic Flux Vector Splitting) scheme for the non linear term, LU-SGS (Lower Upper Symmetric Gauss Siedel) for implicitisation for faster convergence, and is parallelised using domain decomposition. The source distributions across the actuator disc are evaluated by blade element theory, for which a separate subroutine has been written and validated. This constitutes the PROP-EULER software package that has been used to obtain independent estimates of the drag of PROWING designed optimum planforms. For the wing mentioned above the induced drag reduction predicted by the PROP-EULER code is 7.9% with a mesh size of 30×10^6, which was shown to be adequate through a convergence study. This result is satisfactorily close to the value (9.15%) obtained using PROWING, demonstrating that PROWING solutions are very useful as a quick preliminary design tool.

To obtain an appreciation of viscous effects and parasite drag, RANS simulations using Fluent were also carried out. The blade element module in PROP-EULER was coupled to Fluent to model the propeller using user defined functions. The total drag reduction obtained using Fluent was 10.9 drag counts (1 drag count being 10^{-4} in C_D) whereas PROWING predicted 9.35 drag counts. (Because of the uncertainity in the prediction of absolute drag values by RANS codes, results are quoted in differential counts.)

Finally, a short wind tunnel test programme was carried out in collaboration with C-CAD (Centre for Civil Aircraft Design and Development), NAL (National Aerospace Laboratories), Bangalore, to provide proof-of-concept. The tests were conducted in the Open Circuit Wind Tunnel at IISc (Indian Institute of Science). A $1/10^{\text{th}}$ scaled model of Saras, a multipurpose civilian aircraft in the Light Transport Aircraft category designed by NAL, was used for testing. By design Saras is a pusher aircraft but, using additional mounts, it was converted into a tractor configuration. Saras has a wing span of 14.7 m, aspect ratio 8, taper ratio 0.3481 and uses Hartzell propellers. The slipstream for the Hartzell propeller was computed using the PROP-EULER code. With the original Saras wing as control, optimum planforms were designed using PROWING. The tests were conducted at a Reynolds number of 0.5×10^6 based on mean aerodynamic chord. The drag data at lift coefficients $C_L = 0$ and $C_L = 0.4$ were analysed. A rather surprising result was that the total drag on the aircraft with optimal wing was lower by 15%, appreciably better than the PROWING predicted reduction of 6.61%. Although the reasons for higher drag reduction are not entirely clear at this stage, preliminary analysis indicates two plausible

candidates: (i) the new wing has appreciably lower profile drag (by 4% or more), perhaps due to transition effects at the relatively low Reynolds numbers at which the tests were conducted, and (ii) there is constructive interference from the fuselage. The tests however leave no doubt that the optimal wing design proposed here has an improved aerodynamic performance. Investigations to explain the higher drag reduction obtained in the wind tunnel tests are being planned.

The present results thus confirm that optimum designs for turboprop wings that exploit the slipstream effect can result in significant benefits on drag, and that the mathematical model embedded in PROWING is an effective tool for preliminary design of novel, aerodynamically more efficient wing planforms.

Contents

Chapter 1
Introduction

The first powered flight way back in 1903 by the Wright Brothers used a propeller to provide thrust for the airplane. The Wright brothers realised that a propeller is essentially the same as a wing which is rotating, and used data from their earlier wind tunnel experiments on airfoils and wings for designing their propeller. They also found that twist was necessary along the propeller blade as the relative angle of attack varied along the length of the blade. The Wright Brothers used certain theoretical methods such as the blade element theory (a theory describing a mathematical model of an ideal propeller) developed in the second half of the 19th century by W. J. M. Rankine, A. G. Greenhill and R. E. Froude, to compute propulsive efficiencies for the speed regimes considered by them. Propellers became an important topic of research during the first half of the 20^{th} century. After the invention and development of the aircraft gas turbine in the 1940s, the first transport aircraft (turboprops) were driven by propellers powered by gas turbines. Later from the mid-1950s to the mid-1970s turbojet and turbofan propulsion systems became a huge success. This caused a decline in the usage of turboprops as turbojets/fans were faster, quieter and provided a more comfortable ride. Though the propulsive efficiency of turbojets/fans was lower than that of turboprops, low fuel prices and the relative discomfort of travelling at lower altitudes in turboprops made turbojets/fans more popular.

Following the energy crisis NASA funded six projects in the 1970s to improve fuel consumption on aircraft, of which one was on "advanced turboprops". Under this project, what came out was a "propfan" (today commonly known as an open-rotor), which is a small diameter, highly loaded propeller having swept blade tips with thin aerofoil sections. This concept was developed to deliver better fuel efficiency than contemporary turbofans. Propfans could reach higher speeds as they could spin fast enough and yet keep the speed of the blade tips below the transonic regimes, which could not be achieved in conventional propellers because of their larger diameters. Open rotors are now making a come-back, and the forecast is that the next generation of Airbus and Boeing single-aisle aircraft, due to enter service around 2019/2020, will fly with open rotor engines (Butterworth-Hayes 2010).

There is however renewed interest in turboprops because of climate change concerns, and unstable oil prices. There is also a pressing need to connect smaller towns and cities for sustained economic growth in India (Kota & Satish 2009) and many other developing economies, especially in Asia. Here turboprops have a natural advantage because of

their inherently higher fuel efficiency on short-haul routes. Boeing company's SUGAR (Subsonic Ultra Green Aircraft Research) entries in the NASA's ERA (Environmentally Responsible Aviation) project include a turboprop as one candidate (see figure 1.1).

Figure 1.1: The Boeing Volt design concept for the Subsonic Ultra Green Aircraft Research, or SUGAR, project (source: http://www.nasa.gov/)

An article from Aviation Week and Space Technology (Robert 2011) reports that the European Commission's newly declared "Flight path 2050" directive emphasises cleaner, quieter and more punctual flying. The target for cleaner flying is to cut down CO_2 and NO_x emissions by 75% and 90% respectively. Once again, turboprops may make a comeback because of their inherently higher fuel efficiency. Fuel consumption for turborprops is about 60% lower per passenger kilometre than that of jets (Pierre 2008) on route lengths of 500 km, meaning CO_2 emission is also lower by 60%.

Turboprops flying today have generally been designed with technologies that were available two to three decades ago. Therefore, by using modern technologies it should be possible to further improve the fuel efficiency. This idea is demonstrated in this thesis through one example in the field of aerodynamics. Turboprop wings have often been designed by treating propeller and the wing as two virtually independent units. We show that by including the propeller in the wing design process appreciable improvements in aerodynamic performance can be obtained. These can contribute to lower fuel consumption and hence lower emissions.

Mutual aerodynamic influence of propeller and wing has been a subject of study for a long time, starting from early 1900s (Prandtl 1921). Various methods and strategies have been adopted to study the problem of interaction. Among these the most notable efforts are due to Kroo (1986) and Veldhuis (2005), who have suggested the inclusion of propellers in the wing design process. By doing so, Kroo (1986) suggests, appreciable improvements in aerodynamic performance can be obtained. He also presents an optimization model to reduce the wing induced drag, and comments that certain changes in the propeller can also lead to better peformance. However, he does not present any specific proposals for new wings. Veldhuis (2005) proposes a different optimization model using which he

concludes that changing wing planform results in unrealistic optimized shapes. We find that the 'unrealistic' planforms obtained by Veldhuis are due to certain errors in problem formulation, handling certain integrals, and in the optimization strategy adopted.

In this thesis we present new, realistic wing shapes for turboprops in tractor configuration, designed by including propeller slipstream effects. The proposed wings have a better performance compared to the existing wings currently used in turborprops. First, we modify lifting-line theory to include propeller effects, and study the influence of the propeller slipstream on wing characteristics. We find that the slipstream can reduce the induced drag at a given lift (detailed explanations are given in subsequent chapters). The induced drag can be further reduced by shaping the wing planform, or incorporating a twist, or both. All this is demonstrated through the developement of an optimization program called PROWING, which is based on the extended lifting-line theory and the use of Bézier polynomials (Farin 2002) to represent the wing planform. PROWING optimizes the weights of the Bézier polynomials used to define the novel wing designs proposed here. The input to PROWING comprises certain overall geometric parameters of wing and propeller, wing aerofoil characteristics, and the velocity field in the slipstream downstream of the propeller. The required velocity field is computed using an Euler code (PROP-EULER) that mimics the effect of a rotating propeller. For this purpose a blade-element theory module for the propeller (Rajagopalan 1989; Lötstedt 1995) is used to provide source distributions of momentum and energy across an actuator disc that represents the propeller in PROP-EULER. A wide variety of optimal wing planform shapes can be generated using these programs, including one in which a modest change in planform in a wing of aspect ratio 12 showed an induced drag reduction of about 9.15%. This particular wing planform was analysed using the PROP-EULER code and the induced drag reduction predicted was about 7.9%, which is satisfactorily close to the results obtained using PROWING.

Therefore, we have a validated method by which wing planforms for turboprops in tractor configuration can be designed by exploiting the slipstream of the propeller, and so help obtain greater benefits in terms of drag and fuel consumption.

The thesis is organised as follows:

- Chapter 2: We review relevant earlier work. We briefly describe each work and highlight the differences between the current and earlier work.

- Chapter 3: The formulation of the optimization problem (PROWING) using extended lifting-line theory is presented. Modifications made to the classical lifting-line theory are also presented. Veldhuis's and Kroo's work is reviewed in detail and the source of the unrealistic chord distribution obtained by Veldhuis is identified.

- Chapter 4: The validation of PROWING described in chapter 3 is presented and optimal wing designs for various constraints and cost functions, using the optimization

formulation, are presented.

- Chapter 5: Optimal wing designs presented in chapter 4 are validated using high-fidelity CFD simulations. Results from Euler and RANS simulations on optimal and control wing designs are presented. For Euler simulations, an Euler code with propeller handling capability (PROP-EULER) was developed. The details and the code and its validation are presented first, and later the drag reductions obtained from it are presented. Results from RANS simulations are also presented.

- Chapter 6: Results from proof-of-concept wind tunnel tests for optimal wing design are presented in chapter 4. Consistency checks and analyis of the results are made. Some flow pictures/visualizations are also presented.

- Chapter 7: We summarize and conclude. Possible future work is discussed.

- Appendix A: A brief discussion on Bézier curves is presented.

Chapter 2
Review of Earlier Work

This thesis is about wing optimization for turboprops, more generally propeller-driven aircraft in tractor configuration. Earlier work relevant to that reported in this thesis is reviewed in this chapter.

Propeller-wing interaction was first studied by Prandtl (1921). Later researchers studied this problem with different objectives, like proposing a theoretical frame work for wing-propeller interaction, improving the theoretical framework for studying propeller flows, modeling of propellers as actuator disks, obtaining the slipstream through CFD, experimental investigations etc. More recent work relevant to the current study is then reviewed and presented here. None of them, except for Kroo (1986) and Veldhuis (2005), studied the problem of wing optimization of propeller-driven aircraft. Kroo (1986) follows a variational calculus approach for optimization but does not present any optimal wing designs for wing-propeller systems. Veldhuis (2005) follows a different approach (detailed review presented in chapter 3), and it is shown that because of certain errors in his work is led to a wrong conclusion.

Prandtl (1921)

Prandtl carried out wind tunnel experiments to investigate wing-propeller interference and commented that "*In judging the results, it is well to distinguish two kinds of influences, one due to variations in velocity, and the other due to variations in directions of the air current. The propeller is affected mainly by variations in the inflow velocity due to the wing. The wing is also subjected to slight changes in the direction of the air flow, which noticeably affect the drag*". He carried out experiments with propeller upstream as well as downstream of the wing.

Comments

For the tractor configuration, Prandtl observed a drag increase when the axis of the propeller is below the wing and a drag decrease if the axis lies above the wing. No physical explanation of the observations was offered. Furthermore, the issue of optimization of wing planform considering the effect of the propeller slipstream was not addressed.

Koning (1935)

In 1935, during the active life of the Guggenheim Fund for the Promotion of Aeronautics, a series of monographs were published on the general subject of Aerodynamic Theory, one of which was on propeller-wing aerodynamics (Koning 1935). Koning addressed the problem analytically by modifying the lifting-line theory to account for propeller effects. He used perturbation theory to arrive at a set of equations that represented the wing-propeller system. In this theory the ratio of the increment in the streamwise velocity in the slipstream to the free stream velocity was used as the small parameter. He did not consider the swirling motion in the slipstream while deriving the governing equations for the wing-propeller system.

Comments

- Swirling motion of the slipstream was not considered.
- Since the small parameter was defined as the ratio of increment in the streamwise velocity in the slipstream to the free stream velocity, the theory could only be applied to lightly loaded propellers.
- Optimization of wing planform considering the effect of propeller slipstream was not addressed.

Karman & Tsien (1945) and Fejer (1945)

Karman & Tsien (1945) commented that it is inappropriate to modify Prandtl's lifting-line theory for nonuniform flows, and developed a new theory starting from the inviscid momentum equations using the fundamental assumptions in Prandtl's lifting-line theory. Furthermore, they consider only a lightly loaded lifting-line. This method was subsequently used by Fejer (1945) for studying a flow where the free stream velocity U_∞ varied linearly in the spanwise direction.

Comments

- In the works of both Karman & Tsien (1945) and Fejer (1945), the slipstream rotation was ignored and the theory was limited to lightly loaded wings.
- If the aspect ratio is large and if the variation of velocities in the spanwise direction is small compared to the variation along the chord, the lifting-line theory, as modified to account for the nonuniformity, is a good approximation and lends itself as a tool to study the effects of propeller slipstream on the wing. This fact is demonstrated in chapters 5 and 6.

- Optimization of wing planform considering the effect of propeller slipstream was not addressed.

Rethorst (1958) and Jameson (1969)

Rethorst (1958) and Jameson (1969) comment that the use of lifting line theory is inappropriate for nonuniform flows. They treated the problem of a wing with several propellers by considering the wing immersed in a jet (no swirl), and used lifting surface theory for the analysis.

Comments

- Slipstream rotation was ignored.
- The authors' general conclusion that lifting line theory is inappropriate for nonuniform flows is not supported in this thesis when the aspect ratio is large and the variation of velocities in the spanwise direction is small compared to the variation along the chord. As demonstrated in chapters 5 and 6, lifting line theory appropriately modified to account for the nonuniformity is a good approximation, and lends itself as a tool to study the effects of the propeller slipstream on the wing.
- Optimization of wing planform considering the effect of propeller slipstream was not addressed.

Whitfield & Jameson (1983)

Whitfield & Jameson (1983) studied the problem of wing-propeller interaction in transonic flow. They used Euler equations with source terms for momentum and energy to simulate propeller slipstream. Viscous effects on the wing surface were computed by coupling 3D Euler equations with 2D compressible turbulent inverse-integral boundary layer equations. The source term for the thrust was imposed by specifying a jump in total pressure which was taken from experiment, and the force components in the plane perpendicular to the thrust were adjusted to obtain measured swirl velocities.

Comments

- A method of handling propellers was demonstrated
- Optimization of wing planform considering the effect of propeller slipstream was not addressed.

Kroo (1986)

Kroo (1986) modified the lifting line theory to account for the propeller, and addressed the problem of wing optimization in the presence of a propeller in tractor configuration. For obtaining the global minimum for the induced drag, he used variational calculus to derive closed form expressions for the Fourier coefficients that appear in the expansion of the spanwise circulation distribution.

Comments

- He does not present any optimal wing planform shapes.
- We find that, instead of finding load distributions that give global minimum induced drag, novel but realistic wing designs can be obtained not at the global optimum but at slightly sub-optimal levels. These wing designs cannot be obtained using Kroo's methodology.

Witkowski *et al.* (1989)

Witkowski *et al.* (1989) have studied aerodynamic interaction between propellers and wings. They carried out both experimental and computational investigations. For the computational study, they used the vortex lattice method. To account for viscosity in the computational study, viscous drag was added using empirical models. In both computational and experimental studies, they observed a reduction in induced drag in a wing-propeller system compared to the wing-alone system. However, they mention that the empirical methods used in total drag prediction in vortex lattice methods overpredict the drag reduction by 10-30%.

Comments

- Optimization of wing planform considering the effect of propeller slipstream was not addressed.

Rajagopalan (1989) and Lötstedt (1995)

Rajagopalan (1989)and Lötstedt (1995) followed an approach similar to that of Whitfield & Jameson (1983), but instead of using experimental data for the pressure jump and the swirl velocity, a combined momentum blade-element theory was used to compute the source distribution from the geometric characteristics of the propeller blades and the aerodynamic characteristics of the aerofoil sections of the blade.

Comments

- A method of incorporating the effect of propeller into a CFD algorithm based on blade aerofoil characteristics was demonstrated
- Optimization of wing planform considering the effect of the propeller slipstream was not addressed.

Conway (1995)

Conway (1995) modified the classical actuator disk theory to account for non-uniform radial loading which was not considered in the original theory developed by Rankine and Froude. Hough & Ordway (1965) gave an analytical solution for velocity fields induced by an actuator disk with unform radial loading. Conway derived analytical solutions for the entire flow field induced by a linearized actuator disk with arbitrary radial load distribution.

Comments

- Focus of the work was on constructing a rigorous theory to handle propellers by not making the assumption of Rankine and Froude regarding uniform load distribution. Also, Conway developed analytical solutions for the flow field induced by actuator disk.
- Design of wing planform considering the effect of propeller slipstream was not addressed.

Veldhuis & Heyma (1998), Veldhuis & Heyma (2000) and Veldhuis (2005)

Veldhuis & Heyma (1998), Veldhuis & Heyma (2000) and Veldhuis (2005) have addressed the problem of wing-propeller interference. They modified lifting-line theory to study the propeller slipstream effects on the wing. The influence of swirl was also considered. They carried out an optimization of wing twist to arrive at designs for lower total drag. They conclude that the optimal chord distribution obtained using their optimization process was unrealistic. Veldhuis (2005) found that the optimal chord distribution obtained by his method shoots upto about 6 times root chord. We shall show in chapter 3 the reasons for the unrealistic chord distributions obtained by this method.

Comments

- Veldhuis & Heyma (1998), Veldhuis & Heyma (2000) and Veldhuis (2005) have reported that the optimal chord distribution is unrealistic. Therefore their optimization process does not consider chord as a design variable.
- We shall analyse in chapter 3 the reasons for his unrealistic conclusions.

Roosenboom *et al.* (2010)

Roosenboom *et al.* (2010) solved the unsteady RANS equation in the whole domain, an approach which is closer to reality but computationally expensive. They also carried out wind tunnel experiments and the velocities in the slipstream were measured and compared with CFD.

Comments

- Focus of the work was on validation and verification of CFD solutions.
- Design of wing planform considering the effect of propeller slipstream was not addressed.

Summary

To summarize, many workers in the past have looked at wing-propeller interaction. Only Kroo (1986) and Veldhuis (2005) have looked at optimization of wing shape for tractor-propeller configurations. Kroo (1986) derives analytical expressions for globally optimal load distributions but does not present any specific optimal wing shapes. Veldhuis (2005) generates optimal wing designs by giving twist distributions and dismisses the chord distribution as an option after obtaining unrealistic results. From the earlier work reviewed in this chapter, the more significant contributions are listed in Table 2.1 for quick reference. The table indicates in brief what the authors did and what is reported in this thesis. Here we extend the lifting-line theory to account for propeller effects and, most importantly, the extended theory is coupled to an optimizer, using which we can generate novel realistic wing designs of lower drag, with both chord and twist distributions.

	Koning (1934)	Kroo (1986)	Lötstedt (1995)	Veldhuis (2005)	Current work	Current work
Equation	lifting-line	lifting-line	Euler	lifting-line	lifting-line	Euler
Assumption	Small perturbations	-	Blade element theory + momentum, energy sources at disk	-	-	Blade element theory + Estimated sources at actuator disk
Optimization	-	Fourier coefficients of circulation for global minimum induced drag	-	Fourier coefficients of globally optimal circulation (different from Kroo's expression)	Planform optimization using Bëzier polynomials	-
Planform result	-	-	-	Unrealistically long chords in slipstream	Novel planforms proposed	Proposed novel planforms validated

Table 2.1: Tabular representation of relevant earlier work for quick reference

Chapter 3
Formulation of the Optimization Problem

We consider in this chapter the methods by which aircraft powered by propellers or other rotors can exploit the propeller slipstream for designing more aerodynamically efficient wings. To make use of the propeller slipstream in the wing design process, we begin with a simple theory for propeller-wing interaction, and formulate an appropriate optimization problem and implement it. For this purpose a model based on lifting-line theory that represents a wing-propeller system is developed. For this model, the time averaged axial and circumferential velocities induced by the propeller along the lifting line that represents the wing are considered. The part of the wing that is immersed in the propeller slipstream experiences an increase in the axial velocity and an up-wash and downwash field (which together we shall call 'propwash') due to the rotation of the propeller. Lifting-line theory is modified to account for the change in axial velocity and the propwash field. This model forms an important element in the optimization process. In this chapter the details of the aerodynamic model and the formulation of the optimization problem are described in detail. Furthermore the works of Kroo (1986) and Veldhuis (2005), reviewed briefly in chapter 2, are also discussed in detail.

3.1 Problem Formulation

The present modelling of a wing-propeller system using lifting-line theory is similar to what was followed by Kroo (1986). Figure 3.1 shows a schematic of a wing in a tractor-propeller configuration. The wing has a semispan s and chord distribution $c(y)$ where y is the spanwise coordinate. Within the propeller slipstream there is an increase in the axial velocity $V(y)$ and an additional downwash $w_p(y)$ (which may be positive or negative) over and above the downwash $w_w(y)$ due to the trailing vortices of the wing. The effect of wing on propeller is ignored.

Figures 3.2 and 3.3 show the time averaged variation of axial velocity and downwash in the propeller slipstream computed numerically using the PROP-EULER code (to be described in chapter 5). The propeller is assumed to be located at $x/D = 1.0$ (x measured from the wing leading edge) where D denotes the diameter of the propeller. The coordinate y runs along the span of the wing across the diameter of the slipstream. In order to

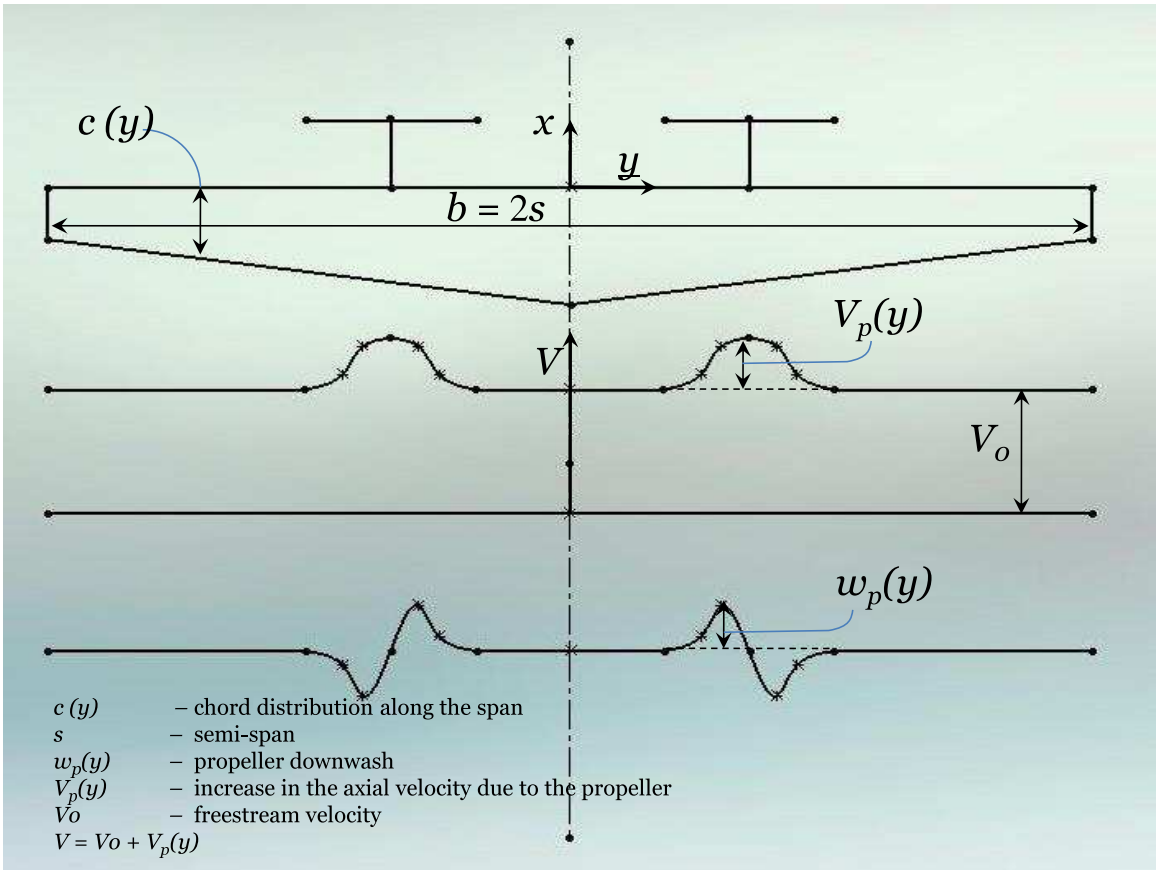

Figure 3.1: Schematic representation of a wing in tractor-propeller configuration

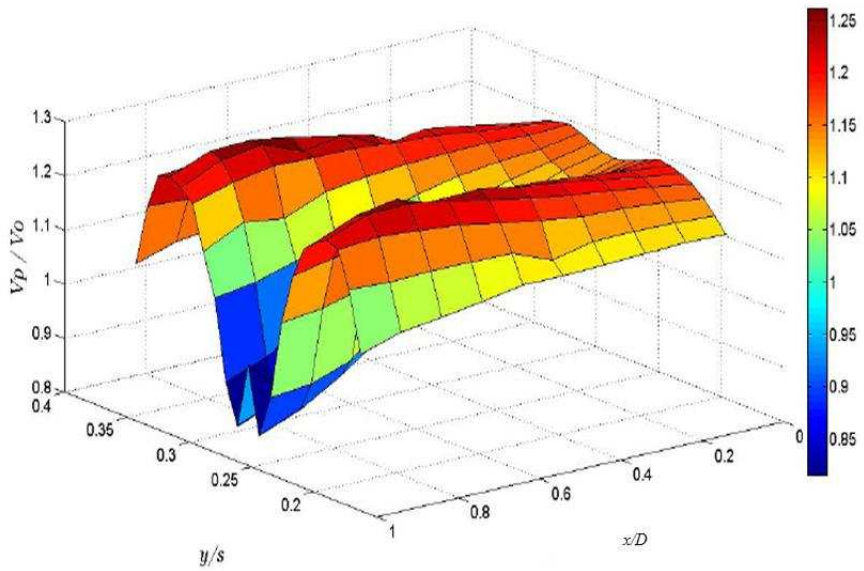

Figure 3.2: plot of time averaged axial velocity in the propeller slipstream

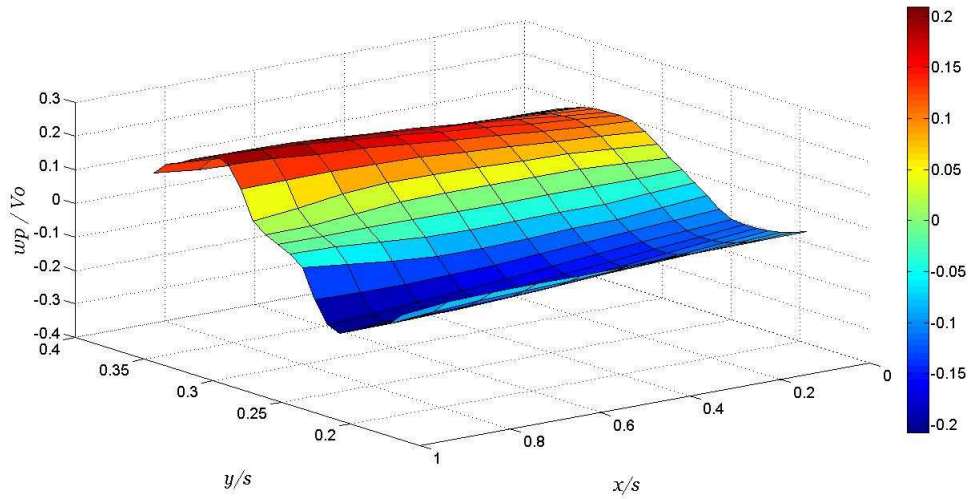

Figure 3.3: plot of time averaged downwash field in the propeller slipstream

account for the propeller slipstream effects, an extended lifting line theory is developed. The mathematical formulation of the theory is as follows:

Given: $V(y) \equiv V_0 + V_p(y)$ and $w_p(y)$, where $V_p(y)$ and $w_p(y)$ are the time-averaged axial velocity and downwash respectively due to the propeller and V_0 is the free stream velocity. It is assumed here, for simplicity, that the propeller slipstream is in the direction of the free stream at infinity. This assumption should be reasonable at cruising flight. However, inclined slipstreams can be accounted for. The total downwash $w(y)$ is the sum of the downwash due to the wing and the propeller. If Γ is the circulation at y' then the total downwash is given by

$$w(y) = w_w(y) + w_p(y) \tag{3.1}$$

$$= \frac{1}{4\pi} \int_{-s}^{+s} \frac{1}{y - y'} \frac{d\Gamma}{dy'} \, dy' + w_p(y) \tag{3.2}$$

The first term on the right hand side of eq. 3.2 is obtained using the Biot-Savart relation as used in classical lifting line theory for calculating the induced velocity due to all the trailing vortices of the wing at any spanwise location. For detailed derivation, see chapter 10 in Glauert (1926). The effective angle of attack α_e (see fig. 3.4 for graphical representation) that the aerofoil section at y sees is then given by

$$\alpha_e = \alpha - \frac{w_w(y) + w_p(y)}{V(y)} \tag{3.3}$$

where $\alpha(y) = \alpha_g - \alpha_t(y)$, α_g is the geometric angle of attack and $\alpha_t(y)$ is the twist along the span;α_e is considered positive in the counter clockwise direction measured from the chord line.

The lift L and induced drag D_i are given respectively by

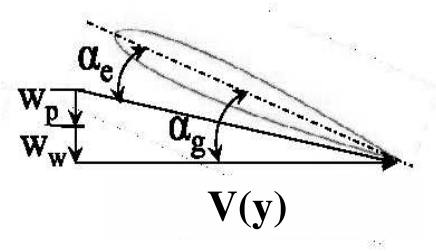

Figure 3.4: Definition of effective angle of attack including the propeller swirl

$$L = \rho \int_{-s}^{+s} V(y)\Gamma(y)\,\mathrm{d}y \tag{3.4}$$

$$D_i = \rho \int_{-s}^{+s} w(y)\Gamma(y)\,\mathrm{d}y \tag{3.5}$$

The profile drag D_p for the wing is obtained by integrating the local profile drag,

$$D_p = \rho \int_{-s}^{+s} 0.5\,V(y)^2 c_d(y) c(y)\,\mathrm{d}y \tag{3.6}$$

For a specific chosen aerofoil c_d for a given c_l is read from the drag polar, obtained either from wind tunnel tests or CFD simulations. The total drag D is then obtained by summing induced and profile drag ($D = D_i + D_p$).

Transforming the coordinate system from y to θ by putting

$$y = -s\cos\theta \tag{3.7}$$

and expanding Γ in a Fourier series with A_k as the Fourier coefficients, we write

$$\Gamma = 4sV_0 \sum_{k=1}^{\infty} A_k \sin k\theta \tag{3.8}$$

Using eq. 3.8, eq. 3.2 gets transformed to

$$w(y) = V_0 \frac{\sum_{k=1}^{\infty} k A_k \sin k\theta}{\sin\theta} + w_p(y) \tag{3.9}$$

The sectional load l is given by

$$l = \rho\, V\, \Gamma = \frac{1}{2}\rho\, V^2\, c\, c_l \tag{3.10}$$

where c is the chord at any location y along the span and c_l is the lift coefficient of the aerofoil section at the same location,

$$c_l = a_0\,(\alpha - \frac{w_w(y) + w_p(y)}{V(y)}) \tag{3.11}$$

where a_0 is the lift-curve slope of the aerofoil section and α is measured with respect to the zero-lift angle of the aerofoil section.

Using equations 3.8 - 3.11 we obtain the fundamental equation to determine the Fourier coefficients as

$$(\sum_{k=1}^{\infty} A_k \sin k\theta)(k\mu + \sin\theta) = \mu\frac{V(\theta)}{V_0}(\alpha - \frac{w_p(\theta)}{V(\theta)})\,\sin\theta \tag{3.12}$$

where $\mu = a_0 c/8s$.

Using eq. 3.8 eq. 3.4 will transform into

$$L = 4\rho V_0 s^2 \int_0^{\pi} V(\theta)\sin\theta \sum_{k=1}^{\infty} \sin k\theta\,\mathrm{d}\theta \tag{3.13}$$

Using eqs. 3.8 and 3.9 eq. 3.5 will transform into

$$D_i = 2\pi s^2 \rho V_0^2 \sum_{k=1}^{\infty} k A_k^2 + B_k \tag{3.14a}$$

where

$$B_k = \frac{2}{\pi}\int_0^{\pi} \frac{w_p(y)}{V_0}\sin k\theta \sin\theta\,\mathrm{d}\theta \tag{3.14b}$$

3.2 Method of Solution

The extended lifting-line equation (eq. 3.12) is solved to determine the Fourier coefficients using the least squares technique. Let n_c and n_f ($< n_c$) be the number of collocation points along the span and number of Fourier coefficients respectively (number of points and modes are chosen after performing a convergence study which is described in chapter 4), then the least squares formulation of eq. 3.12 will be as follows:

Defining LL using 3.12 as

$$\mathrm{LL}(\theta_i, A_1, A_2, ..., A_{n_f}) = (\sum_{k=1}^{\infty} A_k \sin k\theta_i)(k\mu + \sin\theta_i) - \mu\frac{V(\theta_i)}{V_0}\sin\theta_i(\alpha - \frac{w_p(\theta_i)}{V(\theta_i)}) \tag{3.15}$$

where $i = 1...n_c$, the least squares formulation is obtained by equating to zero the partial derivatives of LL with respect to the Fourier coefficients $A_1...A_n$.

$$\frac{\partial}{\partial A_j}\sum_{i=1}^{n_c} \mathrm{LL}(\theta_i, A_1, A_2, ..., A_{nf}) = 0\,; j = 1...n_f \tag{3.16}$$

Validation and results from the code using this method are presented in chapter 4.

3.3 Optimization

Since the main goal here is to optimize wing planforms for lower total/parasite/induced drag, an optimization problem is formulated.

The drag (induced (D_i), profile (D_p), or total ($D_i + D_p$)) that needs to be minimised is chosen as the cost function. The optimization process is carried out under any prescribed aerodynamic, geometric and structural constraints. Aerodynamic constraints include the wing lift coefficient, pitching moment and the extended lifting-line equation (eq. 3.12). The geometric constraints considered here include tip chord, root chord, wing area, bounds on chord and twist etc., and the structural constraints include root bending moment etc. The constraints are not restricted to the ones mentioned above. The chord and twist are taken as the variables in the present study.

When it is required to have a smooth wing trailing edge, the chord and twist are parameterized using Bézier curves (Farin 2002) as shown in eqs. 3.17a and 3.17b; see appendix A for a brief discussion of Bézier curves),

$$c(y) = \sum_{i=0}^{n_{dc}} B_i^n(y)\, w_{c_i} \tag{3.17a}$$

$$\alpha_t(y) = \sum_{i=0}^{n_{dt}} B_i^n(y)\, w_{t_i} \tag{3.17b}$$

where n_{dc} and n_{dt} are the degrees of the Bézier curve used for chord and twist parameterization respectively, w_c and w_t are the Bézier modes associated with chord and twist respectively and B_i^n is the i^{th} Bernstein polynomial of degree n defined as

$$B_i^n = \binom{n}{i}(1-y)^{n-i}y^i,\ y \in [0\ 1] \tag{3.18}$$

Mathematically the problem can be stated as follows:

$$\begin{aligned} \text{minimize} \quad & D_i(c, \alpha_t) + D_p(c, \alpha_t) \\ \text{subject to} \quad & \text{LL} = 0 \\ & S_{opt} = S_{ref} \\ & L_{\text{opt}} = L_{\text{des}} \\ & c_{\text{opt}} > 0 \end{aligned} \tag{3.19}$$

where LL is the lifting line equation (eq. 3.15), D_i and D_p are induced and profile drag forces respectively, c, α_t are chord and twist respectively which are the design variables, S_{opt} and S_{ref} are the optimal and reference planform areas respectively, L_{opt} and L_{des} are

the optimal and design wing lift forces.

A software called PROWING was written in MATLAB (2007), to perform constrained optimization using an inbuilt function of MATLAB called fmincon (detailed documentation of fmincon can be obtained in http://www.mathworks.co.uk/help/optim/ug/fmincon.html (.)) which solves the Karush-Kuhn-Tucker (KKT) equations which are the necessary conditions for optimality for a constrained optimization problem. The operation of PROWING is described in the flow chart shown in figure 3.5.

The input to PROWING comprises

- geometric details of wing: wing area, root chord, tip chord, washout etc.,
- aerodynamic parameters: e.g. design lift coefficient (C_L),
- aerofoil data: $c_l(\alpha)$, $c_d(\alpha)$,
- numerics: number of collocation points n_c, number of Fourier modes n_f, number of modes to be used in Bézier parameterization,
- propeller details: diameter, location of propeller along the span, time-averaged slipstream velocities obtained either through wind tunnel tests or CFD simulations;
- cost function: C_{Di}, C_{Dp}, C_D ...
- constraints: bounds on twist and chord, tip chord and root chord, wing area etc.

Once the input is specified, the software then parameterizes the chord and twist distibution using the 'shape parameterization' module, and starts iterating to approach the optimal by minimizing the cost function computed using the module 'FUN', by making sure that the constraints are obeyed using the module 'NONLCON'. Optimal wing shapes are generated once the optimum is reached.

3.4 Comparison with other works in the literature

As mentioned in the chapter 2, Kroo (1986) and Veldhuis (2005) have addressed the problem of wing optimization of turboprop aircraft and these are the two earlier works that are very close to the subject of this thesis. Kroo's work is presented first and a critical review of Veldhuis's work is made later in this section.

3.4.1 Kroo (1986)

Kroo analysed the problem of wing-propeller interaction by modifying the lifting-line theory to account for propeller effects. Kroo's expressions for the lift and drag with propeller effects included are the same when compared to what we have obtained above.

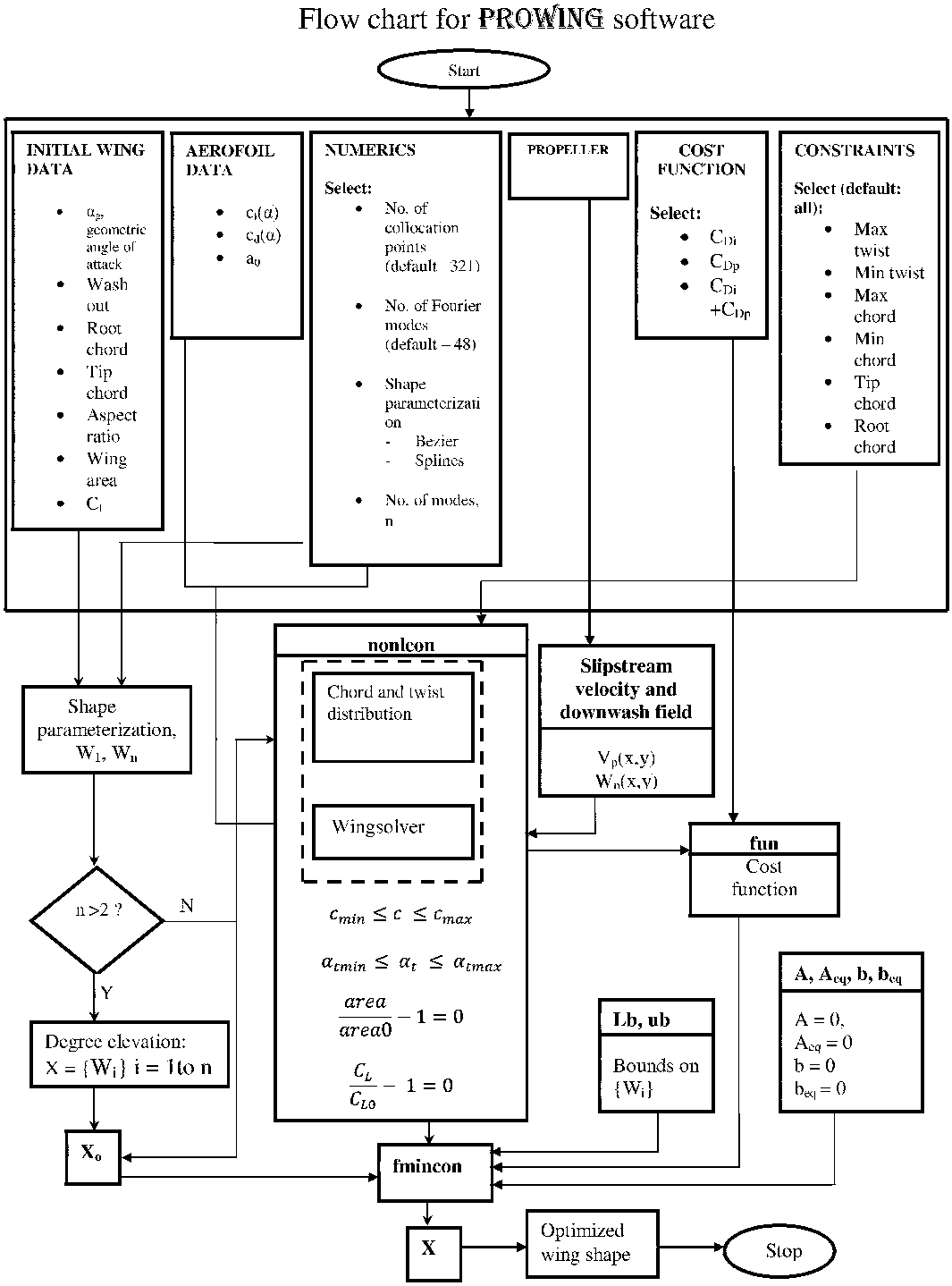

Figure 3.5: Flowchart describing the operation of PROWING

However, the optimization strategy adopted by Kroo was different. He made use of the classical variational calculus approach to carry out the optimization. He derived a closed form expression for the optimal Fourier coefficients. Using Kroo's method for optimization, only those designs that are globally optimal can be obtained. On the other hand the optimization strategy (described in section 3.3) formulated here shows how locally optimal designs can be obtained. This is the key difference between Kroo's work and the present approach. Highlights of his work are presented in this section.

Modified equations for the lift L^* and drag D forces are given by

$$L = \frac{4}{\pi b} \sum_n A_n I_{un} \tag{3.20}$$

[Kroo (1986):562(10)]† where

$$I_{un} = \int_{-b/2}^{b/2} U(y) \sin n\theta dy, \tag{3.21}$$

and

$$D = \frac{1}{q\pi b^2} \sum_n A_n^2 + \frac{4}{\pi b} \sum_n A_n I_{wn} \tag{3.22}$$

[Kroo (1986):562(11)], where

$$I_{wn} = \int_{-b/2}^{b/2} w_p(y) \sin n\theta dy. \tag{3.23}$$

Kroo makes use of the classical variational calculus approach to carry out the optimization, i.e. putting

$$\frac{\partial \text{Obj}}{\partial A_n} = 0 \quad n = 1, 2, 3, ..., \infty, \tag{3.24}$$

where

$$\text{Obj} = D + \lambda(L - \frac{4}{\pi b} \sum_n A_n I_{Un}) \tag{3.25}$$

[Kroo (1986):563(12)], where λ is the Lagrange multiplier, the lift force (L) is a constraint and the contributions of all Fourier coefficients A_n are taken into account.

Kroo's expression for optimal Fourier coefficients [Kroo (1986):563(13)] is

$$A_n = \frac{\rho U_\infty b}{n} [(\frac{\pi L}{4\rho U_\infty^2} + \sum_j \frac{I_{Uj} I_{wj}}{j})(I_{Un} / \sum_j \frac{I_{Uj}^2}{j}) - I_{wn}]. \tag{3.26}$$

Kroo however does not present any result showing optimal planforms using the method-

*All symbols in section 3.4.1 are the same as the ones used by Kroo. Table 3.1 shows the relation between symbols used by Kroo and the corresponding symbols used in this thesis.

†This notation refers to equation 10 appearing in p.562 of Kroo (1986)

Kroo (1986)	PROWING
$A_n/2\pi s^2\rho V_0^2$	A_k
L	L
D	D_i
$b/2$	s
u	V_p
U_∞	V_0

Table 3.1: Comparison of symbols used in Kroo (1986) and PROWING

ology described by him, although he mentions that changes in chord, twist, camber and thickness distributions can have significant benefits on wing performance. He also mentions that the wing could be designed for recovering the loss associated with slipstream swirl.

3.4.2 Veldhuis (2005)

Veldhuis has considered optimal designs for wings of aircraft driven by wing-mounted tractor propellers. The optimization is carried out on twist, camber and chord distributions along the wing span. We focus on chord distributions, for which Veldhuis's solution yields a very long chord in the portion of the wing behind downward-moving propeller blades and a short chord on the other side of the slipstream. This is correctly characterized as 'unrealistic' by the author himself. This 'unrealistic' chord distribution obtained by Veldhuis may be traced to three factors: (i) error in basic formulation, (ii) error in evaluation of certain integrals and (iii) inappropriate search space used in the optimization process. Each of these is described in subsequent sections.

3.4.2.1 Error in basic formulation

To explain the error in the basic formulation, highlights of a (presumed) derivation of the equation for induced drag coefficient 3.27 are presented here since the detailed derivation is not given either in Veldhuis's publications (Veldhuis & Heyma 1998, 2000) or in the thesis (Veldhuis 2005).

The expression used by Veldhuis for the induced drag coefficient, C_{Di} [‡] (Veldhuis (2005):266(7.12)) is

$$\begin{aligned} C_{Di} = 2AR\sum_{n}^{\infty}\sum_{k}^{\infty} nA_nA_k \int_0^\pi \sin(n\theta)\sin(k\theta)(1+a(\theta))d\theta \\ +2AR\sum_{n}^{\infty} A_n \int_0^\pi \alpha_{ip}(\theta)\sin(n\theta)\sin(\theta)(1+a(\theta))d\theta, \end{aligned} \tag{3.27}$$

[‡]All symbols in section 3.4.2 are the same as the ones used by Veldhuis and are listed in figures 3.13, 3.14. Table 3.2 shows the relation between symbols used by Veldhuis and the corresponding symbols used in this thesis

Veldhuis (2005)	PROWING
$A_n/$	A_k
L	L
D_i	D_i
$b/2$	s
V_{ax}	V_p
U_∞	V_0
Γ	Γ
ρ	ρ
θ	θ
AR	$\mathcal{AR}$

Table 3.2: Comparison of symbols used in Veldhuis (2005) and PROWING

where AR is the aspect ratio, θ is the angular variable obtained by transforming the physical coordinate y using $\theta = \cos^{-1}(-2y/b)$ (same as eq. 3.7), $a(\theta)$ is the increment in the streamwise velocity behind the propellers normalised with by freestream velocity U_∞, A_k are the Fourier coefficients in the expansion of Γ (see eq. 3.33, same as eq. 3.8) and $\alpha_{ip}(\theta)$ is the downwash angle due to the propeller.

Veldhuis defines the integral [Veldhuis (2005):267(7.15)]

$$I_{nk} = \int_0^\pi \sin(n\theta)\sin(k\theta)(1 + a(\theta))d\theta \tag{3.28}$$

and in the first line on p.268 in Veldhuis (2005), it is mentioned that $I_{nk} = 0$ when $n \neq k$.

Using eq. 3.28 and the above assumption made for I_{nk} by Veldhuis, eq. 3.27 can be written as

$$\begin{aligned} C_{Di} = AR\sum_n^\infty\sum_k^\infty nA_n^2\int_0^\pi \sin^2(n\theta)(1+a(\theta))d\theta \\ +2AR\sum_n^\infty A_n\int_0^\pi \alpha_{ip}(\theta)\sin(n\theta)\sin(\theta)(1+a(\theta))d\theta, \end{aligned} \tag{3.29}$$

The derivation of eq. 3.29 (simplified version of eq. 3.27) is now presented.

The induced drag force D_i [Veldhuis (2005):265(7.5)] is taken as

$$D_i = \rho U_\infty \int_{-\frac{b}{2}}^{\frac{b}{2}} \alpha_i(y)\Gamma(y)dy \tag{3.30}$$

In the last line on p.265 Veldhuis mentions that the expression for induced drag with the propeller slipstream effects included could be obtained by following the procedure in deriving an expression for lift with propeller slipstream effects included. For the lift expression, Veldhuis multiplies the propeller induced axial velocity factor $a(\theta) = V_{ax}(\theta)/U_\infty$

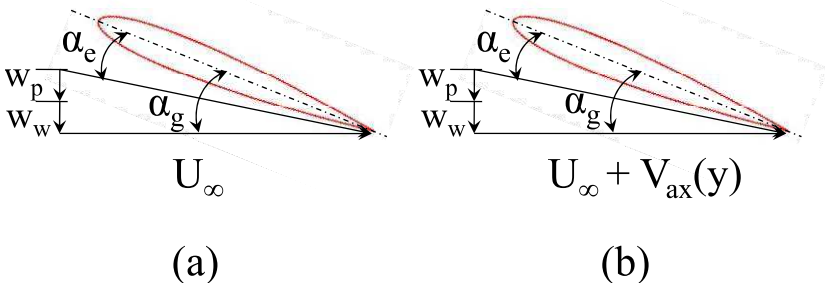

Figure 3.6: Reference velocity used to obtain local angle of attack: (a) Veldhuis - increment in axial velocity is neglected. (b) Present work and Kroo - increment in axial velocity because of propeller as a function of span is considered.

to the lift expression for the wing alone case [Veldhuis (2005):265(7.9)],

$$L = \rho U_\infty^2 b \sum A_n \frac{b}{2} \int_0^\pi \sin n\theta (1 + a(\theta)) \sin\theta \mathrm{d}\theta. \tag{3.31}$$

Therefore, on multiplying eq. 3.30 by the propeller induced axial velocity factor $a(y) = V_{ax}(y)/U_\infty$ to incorporate the effects of propeller slipstream we get

$$D_i = \rho U_\infty \int_{-\frac{b}{2}}^{\frac{b}{2}} \alpha_i(y)\Gamma(y)(1 + a(y))dy \tag{3.32}$$

Using the expression for Γ [Veldhuis (2005):265(7.6)]

$$\Gamma = 2U_\infty b \sum_{n=1}^{N} A_n \sin(n\theta). \tag{3.33}$$

and replacing the physical coordinate y by the angular variable eq. 3.32 becomes

$$D_i = \rho U_\infty^2 b^2 \int_0^\pi \alpha_i(\theta)(1 + a(\theta)) \sum_{n}^{\infty} A_n \sin(n\theta) \sin(\theta) \mathrm{d}\theta \tag{3.34}$$

where

$$\alpha_i = \alpha_{iw} + \alpha_{ip} \tag{3.35}$$

[Veldhuis (2005):264(7.2)], α_i being the total induced angle of attack, α_{iw} the induced angle of attack due to the wing and α_{ip} that due to the propeller.

The angle α_{i_w} is defined by Veldhuis as [Veldhuis (2005):264(7.3)]

$$\alpha_{iw}(y_0) = \frac{-1}{4\pi U_\infty} \int_{-b/2}^{b/2} \frac{\mathrm{d}\Gamma(y)/\mathrm{d}y}{y_0 - y} \mathrm{d}y \tag{3.36}$$

In this definition the free stream velocity U_∞ is erroneously used by Veldhuis to estimate the induced angle of attack due to wing. This is shown pictorially in fig. 3.6.

Using eq. 3.33 , substituting eqs. 3.35 and 3.36 in eq. 3.34, using the assumption made

for I_{nk} and nondimensionalising using U_∞, freestream density(ρ_∞), and wing planform area(S), eq. 3.34 becomes

$$\begin{aligned} C_{Di} &= AR \sum_{n}^{\infty} \sum_{k}^{\infty} n A_n^2 \int_0^\pi \sin^2(n\theta)(1 + a(\theta))d\theta \\ &+2AR \sum_{n}^{\infty} A_n \int_0^\pi \alpha_{ip}(\theta) \sin(n\theta) \sin(\theta)(1 + a(\theta))d\theta, \end{aligned} \tag{3.37}$$

which is the same as eq. 3.29. We have shown above that eq. 3.29 is obtained by Veldhuis assuming that the free stream velocity U_∞ is to be used to calculate the local angles of attack at any section y along the span (see fig. 3.6a). But it is physically incorrect to measure the local angle of attack with respect to the freestream velocity U_∞ in the slipstream of a propeller. The reason is that the wing sections behind the propeller experience an angle of attack determined by the velocity $U(y)$ at the station y within the propeller slipstream, which is not taken into consideration by Veldhuis (fig. 3.6a).

We now show how the expression for C_{Di} changes when the error is corrected by the use of the local approach velocity, $U(y)$. The local angle of attack (see fig. 3.6 (b)) should be estimated with respect to the 'local' free stream velocity seen by the wing, namely $U_\infty + V_{ax}(y)$ as indicated earlier by Kroo (1986) and adopted here, then eq. 3.36 would be replaced by

$$\alpha_{iw}(y_0) = \frac{-1}{4\pi(U_\infty + V_{ax}(y_0))} \int_{-b/2}^{b/2} \frac{d\Gamma(y)/dy}{y_0 - y} dy \tag{3.38}$$

Again using eq. 3.33, transforming the physical coordinate y to angular coordinate θ , substituting eqs. 3.35 and 3.38 in eq. 3.34 and nondimensionalising it, we get the correct expression for C_{Di} (same as our eq. 3.14a written in Veldhuis's notation) as

$$\begin{aligned} C_{Di} &= AR \sum_{n}^{\infty} \sum_{k}^{\infty} n A_n^2 \int_0^\pi \sin^2(n\theta) \mathrm{d}\theta \\ &+2AR \sum_{n}^{\infty} A_n \int_0^\pi \alpha_{ip}(\theta) \sin(n\theta) \sin(\theta)(1 + a(\theta)) \mathrm{d}\theta, \end{aligned} \tag{3.39}$$

It can be seen that the first term on the right hand side of eq. 3.39 does not contain the $1+a(\theta)$ term when compared to the corresponding term in eq. 3.37, the result derived by Veldhuis.

Therefore, we infer that Veldhuis has incorrectly neglected the influence of the increase in axial velocity because of the propeller.

n	k	I_{nk}
1	1	1.6091
1	3	-0.0253
1	5	0.0045
1	7	0.016
1	9	-0.0285
1	11	-0.0297

Table 3.3: Cases chosen for evaluation of I_{nk}

3.4.2.2 Error in evaluation of certain integrals

In the process of evaluating eq. 3.27 Veldhuis defines the integral [Veldhuis (2005):267(7.15)]

$$I_{nk} = \int_0^{\pi} \sin n\theta \sin k\theta (1 + a(\theta)) d\theta \tag{3.40}$$

As we have already mentioned, Veldhuis (2005) (first line on p.268) takes $I_{nk} = 0$ when $n \neq k$. However the above integral, when $n \neq k$, is not zero. To illustrate this, we analyse the six listed cases table 3.3.

To evaluate the integrals slipstream data is needed. Since the data used by Veldhuis is not available in the public domain, typical values for $a(\theta)$ were taken from the CFD simulation carried out for this thesis (details of CFD simulations are described in chapter 5) for the propeller tested by Hartman & Biermann (1938). This particular propeller was chosen because the entire information needed to carry out the numerical simulation is available in the public domain, and this propeller is typical of the kind used in turboprops. The spanwise variation of a so obtained is shown in fig. 3.7. For each case the corresponding value of the integral I_{nk} is shown in table 3.3. The integrals were computed using 320 points along the θ axis.To ensure that the step size used for integration is sufficiently small, integration with 640 points was performed, and the value of the integral changed only by 0.12%. It can be seen that all the I_{nk} except I_{11} is either two or three orders of magnitude smaller compared to I_{11}. However they are not zeroes. Though the values of the I_{nk} except I_{11} are small (compared to I_{11}), the assumption that $I_{nk} = 0$ when $n \neq k$ is incorrect.

Veldhuis further defines the integral [Veldhuis (2005):267(7.16)]

$$J_n = \int_0^{\pi} \alpha_{ip}(\theta) \sin(n\theta) \sin(\theta)(1 + a(\theta)) d\theta \tag{3.41}$$

If we assume $J_n = 0$ when $n = 2, 3, 4...$ (following Veldhuis's assumption on I_{nk}) we reproduce the optimal wing chord distribution of the kind that Veldhuis arrived at (see fig. 3.8a). Since the propeller slipstream velocities used by Veldhuis are not known, only a qualitative comparison between the results obtained by us and Veldhuis is possible. The

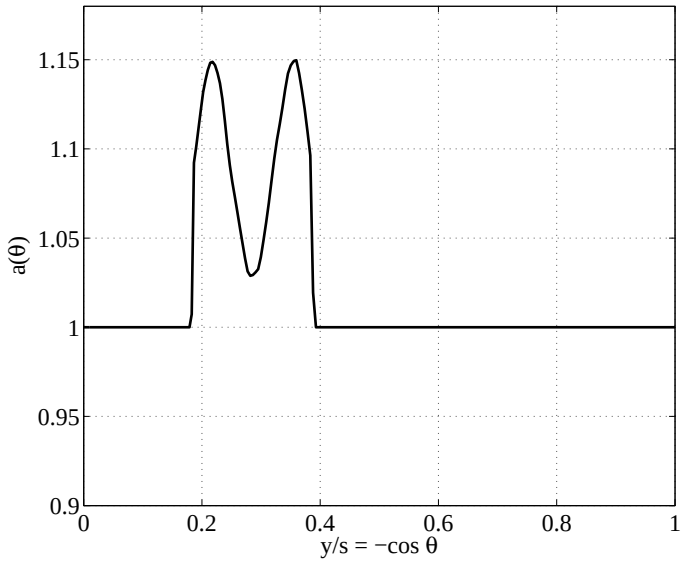

Figure 3.7: Typical variation of propeller induced axial velocity increase factor a along the semispan

integral J_n for $n = 2, ..., \infty$ is in fact not zero; for certain values of n the value of J_n is orders of magnitude larger than J_1 (see fig. 3.9). (The values of α_{ip} used to compute J_n are taken from the numerical simulation carried out here for the reason mentioned in section 3.4.2.2; for the present variation of $\alpha_{ip}(y)$ with y see fig. 3.10). On rectifying the error in the evaluation of the integral J_n, one obtains a chord distribution (shown in fig. 3.11) that is drastically different when compared to the one obtained here using Veldhuis's methodology (shown in fig. 3.8a).

Though the integral $I_{nk} \neq 0$ for $n \neq k$, its value is about two orders of magnitude smaller compared to the value of I_{nk} when $n = k$ (for numerical values of I_{nk} refer to previous section). On rectifying the errors described in section 1, in evaluating I_{nk} but not in evaluating J_n, the chord distribution would still look the same as shown in fig. 3.8a. But on rectifying the assumption made for J_n we would get a get a chord distribution as shown in fig. 3.11. This shows that J_n has the bigger influence on the chord distribution. However, even in the chord distribution shown in fig.3.11, longer chords (though not spiked) can still be seen in the region of propeller slipstream. This particular characteristic of chord distribution is explained in section 3.4.2.3.

We therefore conclude that it is not justifiable to assume the integral $J_n = 0$ when $n = 2, ..., \infty$.

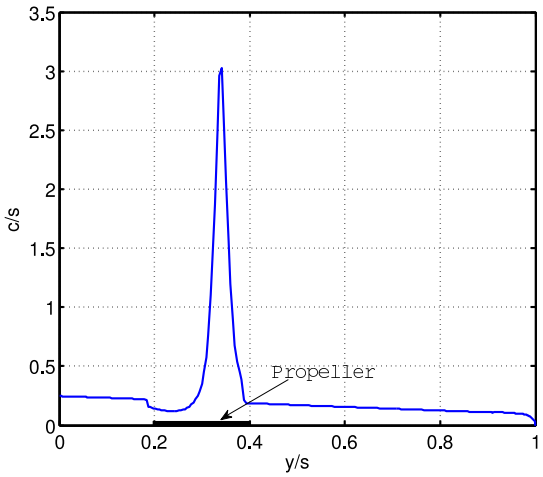

(a) Chord distribution obtained using a code written by the authors by Veldhuis's methodology. This was obtained by considering J_1 only

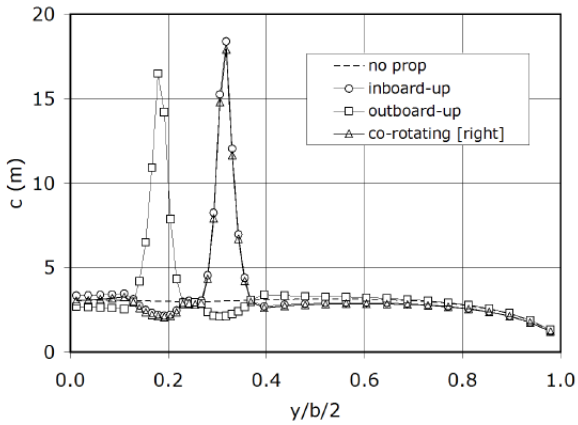

(b) Chord distribution for optimum loading obtained by Veldhuis (figure taken from Veldhuis & Heyma (1998) p.10)

Figure 3.8

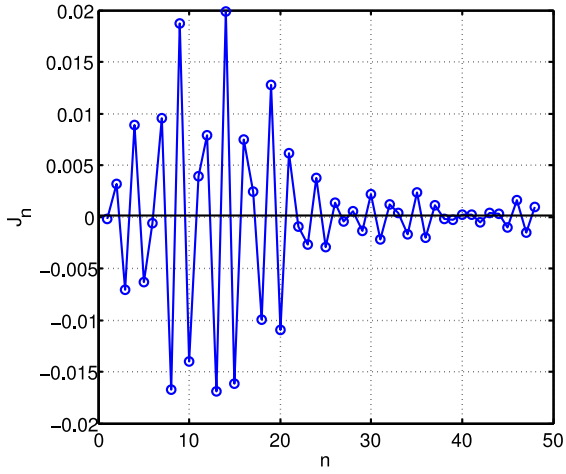

Figure 3.9: Integral J_n computed for $n = 1, ..., 48$

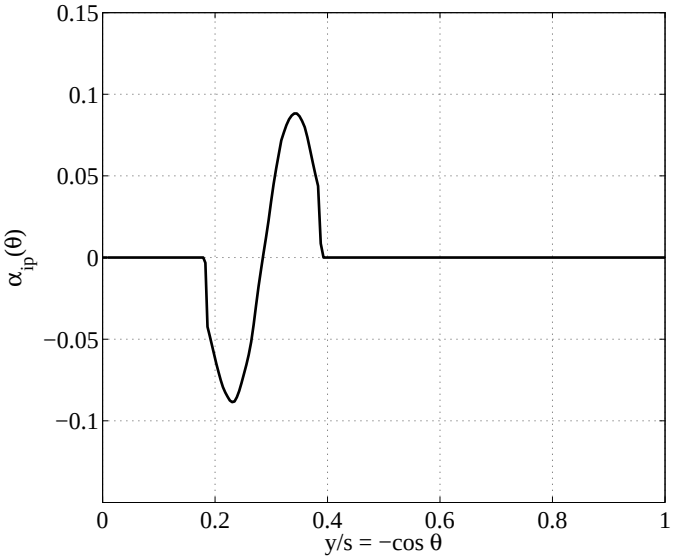

Figure 3.10: Typical variation of α_{ip} along the semispan

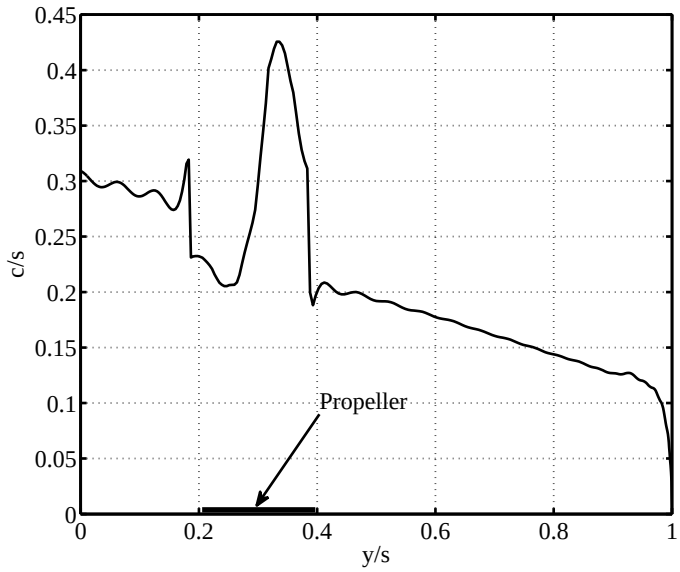

Figure 3.11: Chord distribution obtained using Veldhuis's methodology after including J_n; $n = 2...\infty$

3.4.2.3 Search space used in optimization

In this section the occurrence of longer chords in Veldhuis's solution in the region of the propeller slipstream is explained.

In order to find the optimal load distribution for a given lift coefficient (C_L), Veldhuis first differentiates eq. 3.37 partially with respect to the Fourier coefficients (A_n) as given by Veldhuis (2005) (p.267(7.14), i.e. he puts

$$\frac{\partial C_{Di}}{\partial A_n} = 0 \qquad n = 2, 3, ..., \infty \tag{3.42}$$

Using eq. 3.42 the optimal Fourier coefficients are obtained as [Veldhuis (2005):268(7.17)]

$$A_n = \frac{-J_n}{2nI_{nn}} \qquad n = 2, 3, ..., \infty \tag{3.43}$$

Thus, the optimal Fourier coefficients depend only on the integrals I_{nn} and J_n. Based on our inference about Veldhuis assuming $J_n = 0$ for $n = 2...\infty$, the Fourier coefficients A_2 ,...,A_∞ in eq. 3.43 are all zero.

Veldhuis proceeds further to calculate either the chord distribution for a given twist distribution or vice versa, using [Veldhuis (2005):270(7.28)],

$$c_l(\theta)\frac{c(\theta)}{b} = 4\sum_{n=1}^{\infty} A_n \sin(n\theta)(1 + a(\theta)) \tag{3.44}$$

where

$$c_l = c_{l\alpha}\alpha_e(\theta) \tag{3.45}$$

$$\alpha_e(\theta) = \alpha_g(\theta) - (\alpha_{ip}(\theta) + \alpha_{iw}(\theta)) \tag{3.46}$$

for the optimal load distribution as obtained using eq. 3.43. The twist distribution appears to be taken from a typical configuration like Fokker 50 [Veldhuis (2005):291]. By keeping the twist fixed, the search space is characterised by the values of only one parameter (namely the chord) at any stage. Using the expression 3.45, the local lift coefficient c_l may be calculated, and is shown in fig. 3.12. It is seen that c_l touches the very small value of 0.038 at $y/s \simeq 0.3$. Since the twist is not varied in the optimization exercise, the chord has to increase to provide the higher lift force necessary for the optimal load distribution. Therefore, a one dimensional search space is also a contributor for higher chords behind the propeller.

3.4.3 Conclusion

The source of the unrealistic chord distribution obtained by Veldhuis is traced here to errors in his formulation. Since it is not clear either from the publications or the thesis

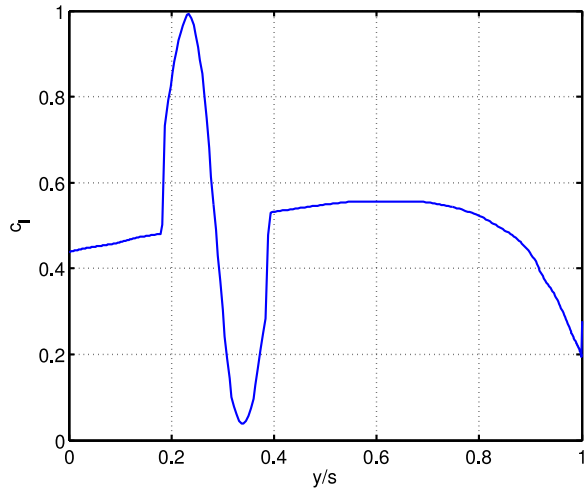

Figure 3.12: Spanwise variation of local lift coefficient computed using Veldhuis's formulation.

of Veldhuis precisely what steps were followed by him to arrive at the chord distribution shown in fig.3.8b, we have attempted to infer the reasons here for the unrealistic chord distribution obtained by him, substantiating it with sufficient reasoning and providing plots wherever necessary. The conclusion we draw is consistent with the reasoning presented. Our approach is consistent with the aerodynamic formulation of Kroo. However our optimization strategy is different from that of either Kroo or Veldhuis, and this leads to the novel planforms that are the subject of this thesis.

Nomenclature

Symbols

a_a	axial velocity factor (v_a/V_∞), speed of sound
a_t	tangential velocity factor (v_t/V_∞)
a'	tangential velocity factor $(v_t/\Omega R)$
a_{cor}	Coriolis acceleration
A	surface area, aspect ratio
A_n	Fourier coefficients
AR	wing aspect ratio
b	wing span
b_f	flap span
B	number of propeller blades
C_{N_p}	propeller normal force coefficient, definition 1, $(= \frac{N_p}{\rho n^2 D^4})$
C'_{N_p}	propeller normal force coefficient, definition 2, $(= \frac{N_p}{q_\infty S_p})$
$C^*_{N_p}$	propeller normal force coefficient, definition 3, $(= \frac{N_p}{q_\infty S_{wing}})$
$C_{N_{\alpha_p}}$	propeller normal force gradient
C_T	propeller thrust force coefficient, definition 1, $(= \frac{T}{\rho n^2 D^4})$
C_d	local two-dimensional drag coefficient
C_D	three-dimensional drag coefficient
C_l	local two-dimensional lift coefficient
C_L	three-dimensional lift coefficient
C_m	pitching moment coefficient
$C_{m,p}$	pitching moment coefficient
$C_{m,y}$	yawing moment coefficient
$C_{m,r}$	rolling moment coefficient
$C_{m,n}$	influence matrix element
C_Y	side force coefficient
C_P	power coefficient
c_p	pressure coefficient, specific heat at constant pressure
c_{p_t}	total pressure coefficient
c_v	specific heat at constant volume
C_Q	torque coefficient
c	chord, speed of sound
$\overline{c}$	mean aerodynamic chord
d	distance
D	(propeller) diameter
D_v	vortex drag
e_t	total energy
f	Prandtl tip loss factor

Figure 3.13: Nomenclature of all symbols used in section 3.4.2

v_a	axial velocity increase
v_t	tangential velocity increase
v_n	normal velocity
V	velocity vector
V	reference velocity
V_e	effective velocity
V_∞	undisturbed reference velocity
$\mathcal{V}$	volume
w_s	vortex sheet velocity
x, y, z	local axis system
x_p, y_p, z_p	propeller position in x, y and z-direction
X, Y, Z	global axis system
α	angle of attack
α_p	propeller angle of attack
α_T	thrust line angle attack
β	yawing angle / local propeller blade angle
γ	specific heat ratio ($=c_p/c_v$)
δ	small increment
δ_f	flap deflection angle
ε	downwash angle, wing twist angle
ε_p	deflection angle of the slipstream tube
Φ	velocity potential
θ	position angle of the propeller blade
θ_s	swirl angle
φ	local angle, perturbation potential
φ_s	vortex sheet angle
Γ	circulation
λ	Lagrange multiplier, wing taper ratio
ρ	air density
σ	solidity factor, source
τ	airfoil camber, wall shear stress
η	efficiency factor
η_p	propulsive efficiency
η_{fa}	free air efficiency
μ	dynamic viscosity, doublet strength
Ω	angular velocity of the propeller
Λ	sweep angle
π	pi ($= 3.1415926$)
ω	angular velocity vector
ω	angular velocity
ξ	dimensionless radius ($= r/R$)

Figure 3.14: Nomenclature of all symbols used in section 3.4.2

Chapter 4
Optimal Wings for Least Drag with Selected Constraints

In chapter 3, a method to analyze a wing-propeller system and a method of optimization to design wing planform shapes with least drag, subject to a variety of cost functions and constraints, was described. To analyze a wing-propeller system, eq. 3.12 has to be solved. The optimization problem described in fig. 3.5 has to be carried out to obtain optimal wing designs. In this chapter, the validation of the numerics used to solve eq. 3.12 for the wing-propeller system and a set of novel wing planform shapes so obtained for various cost functions and constraints are presented.

4.1 Validation and Convergence Study of the algorithm

The PROWING code, described in chapter 3, was validated against the results available in Glauert (1926). Glauert considered a tapered wing in which the chord varies linearly with span. Using his technique of expanding circulation Γ in Fourier series in eq. 3.12 two monoplane coefficients τ and δ were evaluated. Glauert defined the two coefficients (henceforth called Glauert coefficients) as

$$\tau = \frac{\alpha}{A_1} - \frac{\pi \mathcal{R}}{2a_0} - 1 \tag{4.1}$$

$$\delta = \frac{\sum_{k=2}^{n_f} k A_k^2}{A_1^2} - 1 \tag{4.2}$$

where A_k; $k = 1...n_f$ are the Fourier coefficients used to represent circulation Γ (eq. 3.8), n_f is the number of Fourier coefficients, a_0 is the lift curve slope of the aerofoil section and $\mathcal{R}$ is the aspect ratio of the wing.

Fig. 4.1 shows the comparison of the coefficients τ and δ computed using PROWING code with those obtained by Glauert. The coefficients were computed for a wing, to be called the control wing, of aspect ratio 12 and taper ratio 0.5, at a cruise $C_L = 0.4$. The wing uses NACA 63-615 aerofoil section. This particular wing geometry was chosen as it represented the current state of the art. The details of wing geometry were obtained from the design office at National Aerospace Laboratories (NAL) (Narayan (2009), personal

communication). It can be seen in Fig. 4.1 that there is very close agreement between Glauert's values and those computed using PROWING.

The Glauert coefficients could be computed accurately using 16 collocation points (n_c) and 8 Fourier modes (n_f). These numbers were obtained after performing a convergence study as shown in fig. 4.2 (method of solution is described in chapter 3). The values of the Fourier modes with increase in number of collocation points are seen to plot on top of each other (see fig. 4.2).

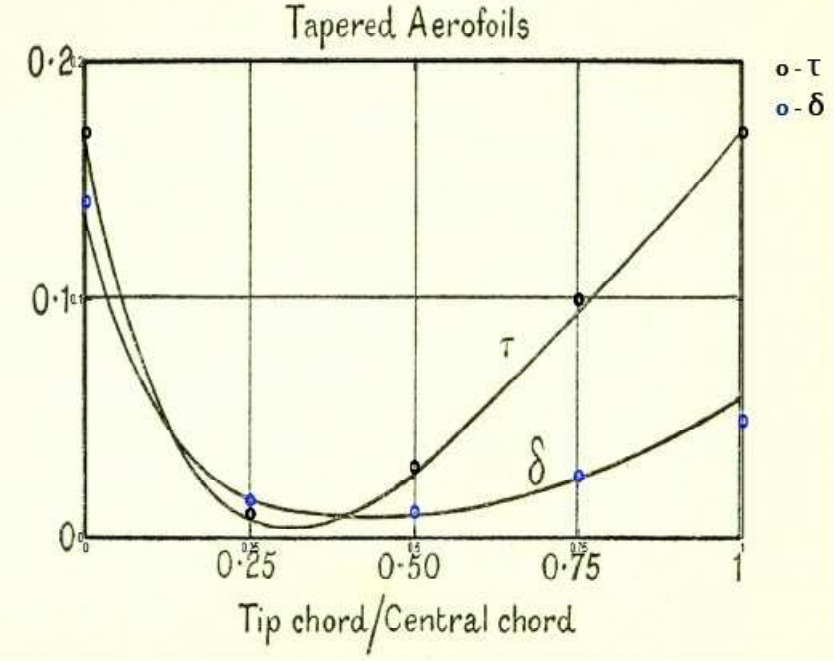

Figure 4.1: plot of variation of Glauert coefficiens with taper ratio = tip chord / central chord. Continuous lines represent the values obtained by Glauert and the circles represent the values obtained by solving eq. 3.12 numerically for a wing-alone case.

For a wing-propeller system, the number of collocation points and Fourier modes are usually larger than in the wing-alone case. This is due to the non-uniformity in the approach velocity. A convergence study was carried out to determine the number of collocation points and Fourier modes which can adequately represent a wing-propeller system.

From fig. 4.3 it can be seen that an adequate number for collocation points and Fourier modes required to represent a wing-propeller system is 160 and 32 respectively. The maximum absolute value of any Fourier mode between 32^{nd} and the 48^{th} has a value of 1.9863×10^{-5} and does not change with increase in number of collocation points beyond 160. Since the computing requirements were not heavy, 320 collocation points and 48 Fourier modes were chosen for the study.

Validation of the optimization part in PROWING was carried out by reproducing the

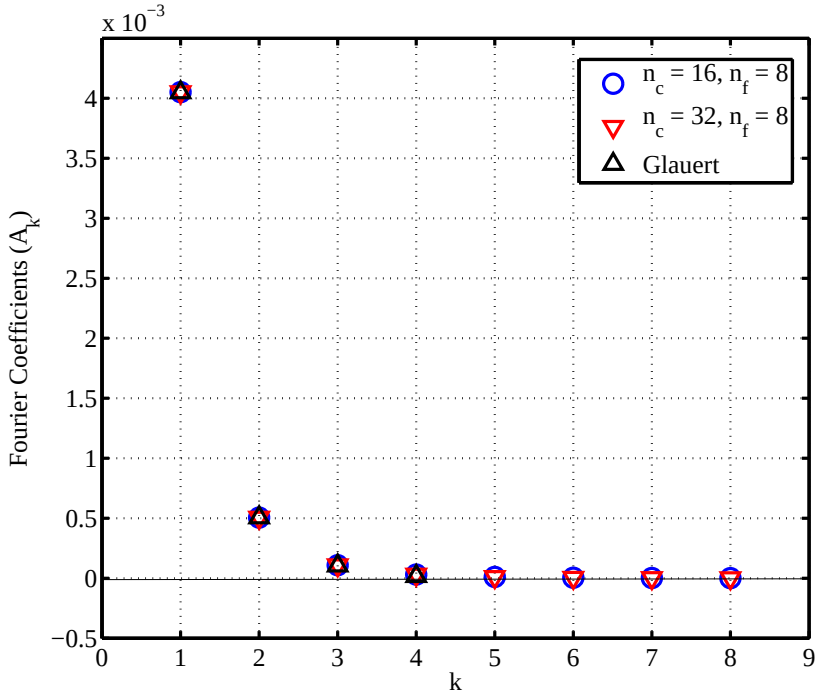

Figure 4.2: Convergence behaviour of Fourier modes with number of Collocation points for wing-alone case. Circles represent Galuert's result which used 4 Fourier modes and 4 collocation points, plusses and crosses indicate results obtained from PROWING for 16 and 32 collocation points respectively with number of Fourier modes equal to 8 in both the cases.

elliptic load distribution for the wing-alone case which is the well-known optimum load distribution for minimum induced drag on a simple wing (Prandtl 1918). Figure 4.4 shows the load distribution for both control and optimal wings.

4.2 Optimal Wing Designs

We now present results of wing optimization in the presence of a propeller for various cost functions and constraints. For easy and quick reference, all the cases that were solved are listed in table 4.1. For all the optimization exercises, the control wing used was of aspect ratio 12, had a taper ratio of 0.5 and a linear washout of 3°. The wing was optimized for a cruise condition at $C_L = 0.4$. Chord and twist were chosen as design variables and were parameterized using Bézier curves. Aerodynamic constraints were the extended lifting-line equation and the cruise lift coefficient. Geometric constraints were wing area, root chord, tip chord and bounds on twist. In addition to these constraints, certain other constraints including structural parameters were also implemented. Those conditions, in addition to the ones mentioned, that were implemented in certain optimization cases are listed in table 4.1. The slipstream velocity needed for optimization was generated using the PROP-EULER code (described in detail in chapter 5). The propeller chosen for wing

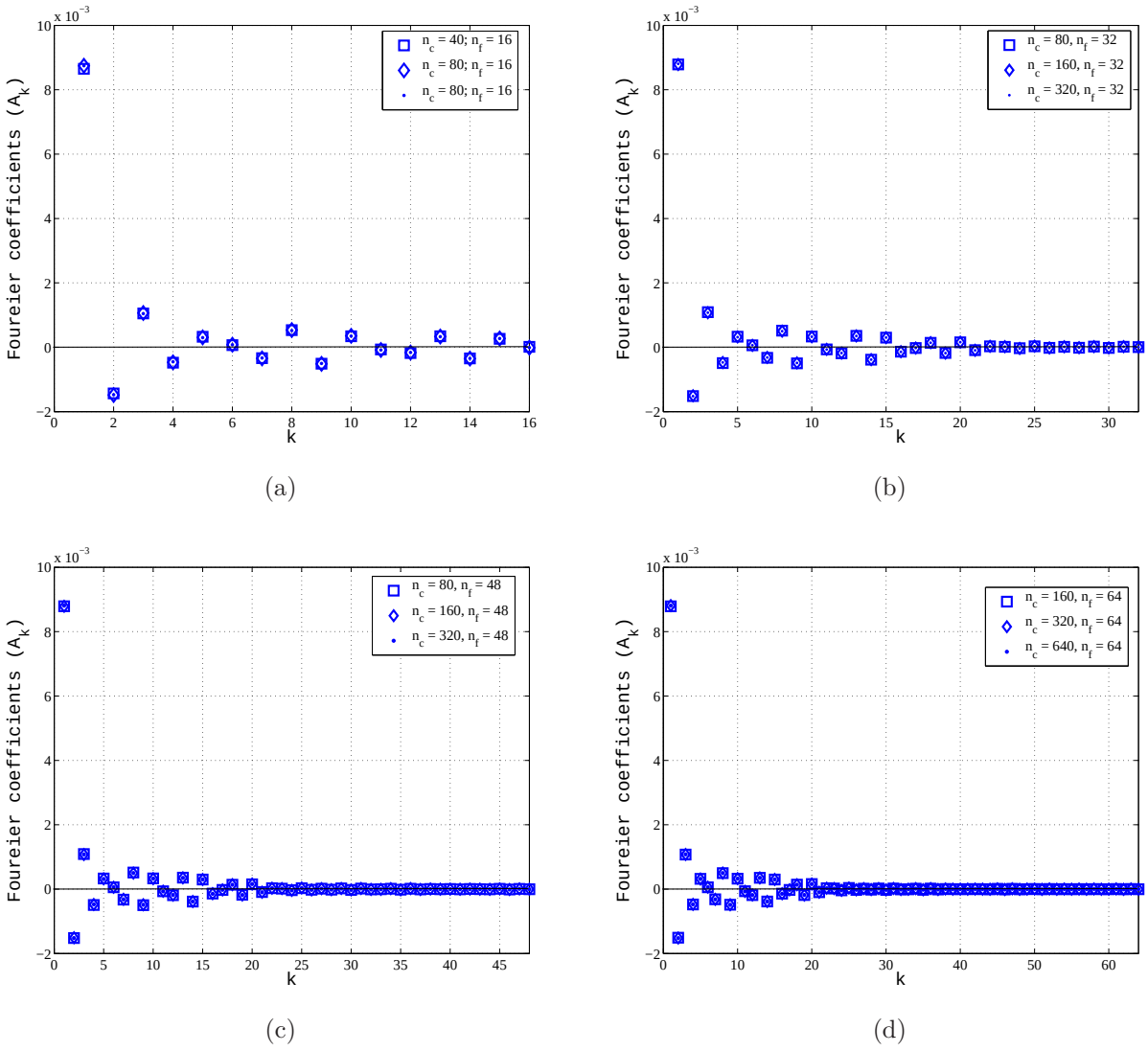

Figure 4.3: Convergence behaviour of Fourier modes with number of collocation points for wing-propeller system

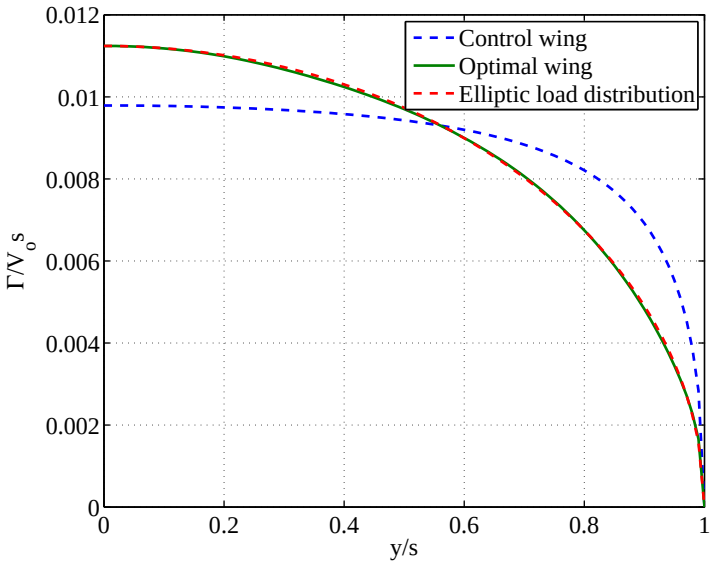

Figure 4.4: Load distribution for both optimal and control wings. Elliptic load distribution for the optimal wing without the propeller checks the optimization routine in PROWING

optimization studies was that mentioned in Hartman & Biermann (1938), except for case 10 for which the propeller used was Hartzell and the geometric details were obtained from C-CAD, NAL, Bangalore.

Numerical values of the constrained variable are

- wing area/ semispan^2 = 0.166
- root chord / semispan = 0.222
- tip chord / semispan = 0.111
- bounds on twist = $-5°$ to $+5°$

4.2.1 Case 1 - Lowest Induced Drag

Optimal wing design for Case 1 is shown in fig. 4.5. In the initial stages, optimization was carried out with the slipstream velocities obtained from Josy (2009), but for all the cases listed in table 4.1 PROP-EULER was used. It is seen that the optimal wing has shorter chords behind each propeller and longer chords on either side of the slipstream. The optimal wing has 8.31% lower induced drag compared to the control wing. Normalised circulation and twist distributions for both control and optimal wings are also shown in the figure. From the plot of normalised ciculation distribution it can be seen that the optimal distribution is not elliptic, which is also plotted for comparison. This is because of the non-uniformity in the approach velocity. It can be seen that the normalised circulation distribution in the propeller-slipstream for the optimal-wing has the same shape as on the control-wing but is lower.

Case No.	Cost function	Additional Constraints*
1	Induced Drag	-
2	Total Drag	-
3	Total Drag	Linear variation of thickness along span between root and tip joined by straight lines at $x/c = 0.2, 0.6$
4	Total Drag	Straight trailing edges
5	Total Drag	Straight trailing edges with linear variation of thickness along span between root and tip joined by straight lines at $x/c = 0.2, 0.6$
6	80% Total Drag + 20% Wing root bending moment	-
7	Total Drag	Root bending moment
8	Total Drag	Twist at root and tip chords were relaxed
9	Total Drag	Linear washout of 5°
10	Total Drag	AR = 8, Linear washout = 2°

Table 4.1: Table indicating the optimization cases solved using PROWING. *Standard constraints (always imposed unless otherwise stated)

An interesting outcome of this circulation distribution is that the induced drag of the control-wing-propeller system was lower than the wing-alone case by 12.2%. This phenomenon was reported first by Kroo (1986) and later by Witkowski *et al.* (1989). Kroo explained it by pointing out that, for a given lift force, the required circulation goes down because of the increased streamwise velocities in the propeller slipstream; hence the induced drag, which depends on the circulation, is also reduced. The optimization process reduces the induced drag further.

The circulation distribution in fig. 4.5 is lower in the region of the propeller slipstream and inboard towards wing root for the optimal wing compared to the control wing, and higher outboard towards the wing tip. This is achieved by having a lower chord in the region behind the propeller and higher chord in the region outboard of the propeller towards the wing tip.

As the number of Bézier modes used to parameterize the chord and twist is increased, the induced drag reduction also increases, but it saturates at around 12.75% as shown in fig. 4.6. The global maximum reduction in induced drag for a given lift force has been computed using the closed form expression given by Kroo (1986). In general the planform gets more wiggly as the number of Bézier modes increases. The incremental saving in drag however becomes marginal beyond about 16 modes as shown in fig. 4.6. Thus substantial gains in drag are already realized with relatively few modes. Fig. 4.7 shows the circulation distribution obtained by both Kroo's closed form expression (eq.3.26) and PROWING. It can be seen that the load distribution obtained from Kroo's expression for global optimum is very close to that obtained from PROWING.

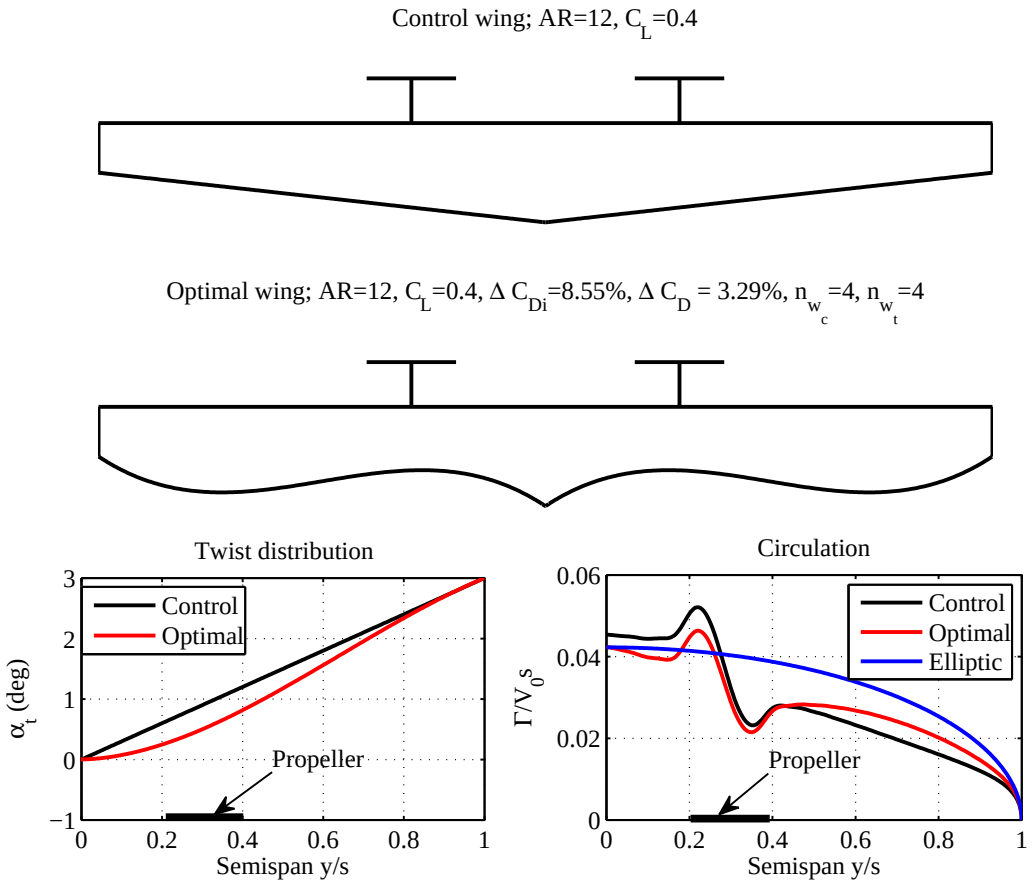

Figure 4.5: Optimal wing design obtained for case 1 designed at $C_L = 0.4$, using $n_{w_c} = 4$ and $n_{w_t} = 4$ having $\Delta C_{Di} = 8.55\%$;$\Delta C_{Di} = C_{Di_{\text{control}}} - C_{Di_{\text{optimal}}}$;

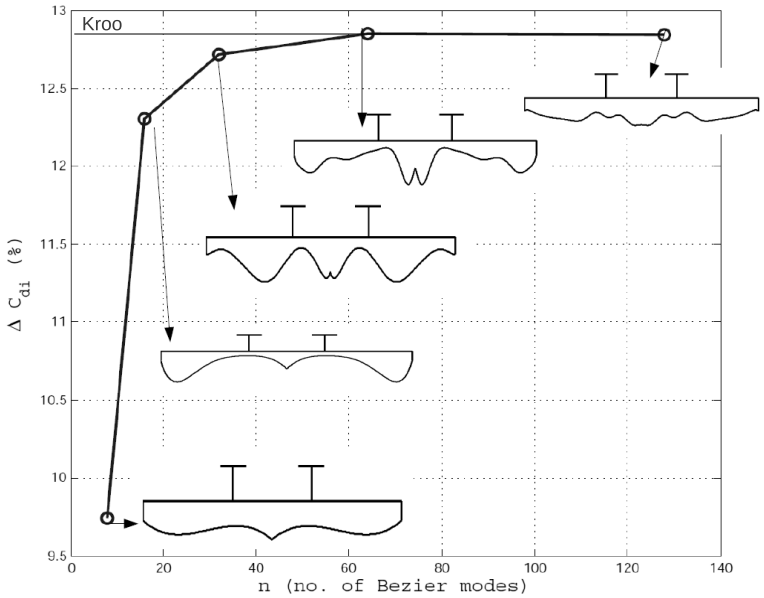

Figure 4.6: Convergence of induced drag reduction, for Case 1, with increase in number of Bézier modes used for shape parameterization. The black horizontal solid line indicating Kroo is the value of the maximum induced drag reduction that can be obtained. This value is computed using Kroo's methodology

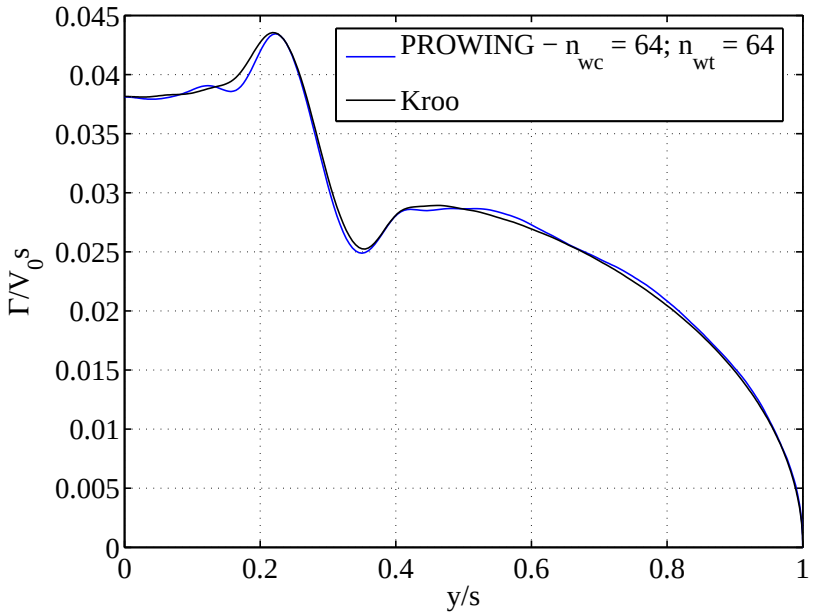

Figure 4.7: Comparison of global optimum; black line obtained using Kroo's equation for global optimum and blue line obtained using PROWING.

4.2.2 Case 2 - Lowest Total Drag

Here we present optimal wing shapes which have lower total drag. The cost function J minimized comprised induced drag D_i and parasite drag D_p,

$$J = D_i + D_p \tag{4.3}$$

Here the parasite drag D_p is defined as

$$D_p = \int_{-s}^{+s} 0.5\,\rho\,V(y)^2\,c_{dp}\,c(y)\,\mathrm{d}y \tag{4.4}$$

where c_{dp} is the profile drag coefficient of the aerofoil section.

In order to compute the total drag we take the profile drag coeffecient (c_{dp}) for the aerofoil section and then evaluate the integral (eq. 4.4 to compute the profile drag (D_p), and then add it to the induced drag (D_i).

The optimal wing shape for this case is shown in fig. 4.8. It has an induced drag reduction of 8.31% and a total drag reduction of 3.37%. The reductions are not significantly different when compared to reductions in case 1. The twist and circulation distributions in fig. 4.8 are qualitatively similar to case 1 results. Since the area is a constraint in the optimization exercise, the parasite drag does not change significantly between optimal and control wing shapes.

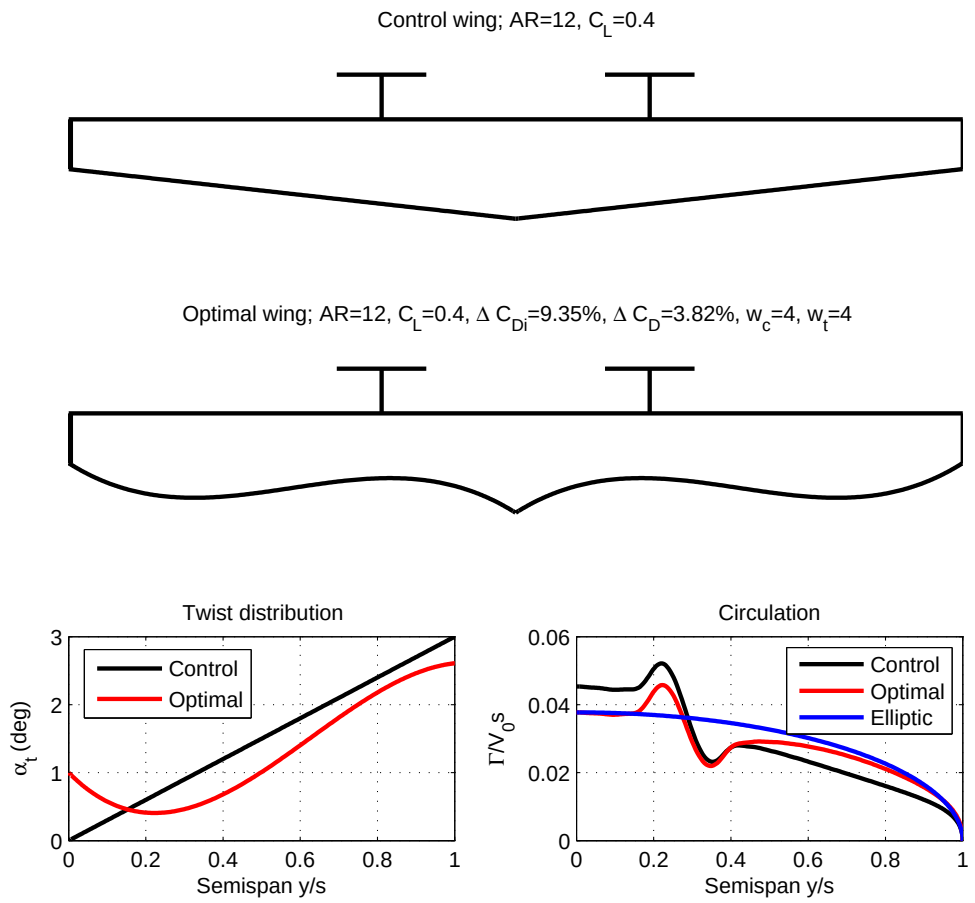

Figure 4.8: Optimal wing design having lowest total drag designed for $C_L = 0.4$ using $n_{w_c} = 4$ and $n_{w_t} = 4$ having $\Delta C_{Di} = 9.35\%, \Delta C_D = 3.82\%$

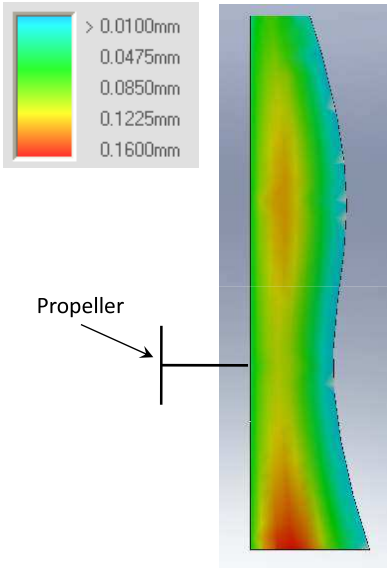

Figure 4.9: Thickness analysis of optimal wing obtained in case 2. Thickness behind the propeller is lower and increases outboard towards wing tip and inboard towards fuselage.

4.2.3 Case 3 - Wing planforms with linear spanwise variation of thickness at $x/c = 0.2$ and 0.6

Optimal wing shapes presented in cases 1 and 2 had shorter chords behind the propeller and longer ones in both outboard and inboard regions. If the aerofoil (including its thickness to chord ratio) is kept the same from wing root to tip, the thickness will no longer then have a linear spanwise variation. Instead the variation will be as shown by the contour plot in fig. 4.9. From the figure it can be seen that the thickness goes down in regions behind the propeller and increases in the regions both inboard and outboard, creating a saddle-like surface behind the propeller. This type of thickness distribution leads to surface undulations and poses structural and manufacturing problems, in particular because inserting spars with depth varying linearly along the span (the preferred fabricating option) will be a challenge.

In order to mitigate this problem we identified two typical x/c locations, 0.2 and 0.6, at wing root and tip as typical of spar locations. These stations were joined by straight lines.Along these lines a linear variation of thickness was prescribed and the optimization exercise was repeated.

Figure 4.10 shows the optimal wing shape for this case. The induced drag reduction obtained is 8.39% and total drag reduction obtained is 4.62%. Comparing the results with cases 1 and 2 it can be observed that the induced drag reduction is not affected by changes in the thickness distribution, which is not unexpected since the wing is of high aspect ratio and thickness effects are of higher order. However total drag reduction obtained is higher by 1.25% when compared to results from case 2.

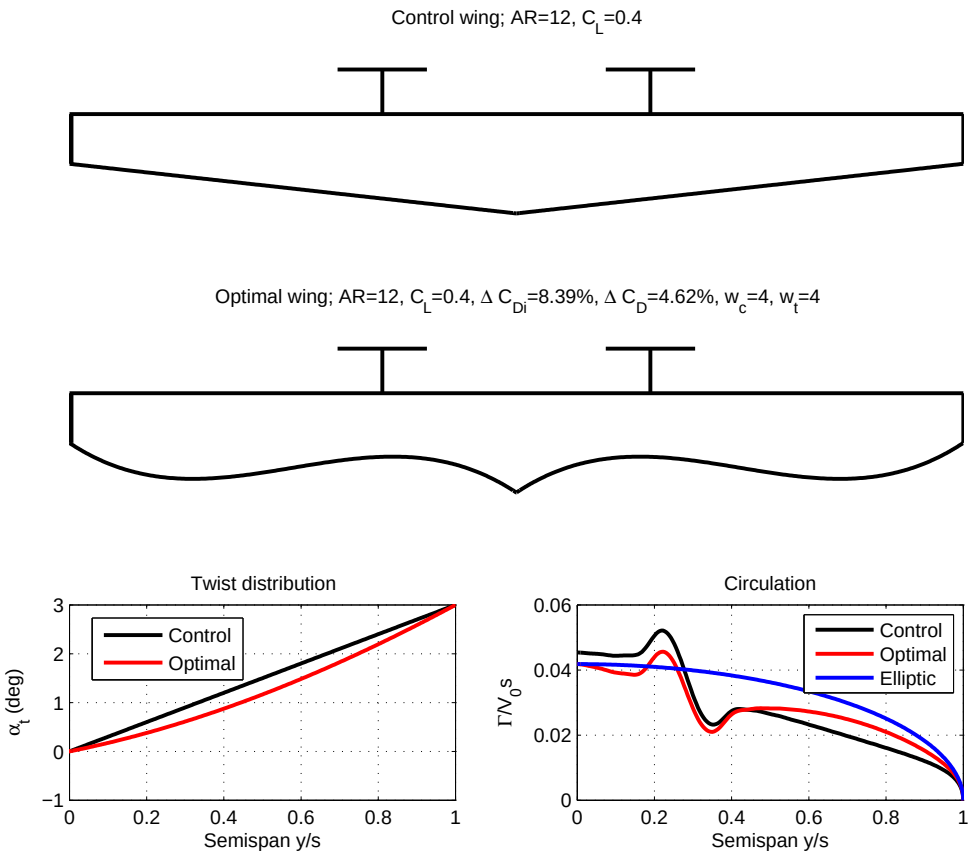

Figure 4.10: Optimal wing design with curved trailing edge and a linear variation of spar thickness along the span, using $n_{w_c} = 4$ and $n_{w_t} = 4$. The wing has $\Delta C_{Di} = 8.39\%, \Delta C_D = 4.62\%$ at $C_L = 0.4$

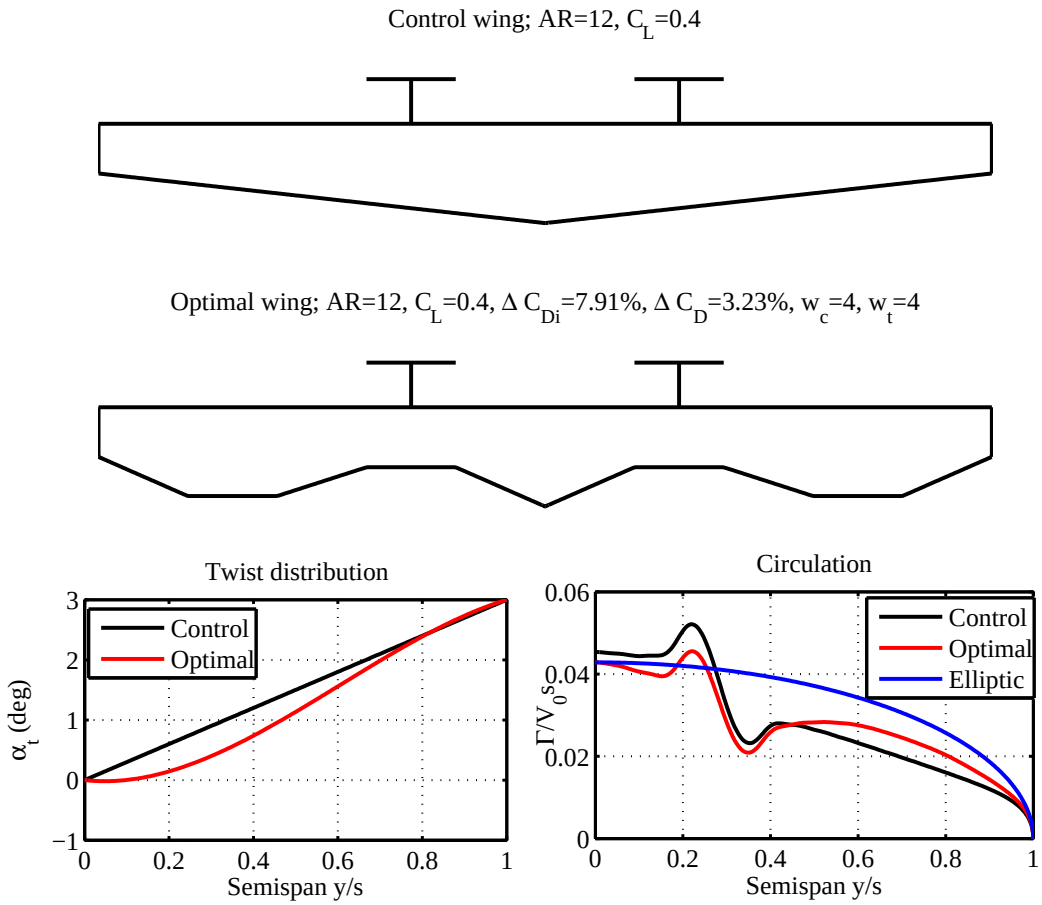

Figure 4.11: Optimal wing design with straight trailing edge using $n_{w_c} = 6$ and $n_{w_t} = 4$. The wing has $\Delta C_{Di} = 7.91\%, \Delta C_D = 3.23\%$ at $C_L = 0.4$

4.2.4 Case 4 - Wing planforms with straight trailing edges

Optimal wing shapes presented so far have curved trailing edges. With certain manufacturing techniques, a straight trailing edge may be preferred. It can also help in attaching flaps and ailerons. This case is worked out and presented here.

Figure 4.11 shows the planform, twist variation and the load distribution on both the control and optimal wings. The reduction in induced drag obtained is 7.91% and in total drag 3.23%.

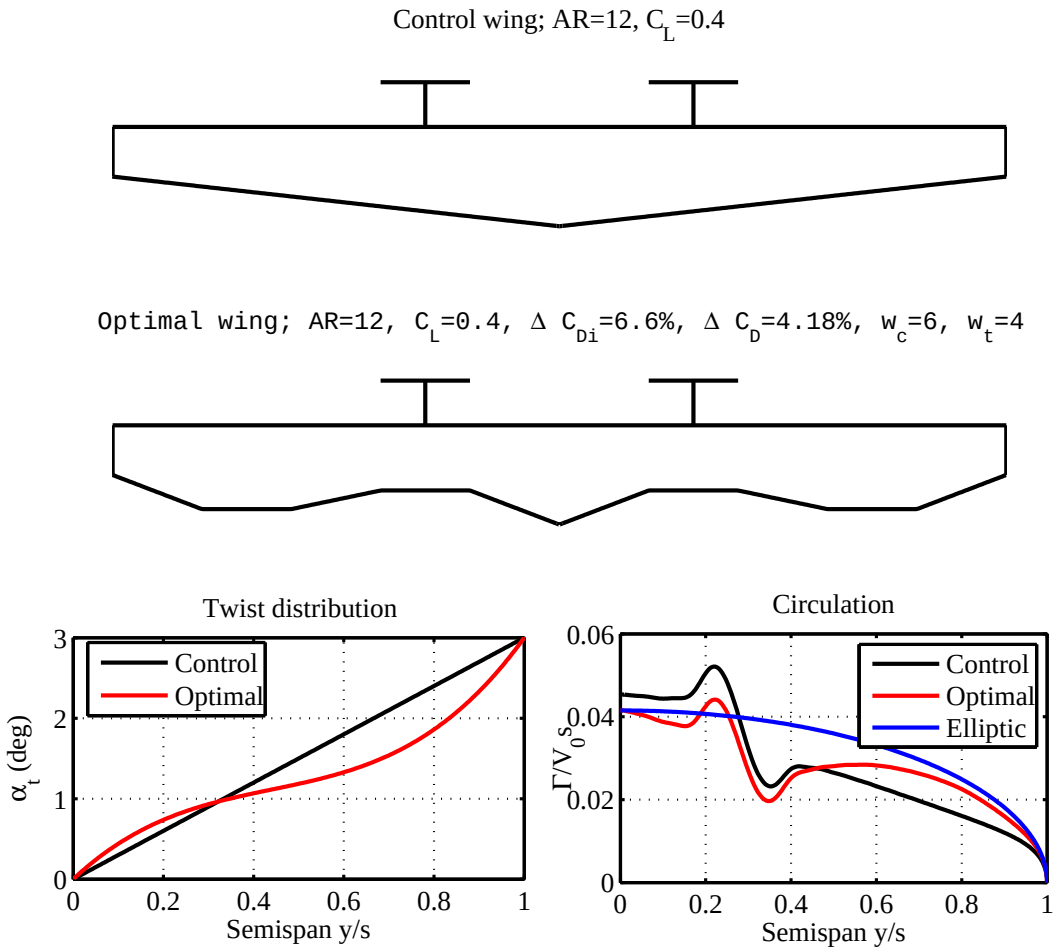

Figure 4.12: Optimal wing design with straight trailing edges and linear variation of spar thickness along the span using $n_{w_c} = 6$ and $n_{w_t} = 4$. The wing has $\Delta C_{Di} = 6.16\%$, $\Delta C_D = 4.18\%$ at $C_L = 0.4$

4.2.5 Case 5 - Straight Trailing edges with linear spanwise variation of spar thickness at $x/c = 0.2$ and 0.6

Combining cases 3 and 4, a new optimization was carried out by specifying both straight trailing edges and linear spanwise variation of thickness at $x/c = 0.2$ and 0.6.

Figure 4.12 shows the optimal wing shape, twist variation and circulation distribution on both the control and optimal wings. The induced drag reduction obtained is 6.61% and total drag 4.18%. The total drag reduction obtained is lower than that obtained in case 3 and higher than that in case 4.

4.2.6 Cases 6, 7: Wing root bending moment

For both control and optimal wings mentioned in case 3 the wing root bending moment (eq. 4.5) was evaluated by integrating over the span the moment due to each section. For the optimal wing the root bending moment turned out to be 0.01223, 10% higher than the control wing (0.0111).

$$\text{WRBM} = \int_0^s l\, y \, \mathrm{d}y \tag{4.5}$$

where l is the lift force per unit span of the aerofoil located at the spanwise station y.

We then carried out an optimization exercise (case 6) which had a weighted cost function so as to minimize both total drag and wing root bending moment WRBM. We gave 80% weight to total drag and 20% weight to wing root bending moment. Figure 4.13 shows the new optimal wing shape. Total drag reduction which was 3.3% in case 3 is now 2.9%. The root bending moment for the optimal wing was now 0.01166 which is higher by 5.09% compared to the control wing-propeller system. So, depending on how crucial the wing root bending moment is in the design process, different weights for the cost function and constraints can be used and wing optimization carried out.

The interaction between wing root bending moment and induced drag has been a subject of study for a long period. Many works on this subject have been published (Jones 1950; Wakayama & Kroo 1995; Iglesias & Mason 2001). All of them carry out an aerodynamic optimization exercise involving constraints from other disciplines. However, the aerodynamic formulation is for turbojet/fan configurations. None of them have considered turboprops. Iglesias & Mason (2001) work out correlations between structural weight and drag reductions for a Boeing-777, which is powered by turbofan engines. For a truboprop similar correlations must be worked out in detail for different missions, with suitable modifications made to the aerodynamic model that include the slipstream effect.

We also evaluated case 7 in which we applied root bending moment of the control wing as an additional constraint. Fig.4.14 shows the optimal wing planform which has an induced drag reduction of 5.73% and a total drag reduction of 3.24%. The optimization was carried out with total number of Bézier modes equal to 64, 32 for chord and 32 for twist, for parameterization. The planform looks unrealistic and manufacturing costs associated with it will increase considerably. In such cases the benefit in total drag would have to be traded carefully with manufacturing costs.

4.2.7 Effect on pitching moment

For the optimal wing obtained for case 3, the effect on pitching moment was computed. The pitching moment, about the point at unit distance upstream to the wing leading edge, was computed by integrating the local lift at each section multiplied by the moment arm. Here the load is assumed to be acting on the wing leading edge. Figure 4.15 shows

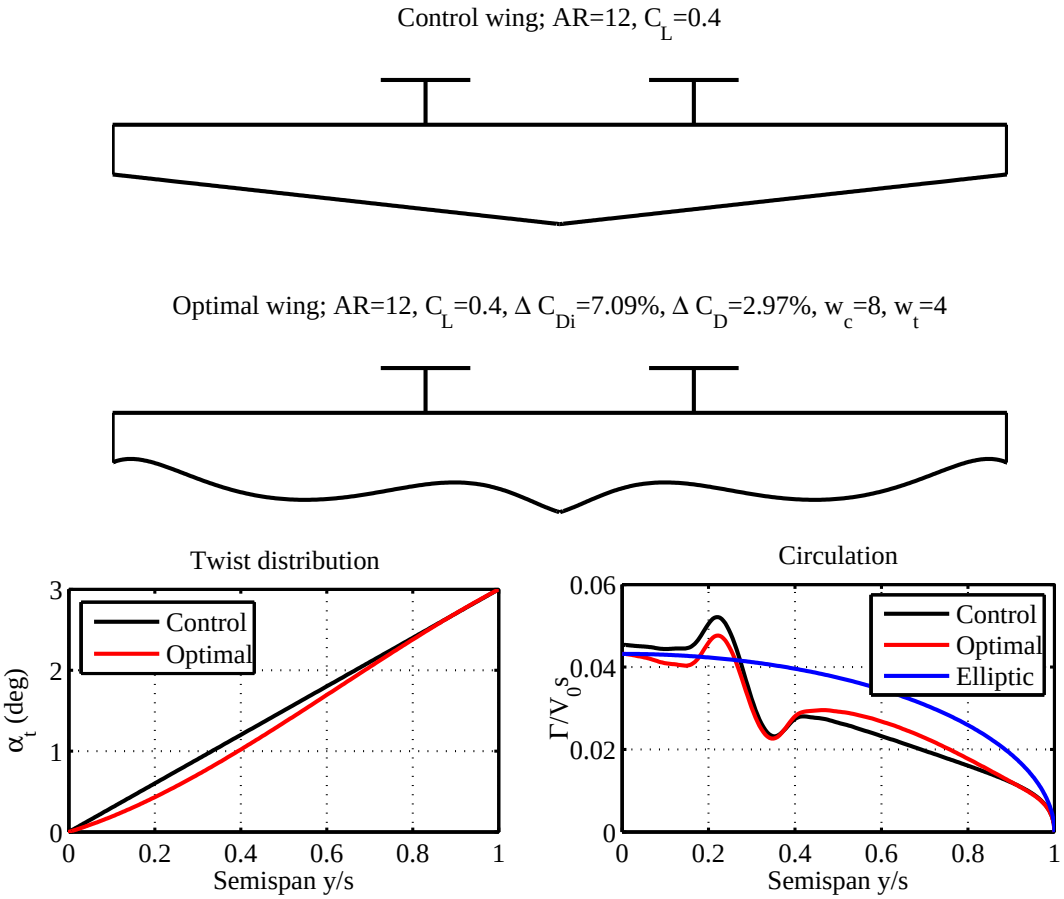

Figure 4.13: Optimal wing design, for case 6, having $\Delta C_{Di} = 7.09\%, \Delta C_D = 2.97\%$

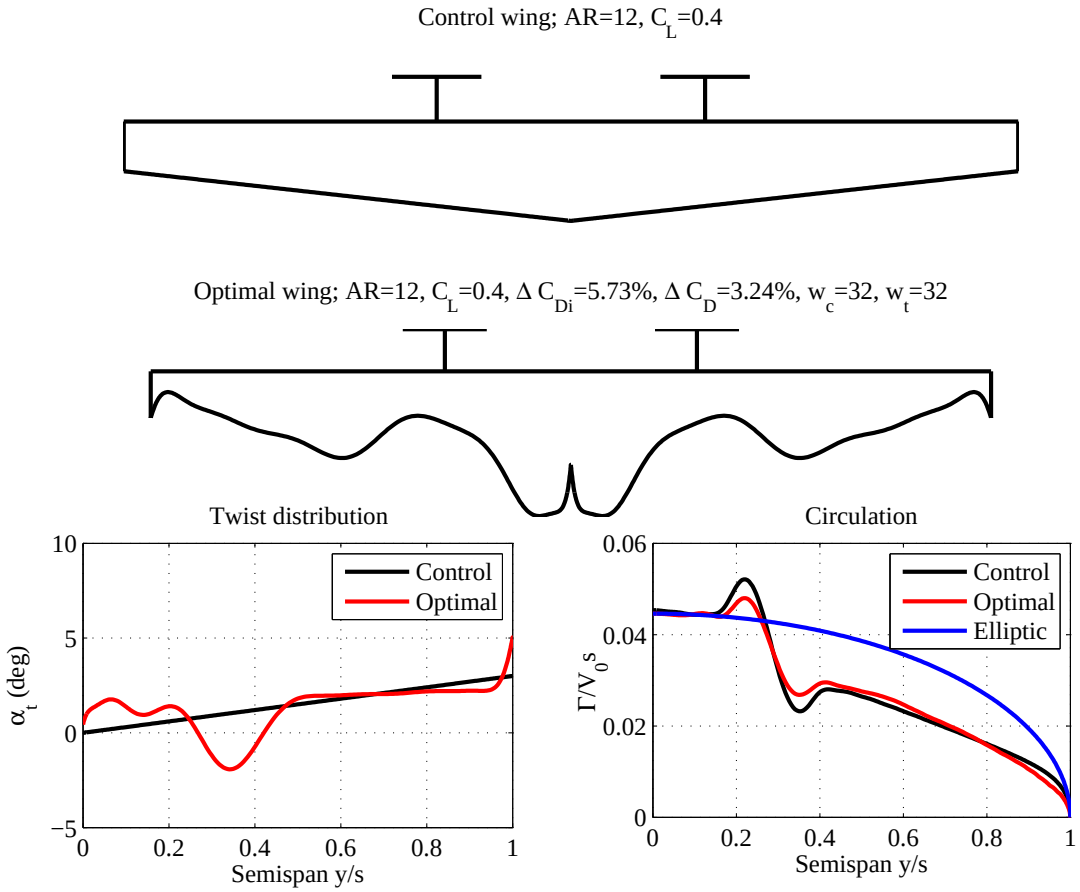

Figure 4.14: Optimal wing design with root bending moment as an additional cosntraint, obtained for $C_L = 0.4$ using $n_{w_c} = 32$ and $n_{w_t} = 32$ having $\Delta C_{Di} = -5.73\%, \Delta C_D = -3.24\%$

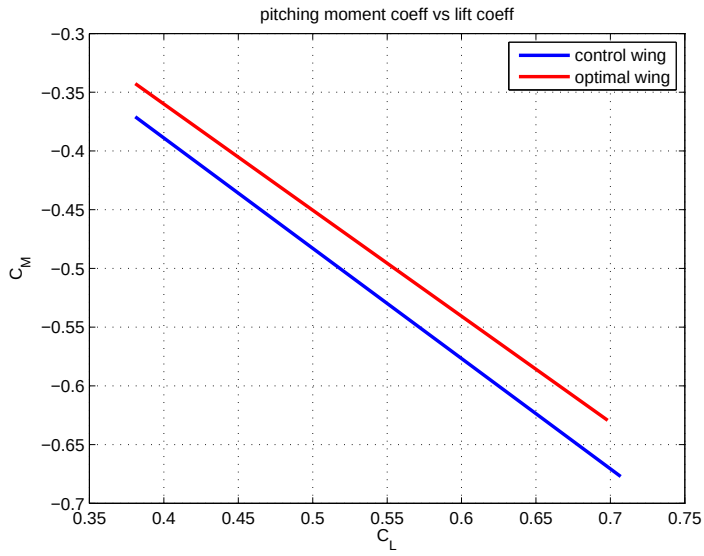

Figure 4.15: Variation of pitching moment coefficient with lift coeffecient for wing planform obtained for case 3

the variation of pitching moment coefficient with the lift coefficient. It can be seen that the slope $\mathrm{d}C_M/\mathrm{d}C_L$ for the optimal wing is also negative with a smaller intercept when compared with the control wing, showing that the trim drag is lower.

4.2.8 Cases 8, 9 , 10 - Wing planforms for CFD and Wind tunnel studies

To check the predictions made by PROWING, high fidelity CFD simulations and wind tunnel tests were carried out (to be described in chapters 5 and 6 respectively). In order to ensure that any differences in drag may be reliably determined, it was decided to generate wing planforms with higher drag reductions. Therefore, optimization was carried out for three cases 8, 9 and 10 respectively.

Optimal wing planform for case 8, shown in fig. 4.16, had an induced drag reduction of 9.35%. This case was chosen for the PROP-EULER simulations as the induced drag reduction obtained was higher than in other candidate cases, and the wing planform did not have sharp changes in the chord distribution.

Optimal wing planform for case 9, shown in fig. 4.17, had a total drag reduction of 11.69% at $C_L = 0.3$. This case was chosen for the RANS simulations using Fluent.

Fig. 4.18 shows four optimal wing planforms with different total drag reductions for a series of proof-of-concept wind tunnel experiments. In order to make the drag reduction sufficiently large so that the reductions can be accurately measured, the optimal wing planform 10a was chosen as it had the highest total drag reduction among the candidates.

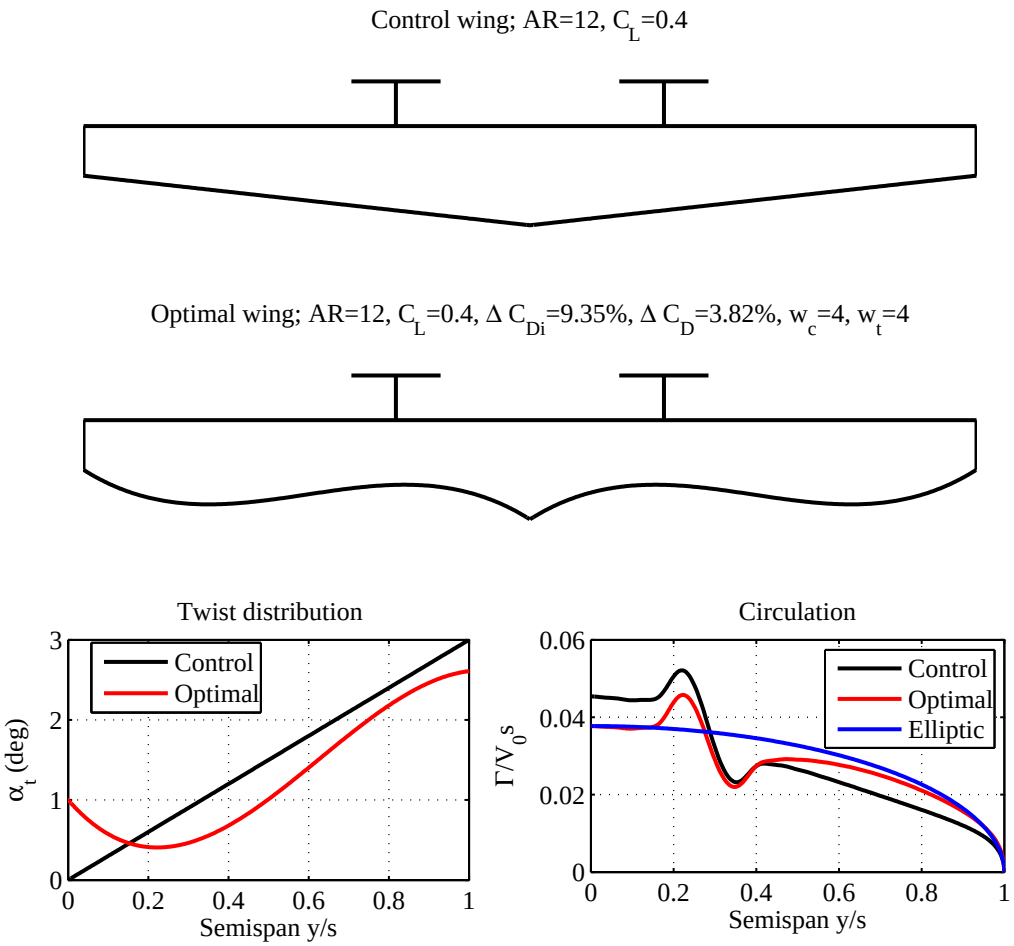

Figure 4.16: Optimal wing design having lowest total drag, designed for $C_L = 0.4$ using $n_{w_c} = 4$ and $n_{w_t} = 4$, having $\Delta C_{Di} = 9.35\%, \Delta C_D = 3.82\%$

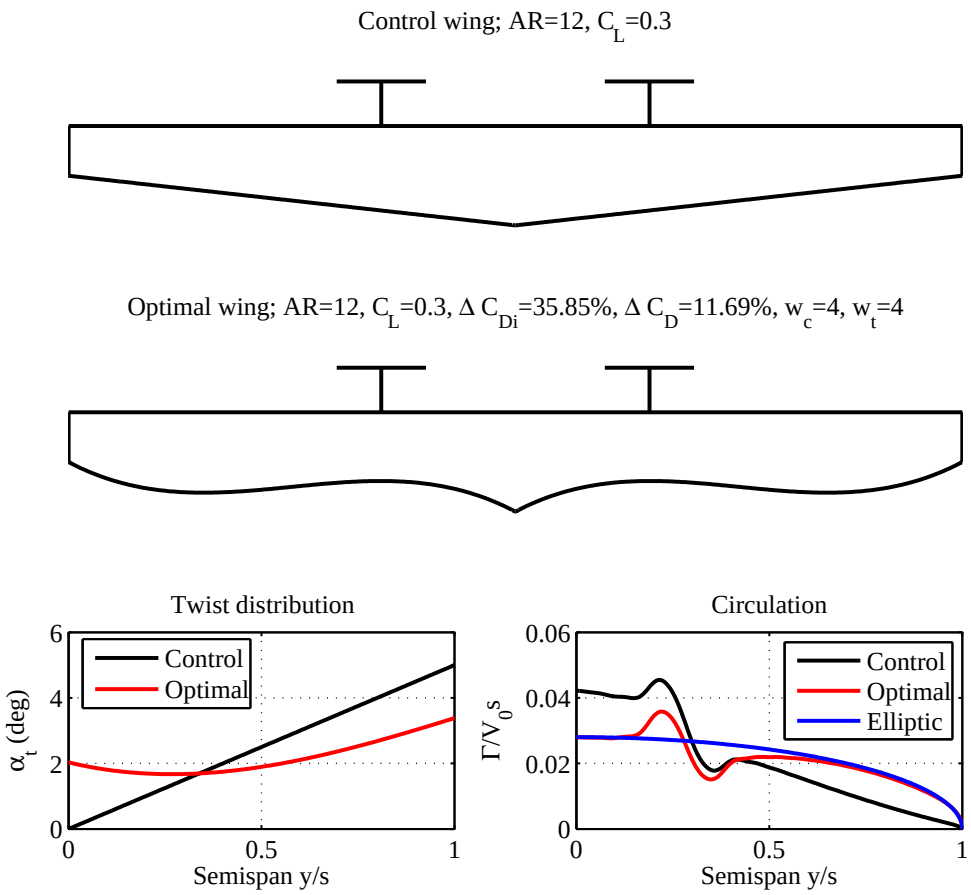

Figure 4.17: Optimal wing design obtained for $C_L = 0.3$ using $n_{w_c} = 4$ and $n_{w_t} = 4$ having $\Delta C_{Di} = 35.85\%, \Delta C_D = 11.69\%$

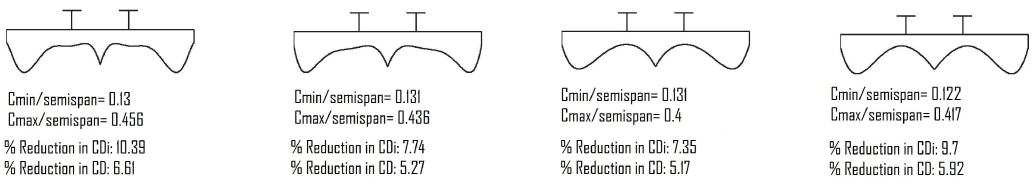

Figure 4.18: Candidate wing shapes generated by PROWING for wind tunnel testing. All of them are of $\mathcal{AR}$ 8.

Chapter 5
High Fidelity CFD Validations

Using an extended lifting-line theory coupled to an optimizer (PROWING, described in chapter 3), novel wing planform shapes have been generated and reported in chapter 4. These planforms were optimized for drag with different constraints, mostly at a cruise lift coeffecient of 0.4. To check the accuracy of predictions made using PROWING, which is a relatively low fidelity model for wing-propeller systems, a set of high fidelity CFD simulations were performed.

Since the extended lifting line theory used in PROWING is inviscid, a natural choice to check the reductions in induced drag was an Euler (inviscid) code. As Euler codes including propellers are not easily available, one (PROP-EULER) was specially developed for the purpose. The propeller is modelled by a Blade Element Theory (henceforth called BET) module, also developed for the purpose. This module is used to provide source distributions of momentum and energy on an infinitesimally thin actuator disk that represents the propeller in the PROP-EULER code. The details of the PROP-EULER code and results of simulations using it are presented in subsequent sections.

Simulations using PROP-EULER account only for 3D effects and not viscosity. In reality there is viscosity and the flow is mostly turbulent for the Reynolds numbers encountered in flight. Therefore, to assess the performance of optimal wing designs taking into account the boundary layer in addition to 3D effects, a RANS code (Fluent in this case) was used. Since Fluent did not have a simple method to handle propellers, the BET module developed for PROP-EULER code was coupled employing the User Defined Functions (UDF) available on Fluent. The use of Fluent is not intended to be a replacement of the Euler codes as results from RANS simulations are dependent on the turbulence model adopted. Use of Fluent along with UDFs to assess the total drag reductions predicted by PROWING eliminated the need to develop a RANS code and helped in getting results early. Results from Fluent simulations are reported in subsequent sections.

5.1 PROP-EULER Code

The PROP-EULER code comprises two parts, namely the Euler code and the Blade Element Theory module. First, details on the structure of the code and its validation are presented, and then the results.

5.1.1 The Euler code

The Euler code developed for the purpose uses an unstructured-mesh, finite-volume based code that solves the 3D invisicid momentum equations

$$\frac{\partial U}{\partial t} + \frac{\partial}{\partial x}\left(G_x\right) + \frac{\partial}{\partial y}\left(G_y\right) + \frac{\partial}{\partial z}\left(G_z\right) = 0 \tag{5.1}$$

where U is the vector of conserved variables and G_x, G_y and G_z are the flux vectors along the coordinate directions x, y and z respectively, given by

$$U = \begin{bmatrix} \rho \\ \rho u_x \\ \rho u_y \\ \rho u_z \\ \rho e \end{bmatrix} \quad G_x = \begin{bmatrix} \rho u_x \\ p + \rho u_x^2 \\ \rho u_x u_y \\ \rho u_x u_z \\ (p + \rho e)\, u_x \end{bmatrix} \quad G_y = \begin{bmatrix} \rho u_y \\ \rho u_x u_y \\ p + \rho u_y^2 \\ \rho u_y u_z \\ (p + \rho e)\, u_y \end{bmatrix} \quad G_z = \begin{bmatrix} \rho u_z \\ \rho u_x u_z \\ \rho u_y u_z \\ p + \rho u_z^2 \\ (p + \rho e)\, u_z \end{bmatrix} \tag{5.2}$$

Here, ρ is density, u_x, u_y, u_z are the components of fluid velocity along x, y, z directions respectively, p is pressure and e is the total energy per unit mass, given by

$$e = \frac{p}{\rho\left(\gamma - 1\right)} + \frac{1}{2}\left(u_x^2 + u_y^2 + u_z^2\right) \tag{5.3}$$

Eq. 5.1 is solved numerically using a second order positivity-preserving KFVS (Kinetic Flux Vector Splitting) scheme (Ghosh *et al.* 1998), which employs reconstruction of the entropy variables called q-variables (Deshpande 1986). It has been shown that the use of q-variables gives a computationally efficient code that yields smooth solutions (Ghosh *et al.* 1998). The KFVS scheme was chosen because of the considerable experience with the technique in the JNC group (Anil 2008).

Many workers in the past have developed Euler codes to study different aspects of KFVS schemes, but they have all been tied to specific problems. Modifying them to use it for our application was not an easy task. Therefore, an Euler code was developed from scratch. Unstructured grids were used to discretize the domain, and were generated using GAMBIT (GAMBIT 2004). Implicit time stepping based on LUSGS (Lower Upper Symmetric Gauss Siedel) was used for faster convergence (Jameson & Yoon 1986). The code has been parallelized using domain decomposition. METIS (Karypis & Kumar 1998) was used for decomposing the mesh into domains.

5.1.2 Validation

Transonic flow past the Onera M6 wing was chosen as the test case for validation of the Euler code. This case has often been chosen to assess the performance of numerical schemes (Praveen 2004; Anil 2008). For the present study, this case was chosen to check

the correctness of the code. Even at other mach numbers, the scheme has performed well (Anil 2008).

The free stream was at a mach number of 0.8395 at an angle of attack of 3.06°. The flow results in a λ-shock structure on the suction surface of the wing (seen in experiments) which can also be seen by plotting pressure contours obtained from the Euler code as shown in fig. 5.1. The coordinate system of the wing is shown on the top right of fig. 5.1: x is along the chord, z is along the span and z is normal to xy plane. The freestream is in the positive x-direction.

Quantitative surface pressure comparisons at 20%, 44%, 65% and 90% of semi-span are shown in figs. 5.2 to 5.5. C_p distribution at 20% semispan, shown in fig. 5.2, has a much stronger shock when compared to the experimental data. This is because, in the CFD simulation, the wing root is attached to a symmetry plane, whereas in experiments, it is attached to the wind tunnel wall. The effects at the wing root in the wind tunnel are not captured in numerical simulation because of the symmetry boundary condition used at the wing root. This is also observed in Anil (2008). However, at other locations the C_p distribution is in good agreement with experimental values of Schmitt & Charpin (1979).

5.2 Propeller Modeling

5.2.1 Theory

Here the propeller is modeled as an infinitesimally thin rotating actuator disk which not only produces a pressure jump across it and accelerates the flow along the axis of the propeller, but also imparts a swirl to the flow (hence the word "rotating") (Rajagopalan 1989; Lötstedt 1995). This is accomplished by considering the forces that the propeller imparts to the fluid as source terms along all the three directions in the momentum equations and the energy equation. If x is along the propeller axis, then the sources in y and z directions impart an angular and radial momentum to the fluid passing through the disk. The source terms are zero everywhere except in the region where the actuator disk is present. To estimate the source strengths, a distribution of force densities on its surface in all the three directions is required, which when integrated over the surface area of the finite volume abutting the disk, gives the average force acting on that particular element of area. These forces, converted to force densities (force per unit area), act as source terms in eq. 5.4.

By coupling the whole-field solver and the rotating actuator disk, the slipstream is captured as a part of the overall flow solution. The forces are estimated using blade element theory and scaled to an equivalent disk.

The Euler equations including source the terms that represent the propeller effects are

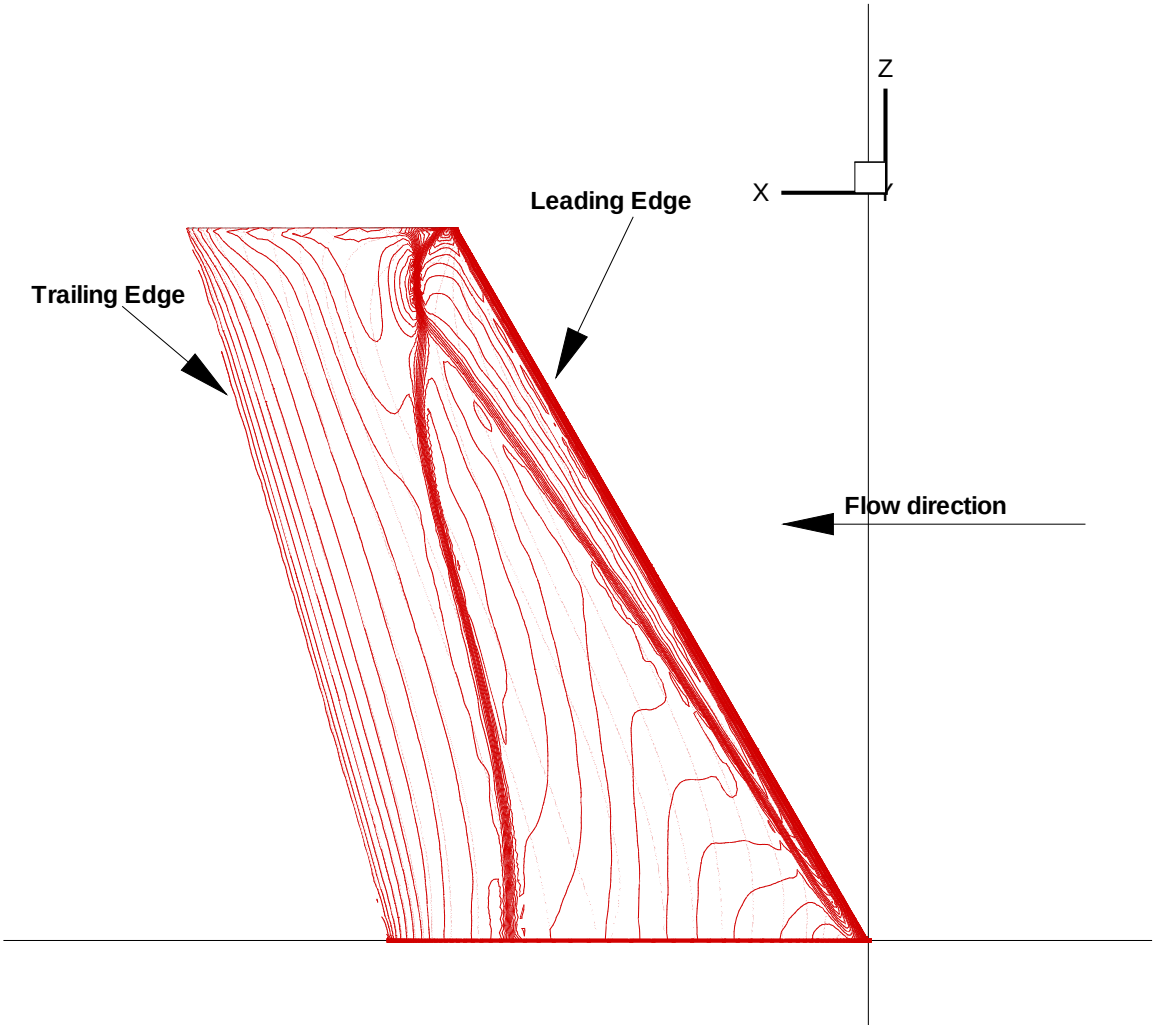

Figure 5.1: Pressure contours on the surface of Onera M6 wing obtained using PROP-EULER code. λ-shock structure is seen on the suction side of the wing.

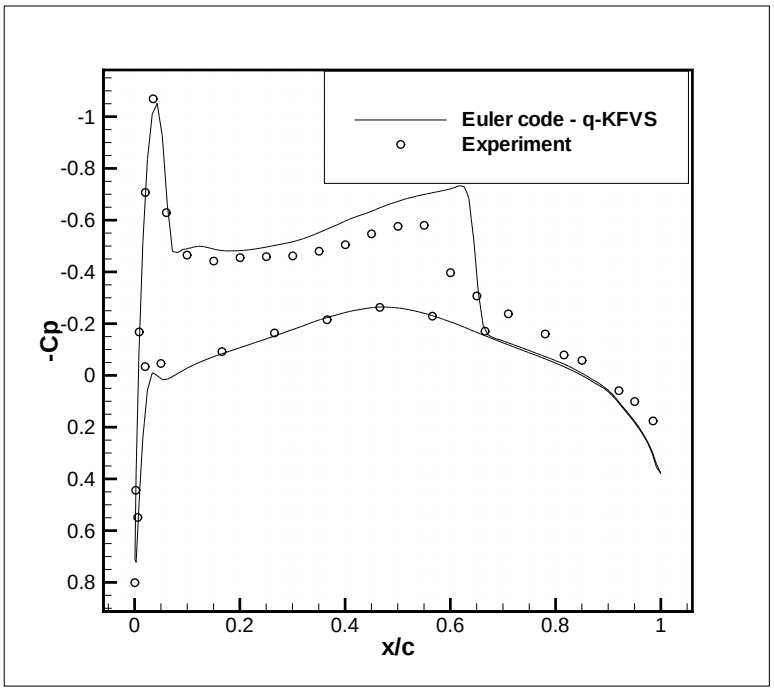

Figure 5.2: Surface pressure coefficient at 20% semi-span

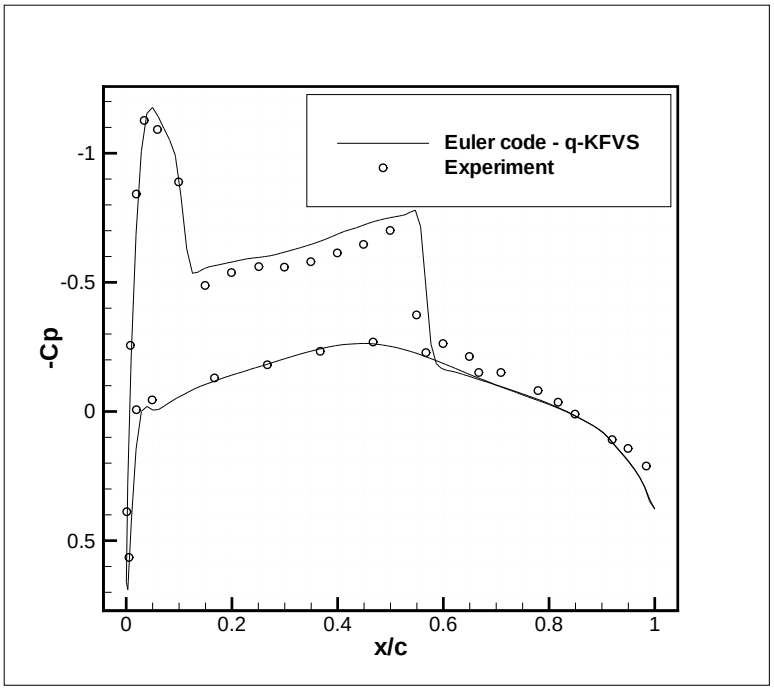

Figure 5.3: Surface pressure coefficient at 44% semi-span

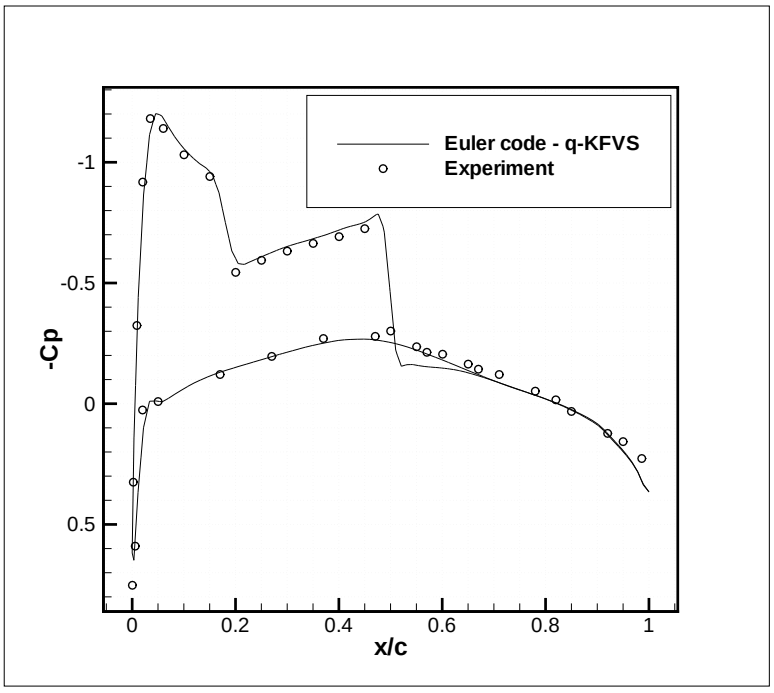

Figure 5.4: Surface pressure coefficient at 65% semi-span

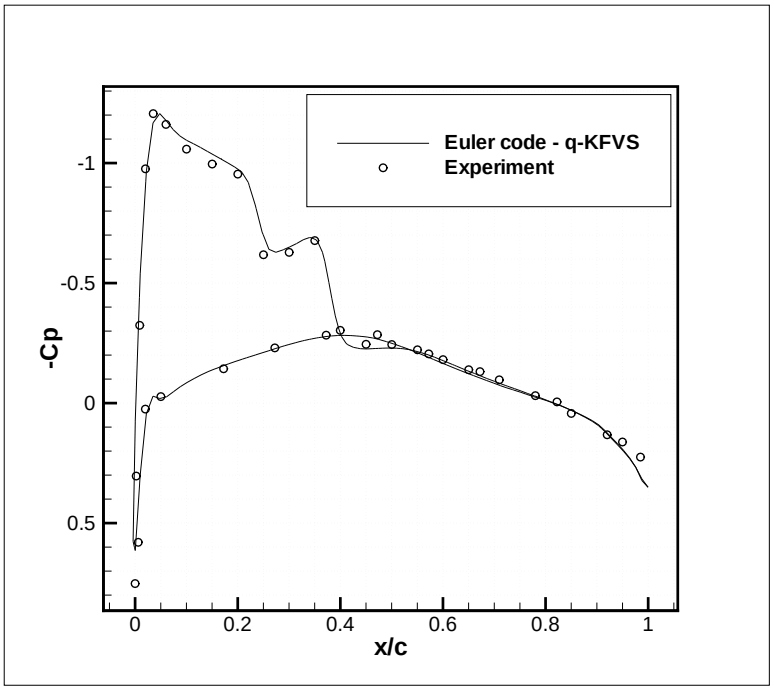

Figure 5.5: Surface pressure coefficient at 80% semi-span

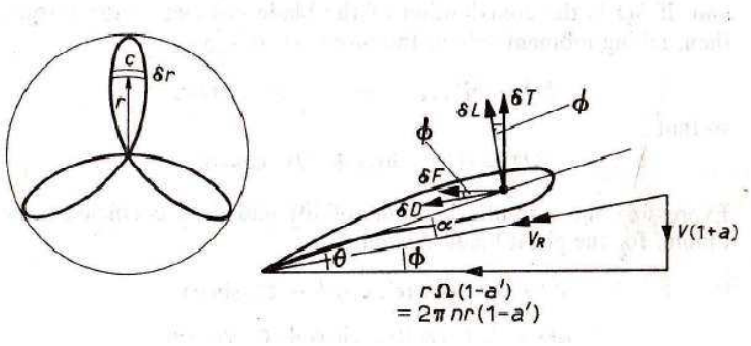

Figure 5.6: Velocity diagram for an aerofoil section of a propeller blade (figure taken from Clancy (1975))

$$\frac{\partial U}{\partial t} + \frac{\partial G_x}{\partial x} + \frac{\partial G_y}{\partial y} + \frac{\partial G_z}{\partial z} = S \tag{5.4}$$

where the vector of source terms is given by

$$S = \begin{bmatrix} 0 \\ S_x \\ S_y \\ S_z \\ S_e \end{bmatrix} \tag{5.5}$$

The first entry represents the mass source (zero strength), S_x, S_y, S_z are the momentum sources in x, y and z directions respectively and S_e is the energy source given by

$$S_e = u_x S_x + u_y S_y + u_z S_z \tag{5.6}$$

5.2.2 Coupling of Blade Element module to the flow solver

A brief description of blade element theory (Clancy 1975) is presented in this subsection, following which a method of calculating the strengths of the source terms is described in detail.

Fig. 5.6 shows the force vector diagram for an aerofoil section at a certain radius r of a propeller blade. Referring to fig. 5.6 the forces normal and perpendicular to the resultant velocity V_R, represented by δL and δD respectively on the element δr, are given by

$$\delta L = 0.5\, c_l\, \rho\, V_R^2\, c\, \delta r \tag{5.7}$$

$$\delta D = 0.5\, c_d\, \rho\, V_R^2\, c\, \delta r \tag{5.8}$$

where c_l and c_d are the lift and drag coefficients of the aerofoil section of the propeller blade at radius r, V_R is the relative velocity of air at the aerofoil section defined as the vector sum of $V(1+a)$ and $r\Omega(1-a')$ with Ω representing the angular velocity, a and a' representing the axial and rotational inflow factors respectively, and V is the flight speed.

If ϕ is the angle between this relative velocity V_R and the plane of the propeller rotation, we have

$$\tan\phi = \frac{V(1+a)}{r\Omega(1-a')} \tag{5.9}$$

If N and R represent the total number of blades and the radius of the propeller respectively, then the total thrust T and the total torque Q are given respectively by

$$T = \int_0^R N\, 0.5\, \rho\, V_R^2\, c\, (c_l \cos\phi - c_d \sin\phi) \mathrm{d}r \tag{5.10}$$

$$Q = \int_0^R N\, 0.5\, \rho\, V_R^2\, c\, r\, (c_l \cos\phi - c_d \sin\phi) \mathrm{d}r \tag{5.11}$$

If we consider the disk approach to model the propeller, then the total thrust on the disk is given by

$$T = \int_0^R \int_0^{2\pi} \sigma(r)\, r\, \mathrm{d}\theta\, \mathrm{d}r = \int_0^R \sigma(r)\, 2\pi r\ \mathrm{d}r \tag{5.12}$$

where σ is the thrust density.

Equating eqs. 5.12 and 5.10 we get an expression for thrust density given by

$$\sigma(r) = \frac{N\, 0.5\, \rho\, V_R^2\, c\, (c_l \cos\phi - c_d \sin\phi)}{2\pi r} \tag{5.13}$$

Similarly we get the torque density τ as

$$\tau(r) = \frac{N\, 0.5\, \rho\, V_R^2\, c\, r\, (c_l \sin\phi + c_d \cos\phi)}{2\pi r} \tag{5.14}$$

Therefore, at any given radius, torque and thrust densities can be calculated using eqs. 5.13 and 5.14, which is then integrated over the area of the surface of the finite volume abutting the disk to obtain the surface force.

A schematic representation of the rotating actuator disk implementation is shown in fig. 5.7. During the operation of the code, if a face of a finite volume element is encountered on the actuator disk (bounded by black lines), then using its centroid values the radius and the angular location, are computed. The veocities u_x, u_y, u_z from the upstream cell are then read (bounded by saffron lines) and are passed onto the blade element module, along with the computed values of radius and angular location to compute the source strengths (S_x, S_y, S_z) . These source strengths are then added to the downstream cell

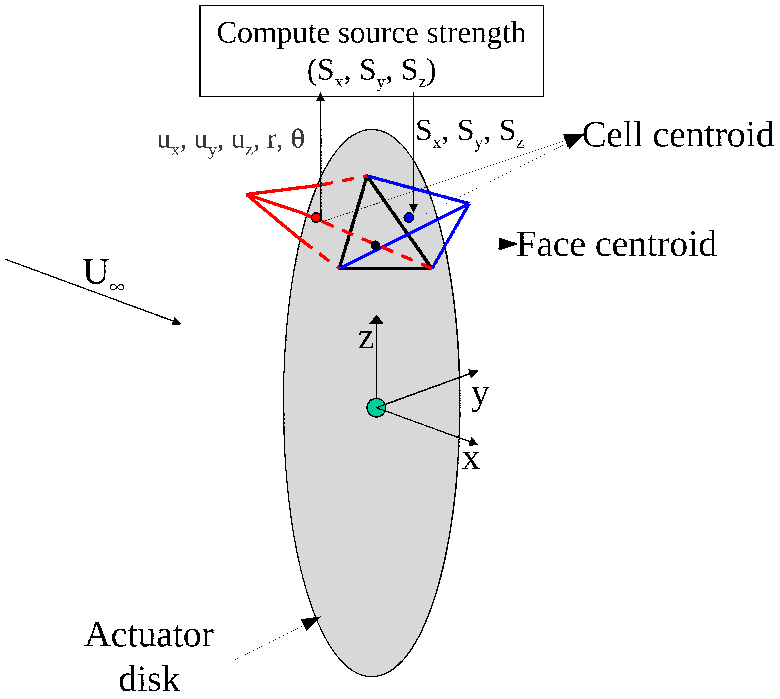

Figure 5.7: Schematic description of propeller handling in PROP-EULER

(bounded by blue lines) as source terms to the momentum and energy equations.

While carrying out the numerical simulation,

- c_l and c_d values for aerofoil sections at prescribed radii are computed for a range of angles of attack by prescribing the local flow conditions (i.e. sum of flight speed (V) and tangential velocity ($r\Omega$)) and given as an input to the blade element module (these coefficients are computed here using the XFOIL code (Drela & Giles 1987));
- aerodynamic coefficients for an aerofoil at any radius in between two discrete stations (considered in the previous step) are computed using the coefficients of adjacent stations by linear interpolation;
- aerodynamic coefficients for an aerofoil at any angle of attack in between the two angles of attack considered in step 1 are computed using the coefficients of adjacent angles of attack by spline interpolation;
- thrust and torque densities at any radius are then computed using the aerodynamic coefficients and the velocities at the cell centres (located half cell width away from the actuator disk).

5.2.3 Validation

Experimental results from Hartman & Biermann (1938) on propeller with R. A. F. 6 aerofoil blade sections were used for validating the propeller module. This particular case

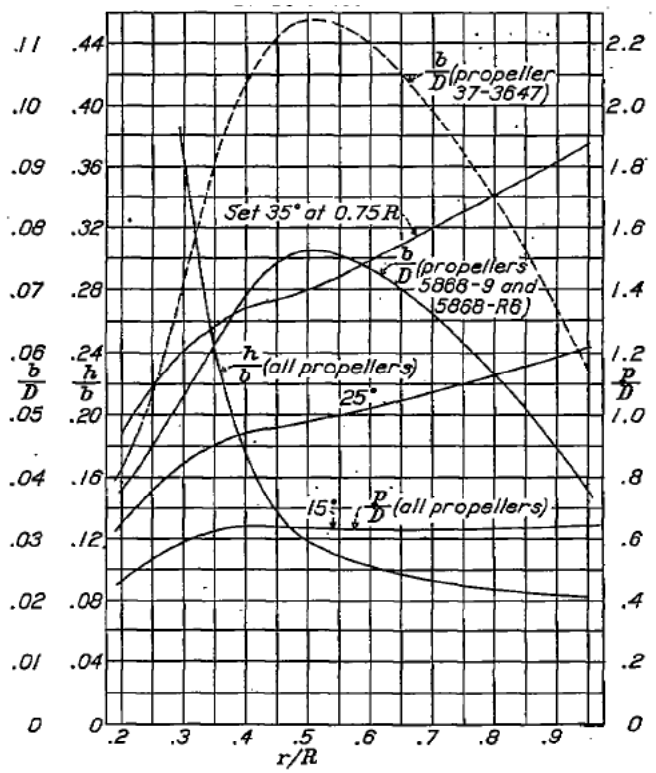

Figure 5.8: Description of propeller blade geometry used for validation of blade element module (figure taken from Hartman & Biermann (1938))

was chosen because all the geometric details needed to model the propeller as an actuator disk in the Euler code were available in the report.

Details of the propeller are as follows:

- Diameter: 10 ft
- Number of blades: 4
- Blade aerofoil section: R. A. F. 6
- Propeller blade geometry as shown in fig. 5.8. Pitch setting of 25° at 75% radius was considered.
- Propeller speed: 1000 rpm

Using the chord, pitch and aerofoil thickness variation along the radius of the propeller given in fig. 5.8, aerofoils were constructed and their corresponding drag polars were computed using XFOIL. These act as an input to the propeller module.

CFD simulations were carried out for advance ratios 1, 1.1, 1.2 and 1.3 and for each case the thrust coefficient was computed. Fig. 5.9 shows the variation of thrust coefficient with advance ratio. The continuous line represents experimental results from Hartman & Biermann (1938) drawn through the points obtained after digitizing fig. 5.10

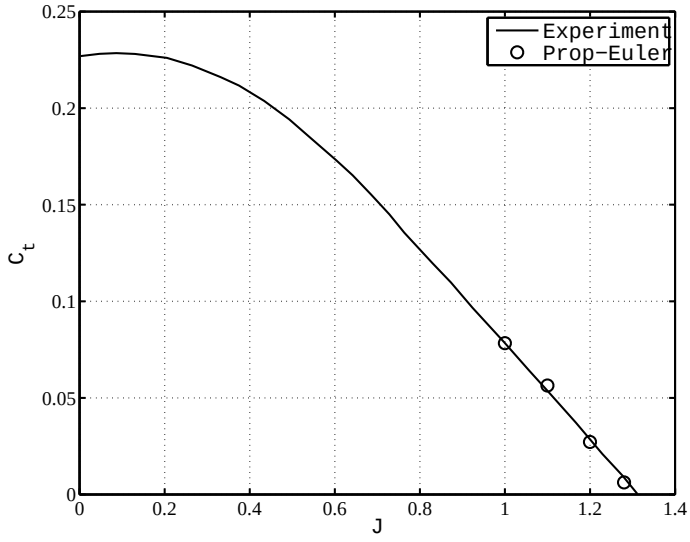

Figure 5.9: Plot of thrust coefficient versus advance ratio showing the validation of Prop-Euler code

in their report. The circles in fig. 5.9 represent the data obtained from the present Prop-Euler code. It can be seen that there is close agreement between the numerical simulations and experimental data.For advance ratios below 1, the free stream mach numbers were becoming very low (< 0.1), which posed difficulties in running the compressible code. Therefore simulations for advance ratios greater than or equal to 1 were carried out. Figure 5.11 shows the flow chart of the PROP-EULER code.

5.3 Use of Prop-Euler code on optimal wing design

The validated Prop-Euler code is used to compute the flow past both control and optimal wing-propeller systems. Case 8, described in chapter 3, was chosen for the validation exercise. The optimal wing for case 8 had an induced drag reduction of 9.35%.

Simulations were carried out for both control and optimal wings in the presence of the propeller, and the induced drag was computed by integrating the surface pressure.

Figs. 5.12 and 5.13 show the density residue, defined as logarithm of the L_2 norm of density normalised with the L_2 norm of density in the 1^{st} iteration, with number of iterations for mesh sizes of 10×10^6 and 30×10^6.

For a simulation carried out with 5×10^6 mesh volumes for both control and optimal wing-propeller system, span efficiency η defined as

$$\eta = \frac{C_L^2}{\pi \, \mathcal{AR} \, C_{Di}}, \tag{5.15}$$

predicted by PROP-EULER code was 0.558 and 0.608 respectively. The span efficiency

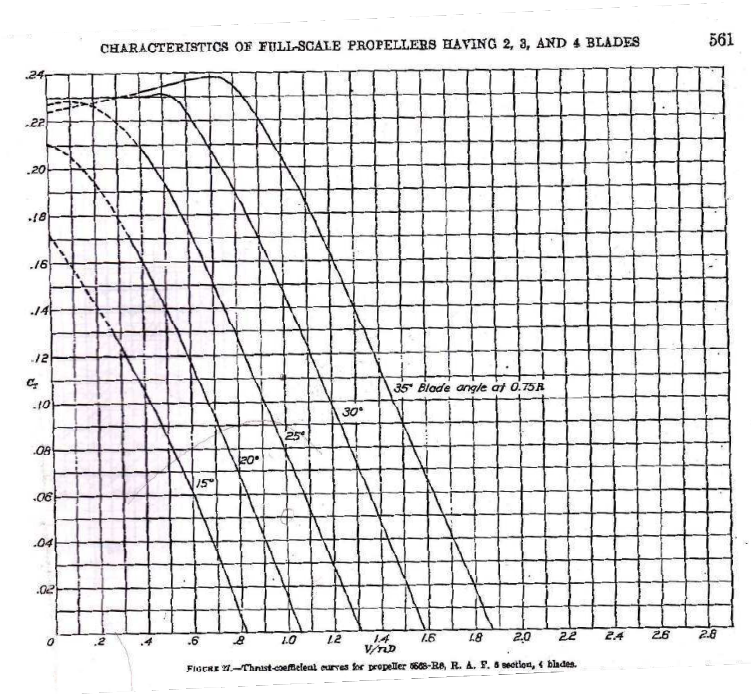

Figure 5.10: Plot of thrust coefficient versus advance ratio for different blade settings, taken from Hartman & Biermann (1938)

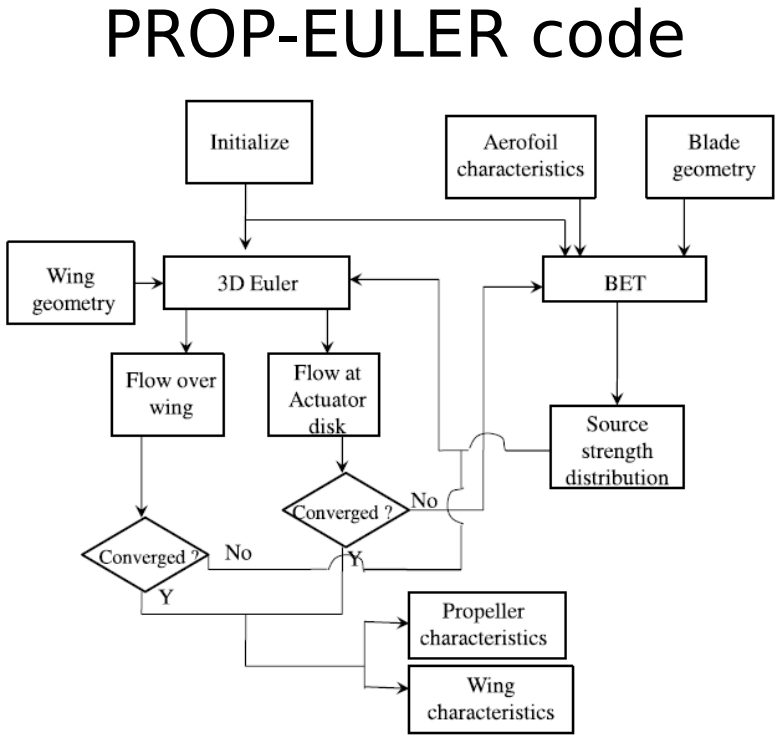

Figure 5.11: Block diagram of PROP-EULER code

of the optimal wing-propeller system was higher by 8.92% compared to the control wing-propeller system.

To ensure grid independence of results, simulations with 10×10^6 and 30×10^6 mesh volumes were carried out.

With 10×10^6 mesh volumes for both control and optimal wing-propeller system, span efficiency predicted by PROP-EULER code was 0.5856 and 0.6334 respectively. The span efficiency of the optimal wing-propeller system was higher by 8.16% compared to the control wing-propeller system.

For the mesh size of 30×10^6 mesh volumes for both control and optimal wing-propeller system, span efficiency predicted by PROP-EULER code for control wing-propeller system was 0.637 and for optimal wing-propeller system was 0.687. The span efficiency of the optimal wing-propeller system was higher by 7.84%, close to the value for the 10×10^6 mesh results compared to control wing-propeller system. This establishes satisfactory grid independence of results.

Figs. 5.14 and 5.15 show the convergence behaviour of lift coefficient for mesh sizes of 10×10^6 and 30×10^6 respectively.

Figs. 5.16 and 5.17 show the convergence behaviour of induced drag coefficient for mesh sizes of 10×10^6 and 30×10^6 respectively.

From the results mentioned above it can be seen that the reductions in induced drag predicted by high fidelity CFD simulations using PROP-EULER code are very close to the value predicted by the low fidelity PROWING tool, which is 9.35%.

Contour plot of the pressure coefficient on both optimal and control wings for the mesh size of 30×10^6 mesh volumes are shown in figures 5.18 and 5.19. It is seen that the pressure gradients are smoother on the optimal wing (fig. 5.19) compared to those on the control wing (fig. 5.18), especially in the region covered by the propeller slipstream.

5.4 Use of Fluent along with UDF for validation of optimal wing design

UDF is a function that enables user programs to be loaded to Fluent to enhance certain capabilities. For example, one may impose a certain type of boundary condtion by writing a small program. One can also define sources in an elemental mesh volume. UDFs are written in C programming language. There are many predefined macros in Fluent which can be used to build UDFs.

We have used a particular macro called as DEFINE_SOURCE (FLUENT 2003). This particular macro helps in adding a mass, momentum and energy source to elemental mesh volumes. The strength of the sources can have a variation over the actuator disk depending on the user's requirement. In the present study, there is no mass source and the blade

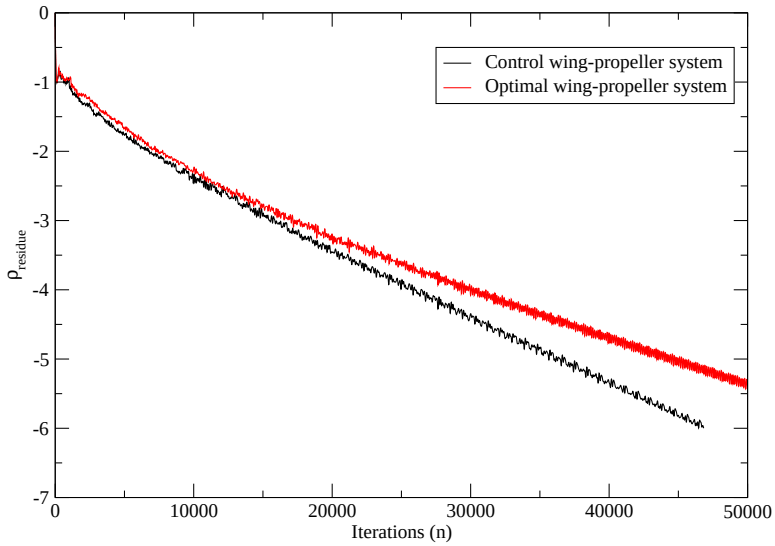

Figure 5.12: Density residue variation with number of iterations for control and optimal wing-propeller system for mesh size of 10×10^6

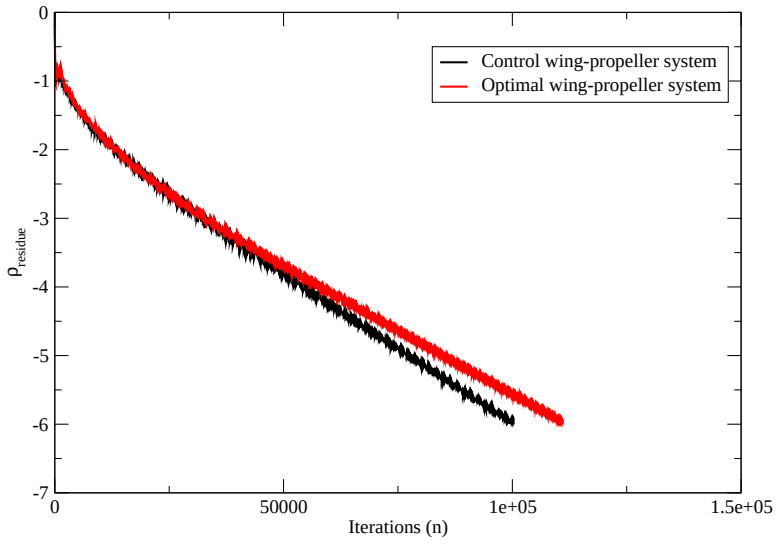

Figure 5.13: Density residue variation with number of iterations for control and optimal wing-propeller system for mesh size of 30×10^6

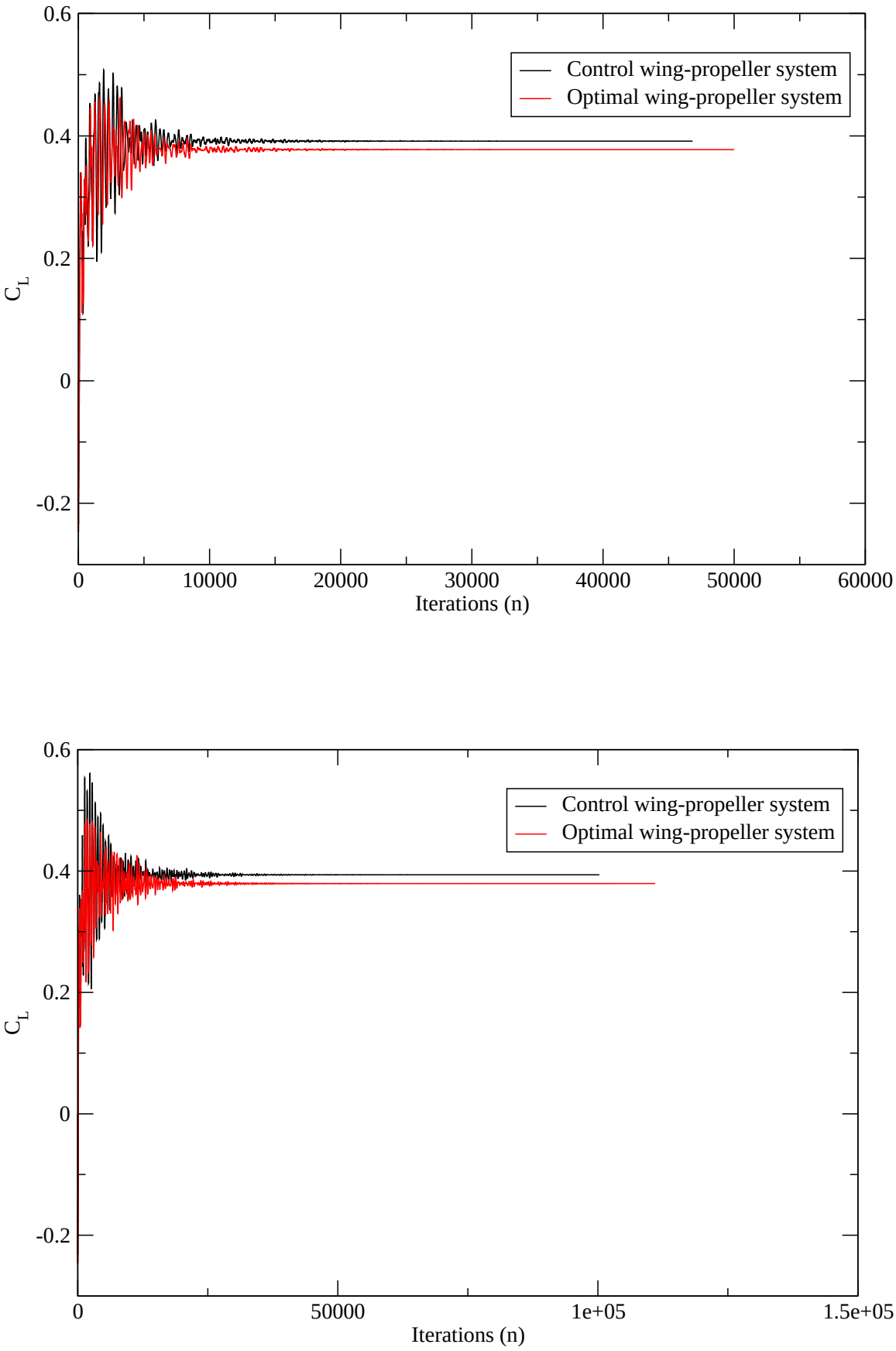

Figure 5.15: Convergence of lift coefficient for control and optimal wing-propeller system for a mesh size of 30×10^6

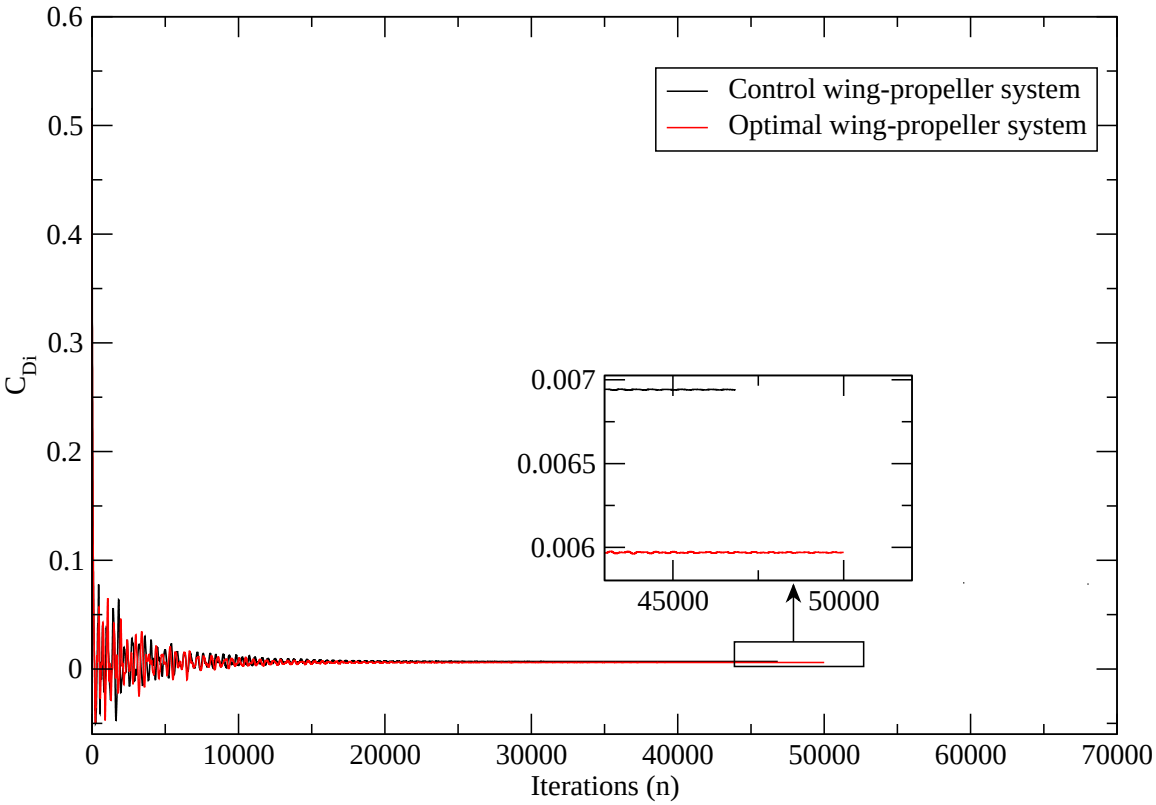

Figure 5.16: Convergence of induced drag coefficient for control and optimal wing-propeller system for a mesh size of 10×10^6. Inset shows the zoomed view of the tail of the convergence history.

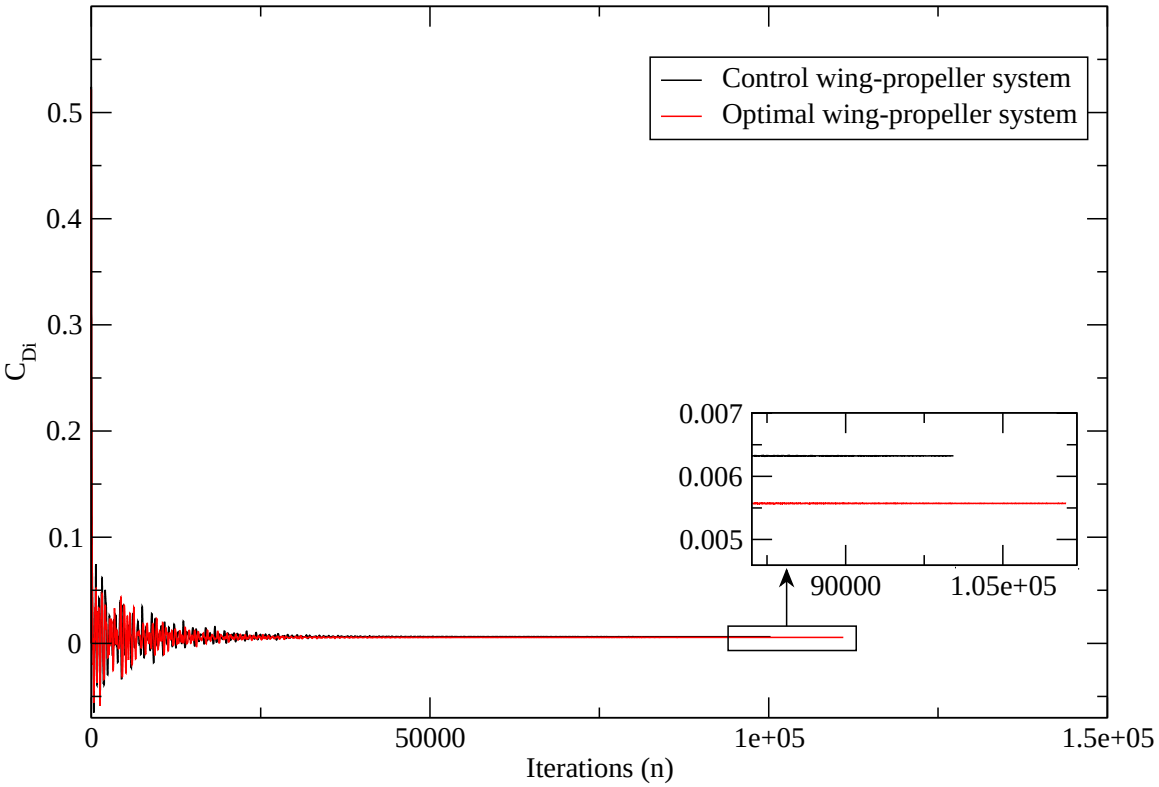

Figure 5.17: Convergence of induced drag coefficient for control and optimal wing-propeller system for a mesh size of 30×10^6. Inset shows the zoomed view of the tail of the convergence history.

element module developed here is used to estimate the strength of the momentum and energy sources.

The optimal wing for case 9 described in chapter 3, which has a total drag lesser by 9.35 drag counts, was chosen to validate the theory and optimization in PROWING. To eliminate the uncertainities in predicting absolute drag values with RANS codes, we focus on the reduction in drag indicated in counts and not in percentages.

For solving the RANS equations, the Spalart-Allmaras turbulence model was used. A mesh size of 10^7 mesh volumes was used. The final solution had the first mesh point at $y^+ < 1$ where y^+ is defined as

$$y^+ = \frac{u_* y}{\nu} \tag{5.16}$$

where u_* is the friction velocity at the nearest wall, y is the distance to the nearest wall and ν the kinematic viscosity of the fluid.

From the simulation it was found that the total drag coefficient of the optimal wing was lower by 10.04 counts compared to the control wing. This reduction is very close to the value of 9.35 counts predicted by PROWING.

These results show that the assumptions made in the model underlying PROWING provide a good approximation for wing-propeller systems. Due to lack of computational

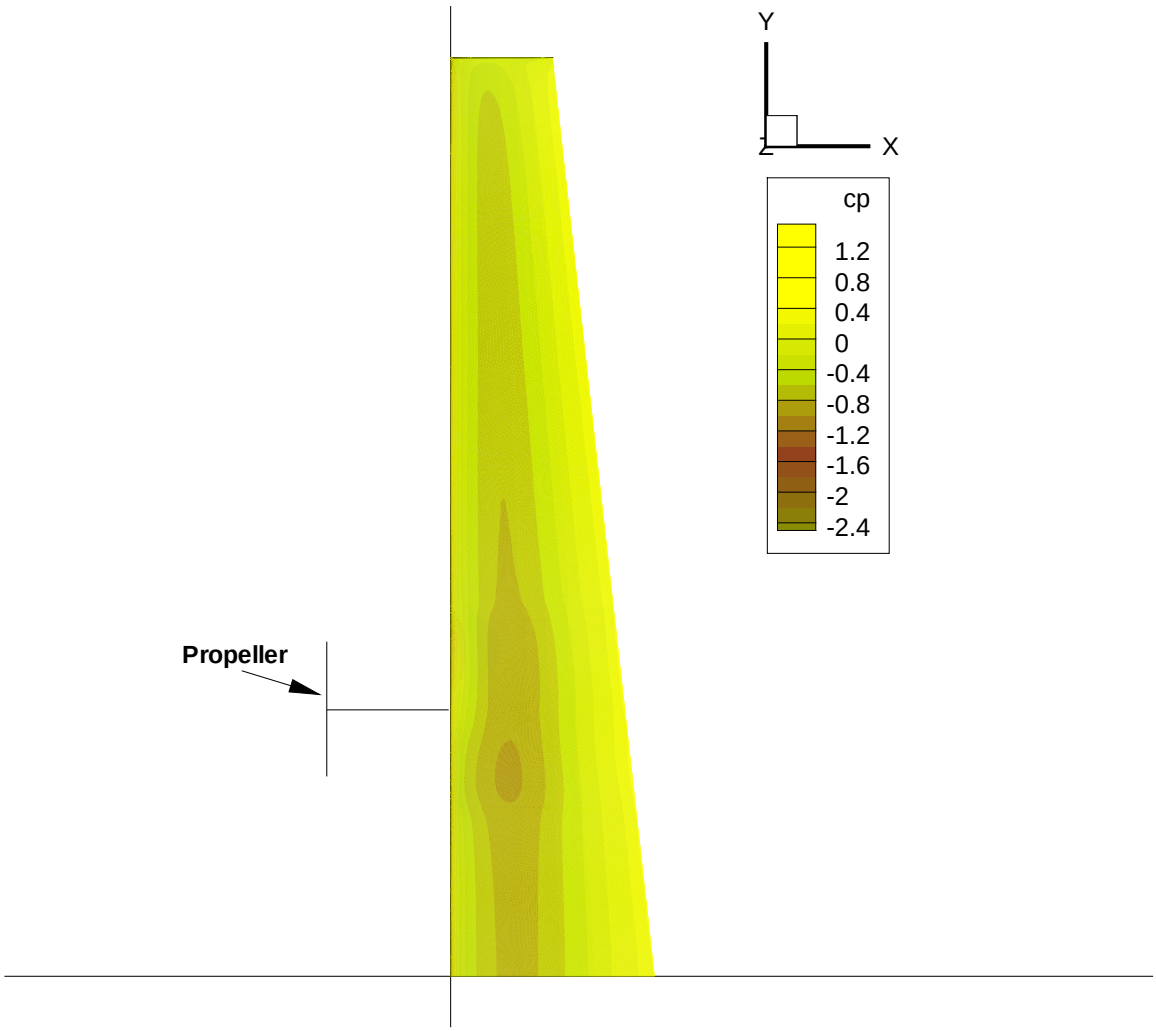

Figure 5.18: Surface contours of pressure coeffecient on control wing.

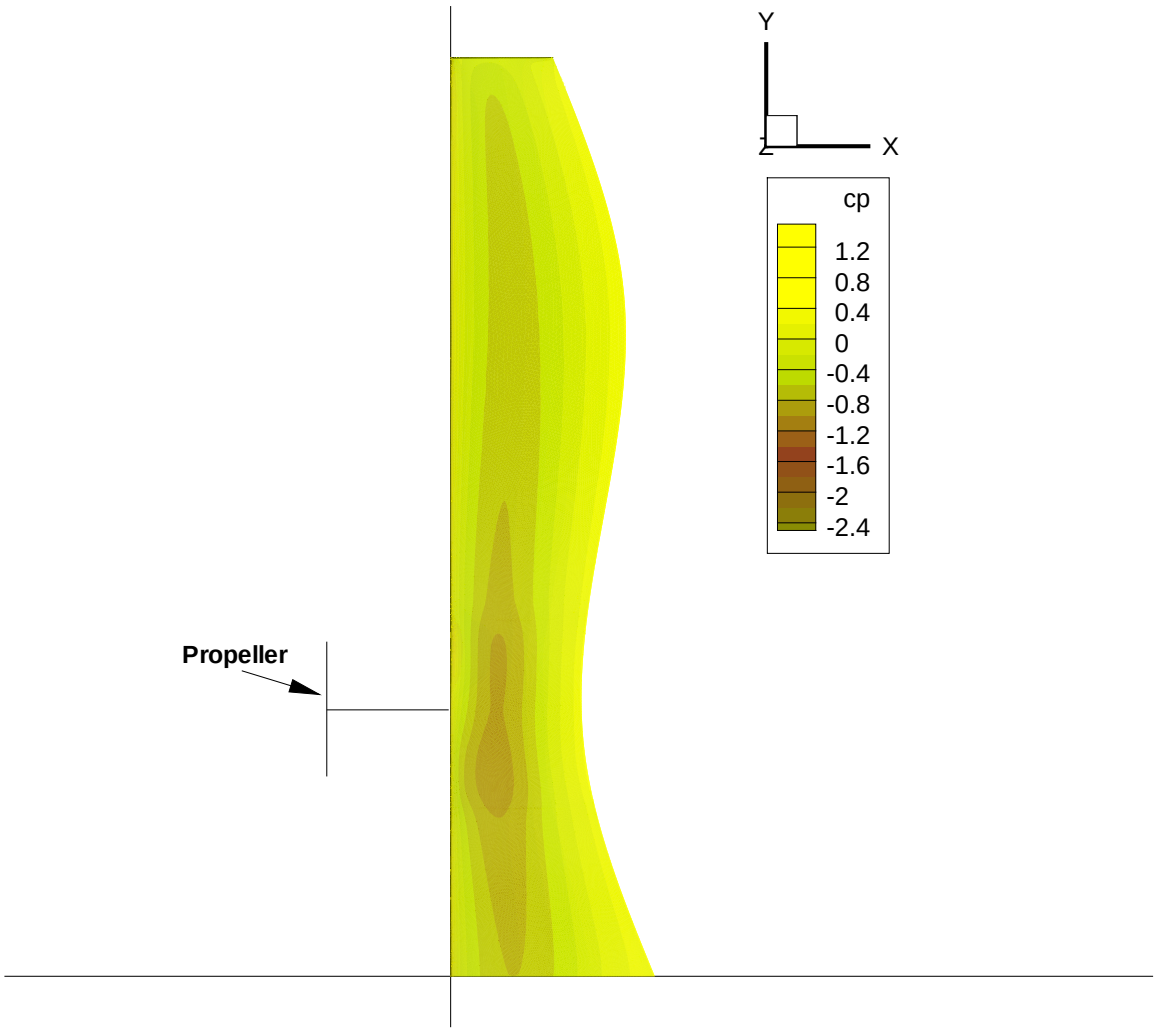

Figure 5.19: Surface contours of pressure coeffecient on optimal wing.

resources, finer meshes could not be used but wind tunnel tests were carried out, and these are described in chapter 6.

5.5 Conclusion

High fidelity CFD simulations, on both control and optimal wings, have shown that the optimal wing has indeed lower drag compared to the control wing. Use of the present PROP-EULER code confirms that the reduction in induced drag as predicted by PROWING is a good estimate, and use of RANS code (FLUENT) along with User Defined Functions confirms the reduction in total drag. This shows that the theory and optimizer in PROWING offer a good approximation and representation of the wing-propeller system.

Chapter 6
Wind Tunnel Tests

In addition to CFD simulations described in chapter 5, a short proof-of-concept wind tunnel study was carried out in collaboration with C-CADD (Centre for Civil Aircraft Design and Development), NAL, Bangalore. A more complete test programme was not possible because of constraints on time and resources, but it is being currently planned. Details and results of the tests, taken in part from Panda *et al.* (2012), are described in subsequent sections. In addition to the details and results, an analysis carried out by us to (i) check for consistency in experiments and (ii) understand the results, is also presented.

6.1 Experimental setup

The wind tunnel studies were carried out on a $1/10^{\text{th}}$ scale model of the NAL Saras aircraft. Saras is a 14-19 seat turboprop with propellers mounted in a pusher configuration (fig. 6.1), and was chosen because a wind tunnel model was readily available at C-CADD, NAL. Since Saras was by design a pusher, and as our study was on a tractor configuration, the model was converted into a tractor by using additional mounts. Saras in tractor configuration, to be called as Saras-C, was used as the control model. The experiments were carried out at the IISc 9ft $\times$ 14ft open circuit wind tunnel.

A $1/10^{\text{th}}$ scale Hartzell propeller was used for the study. Slipstream velocities required for the design of optimal wings using PROWING were generated using the PROP-EULER code. For this purpose the aerodynamic coefficients of the Hartzell propeller blade sections were needed and were computed using XFOIL (Drela & Giles 1987) for a chord based Reynolds and Mach number, corresponding to a wind speed of 35m/s. Variation of chord and pitch of the Hartzell propeller blade along the radius is shown in fig. 6.2. Variation of Reynolds and Mach numbers along the radius of the propeller is shown in figs. 6.3 and 6.4. Aerodynamic coefficients computed using XFOIL for sections of the propeller blade were then given as the input to the PROP-EULER code to generate slipstream velocities. Using these slipstream velocities, wing optimization was carried out using PROWING. The optimal wing had the same aerofoil section as the Saras wing namely modified GAW-2. Four optimal wing designs were generated as reported under case 10 in chapter 4, all at $C_L = 0.4$, the cruise lift coefficient of Saras.

The four candidate designs 10a, 10b, 10c, 10d are optimal planforms generated using different number of design variables mentioned under each planform under case 10 in

Figure 6.1: Saras aircraft with propellers mounted in pusher configuration

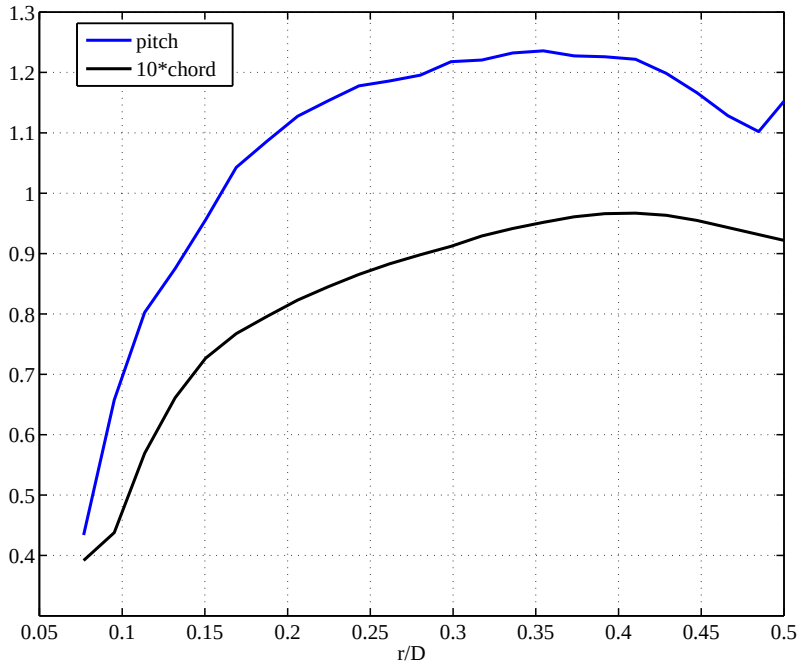

Figure 6.2: Variation of chord and pitch along the radius of $1/10^{\text{th}}$ scale of hartzell propeller blade

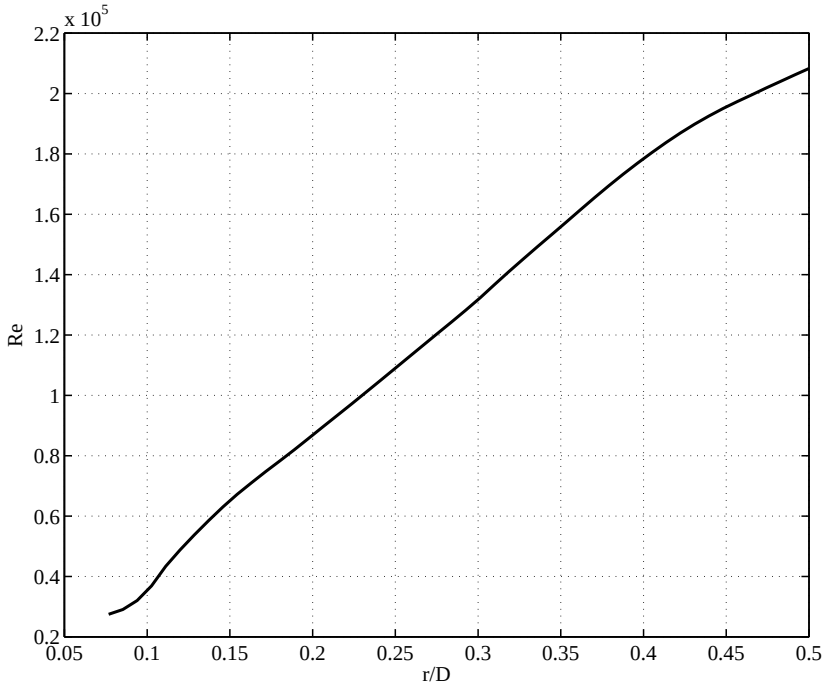

Figure 6.3: Variation of Reynolds number along the radius of $1/10^{\text{th}}$ scale of hartzell propeller blade

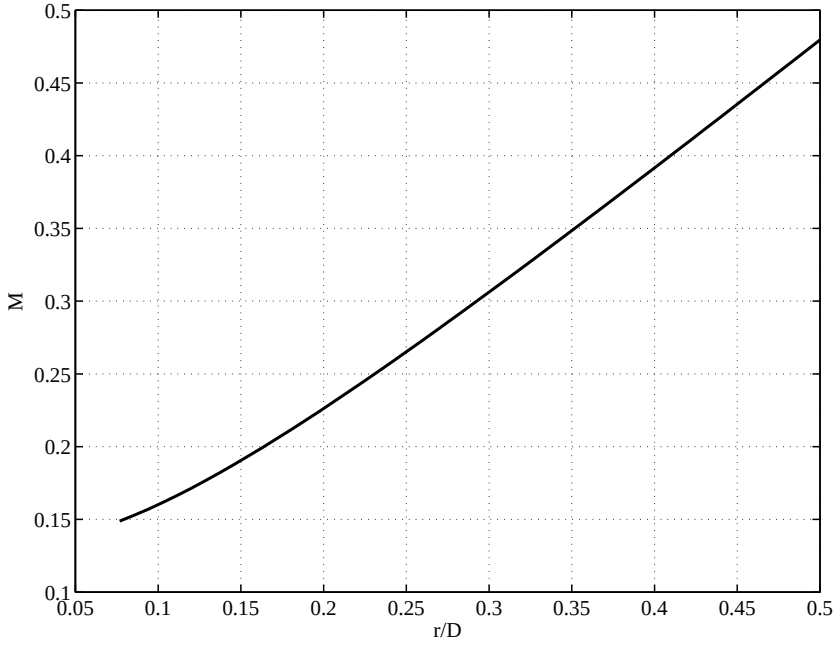

Figure 6.4: Variation of Mach number along the radius of $1/10^{\text{th}}$ scale of hartzell propeller blade

Figure 6.5: Control configuration - Saras-c used for wind tunnel testing

chapter 4. Out of the four candidates design 10a was chosen for the wind tunnel experiments, as it had the highest total drag reduction compared to the other designs namely, 6.61%.

A CAD model of design 10a was prepared and handed over for fabrication at NAL. The optimal wing model as fabricated at C-CAD, NAL used fiber reinforced plastic, with two aluminium spars of 9mm diameter located at 17mm and 35mm from the leading edge of the wing and 2mm above the wing root aerofoil chord line. The model with the optimal wing attached to the fuselage of Saras-C is called Saras-O.Final models of Saras-C and Saras-O used for wind tunnel testing are shown in figures 6.5 and 6.6 respectively.

Figure 6.6: Optimal configuration - Saras-o used for wind tunnel testing

6.2 Test Procedure

The tests were conducted at a tunnel wind speed of 35m/s. To have a significant effect of the propeller slipstream on the wings and measurable drag differentials, the propellers were run at an advance ratio of 0.89. The rotational sense of the propellers was up-inboard. Tests were conducted with and without boundary layer trips, herein referred to as BLT. Forces in all the three directions were measured and drag polars and pitching moment were computed. The range of angles of attack covered was from $-4°$ to $+10°$.

Table 6.1 gives the geometric and aerodynamic details of propeller and wing used to generate optimal wing design for wind tunnel testing.

Parameter	Value
Wing span	1.3m
Exposed wing area	$0.214m^2$
Aspect ratio	7.89
Taper ratio	0.3481
Cruise lift coefficient	0.4
Propeller diameter	0.216m
Propeller blade angle at 75% radius	29°
Tunnel speed	35m/s
Advance ratio	0.89

Table 6.1: Geometric and aerodynamic details used to generate optimal wing design

Saras-C and Saras-O mounted in the wind tunnel for testing are shown in figs. 6.7 - 6.9. Figure 6.10 shows the propeller mounted in tractor configuration. Fig. 6.11 shows the trip used on the wing surface.

The tests were divided into the following runs:

- Basic run: This test was on a model configuration including fuselage (F), wing, vertical tail (VT), horizontal tail (HT) and ventral fins (VF). The model was mounted on a strut in the wind tunnel.

- Power off: This test includes all the components of basic run along with motor struts (MS) and nacelles (N) but without the propeller as it would windmill and hence alter the flow-field across the wing. This test is essential to find out the aerodynamic effects of the components added after the basic run.

- Power ON: This test includes all the components of basic run along with motor mounts, nacelles and propellers. The motors are supplied with the power to rotate the propellers at the predetermined speed to achieve the required advance ratio, thereby developing the required flow-field. The test was conducted with and without boundary layer trips (BLT). Two types of BLTs, namely BLT 1 which has dense

Figure 6.7: Saras wing, as seen from front and below, mounted to the fuselage

Figure 6.8: Optimal wing, as seen from front and below, mounted to the fuselage

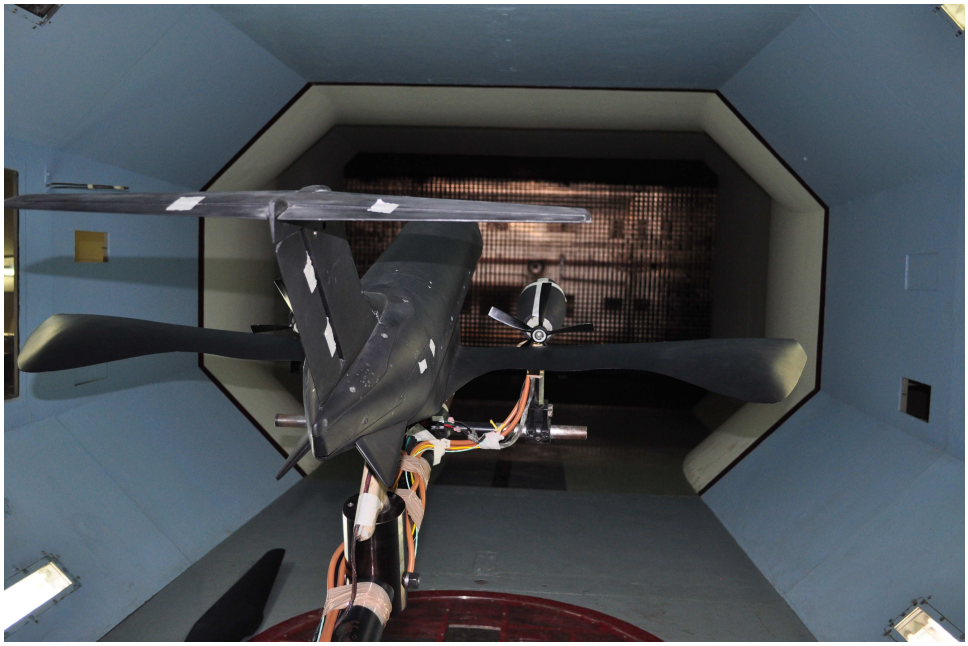

Figure 6.9: Optimal wing, as seen from behind the aircraft

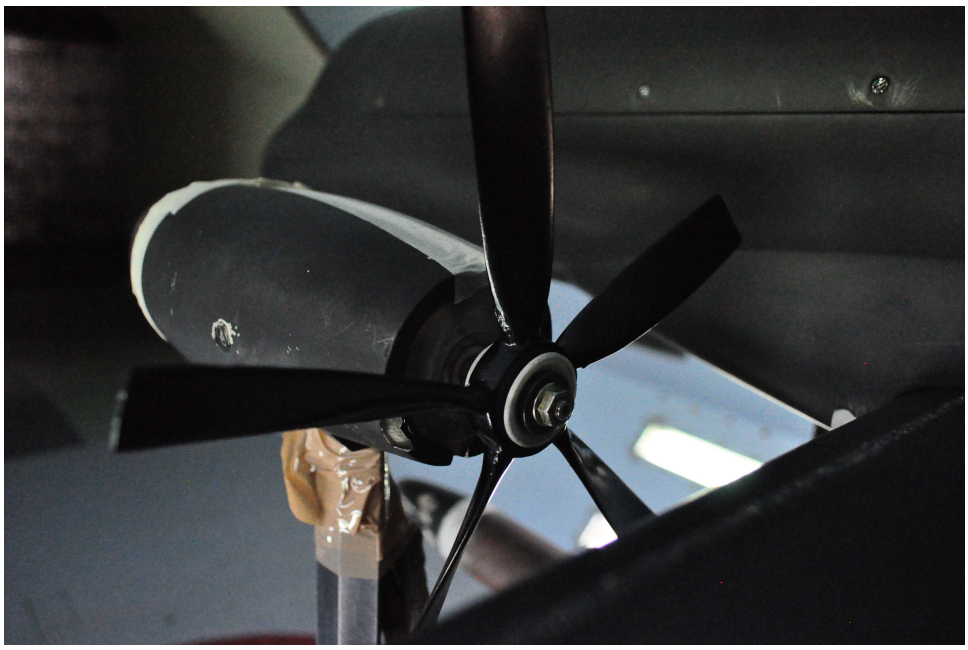

Figure 6.10: $1/10^{\text{th}}$ scale model of Hartzell propeller

Figure 6.11: Boundary layer trip used for testing

particles, and BLT 2 which has fine particles, were used. After preliminary tests with BLT 1, it was decided that the tests with BLT would be performed with BLT 2 as the particle size in BLT 1 was too thick.

Table 6.2 indicates the test schedule.

Run No.	Components involved
1	F + Saras-C + VT + HT + VF Basic Run
2	F + Saras-O + VT + HT + VF Basic Run
3	F + Saras-C + VT + HT + VF + MS + N + BLT2 + Power OFF
4	F + Saras-O + VT + HT + VF + MS + N + BLT2 + Power OFF
5	F + Saras-C + VT + HT + VF + MS + N + BLT 2 + Power ON
6	F + Saras-O + VT + HT + VF + MS + N + BLT 2 + Power ON
7	F + Saras-C + VT + HT + VF + MS + N + Power ON (no trip)
8	F + Saras-O + VT + HT + VF + MS + N + Power ON (no trip)

Table 6.2: Test schedule

6.3 Results

Results of wind tunnel tests for the schedule mentioned in table 6.2 are described in this section.

Figures 6.12, 6.13 show a comparison of drag polar and $C_M - C_L$ variation between runs 1 and 2. From fig. 6.12 it can be seen that the Saras-O configuration even without the propeller has a lower drag, by 8.33% at $C_L = 0.4$. It also has a lower drag upto about $C_L =$

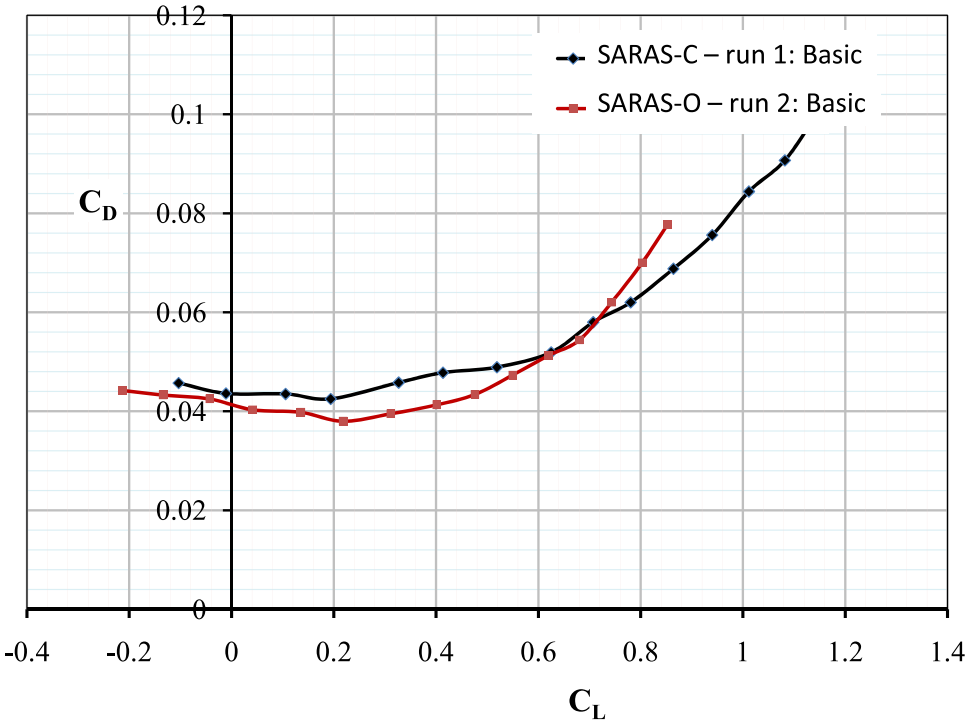

Figure 6.12: Comparison of drag polar between runs 1 and 2

0.6. Thus, even in the absence of the slipstream, the new planform is aerodynamically more efficient. From fig. 6.13 it can be seen that the stability characteristics of both Saras-C and Saras-O configurations are almost the same till about a $C_L = 0.45$, and that for $C_L > 0.45$ Saras-O is stabler than Saras-C.

Figures 6.14, 6.15 show a comparison of drag polar and $C_M - C_L$ variation between runs 3 and 4. Similar observations as made for runs 1 and 2 can be made. From fig. 6.14 it can be seen that Saras-O wing even without the propeller has a lower drag upto about $C_L = 0.55$. The boundary layer trip has moved the cross over point in the drag polar to a lower C_L value compared to the drag polar of runs 1 and 2. From fig. 6.15 it can be seen that Saras-O is stabler compared to the Saras-C in the presence of a boundary layer trip.

Figures 6.16, 6.17 show a comparison of drag polar and $C_M - C_L$ variation between runs 5 and 6 (power on). It can be seen from figure 6.16 that the drag of Saras-O at $C_L = 0.4$ is lower by about 15% compared to Saras-C. C_D continues to be lower upto $C_L \approx 0.78$, increasing thereafter. One point that needs to be emphasised is that the optimal wing was designed for cruise at $C_L = 0.4$. The drag of Saras-O being lower than Saras-C at other C_L's is a by-product. It was found that the C_L for Saras-C during take-off is around 0.76-0.78. Therefore, it can be concluded that Saras-O is doing neither any better nor any worse during take-off. Depending on the duration of the cruise phase during flight, the benefits of lower drag are available.

The precise reason for the higher drag reduction obtained in wind tunnel tests is not clear at the present stage, however the following explanations are plausible: (i) accuracy of propeller data supplied as input to Prop-Euler code which was used to generate slipstream

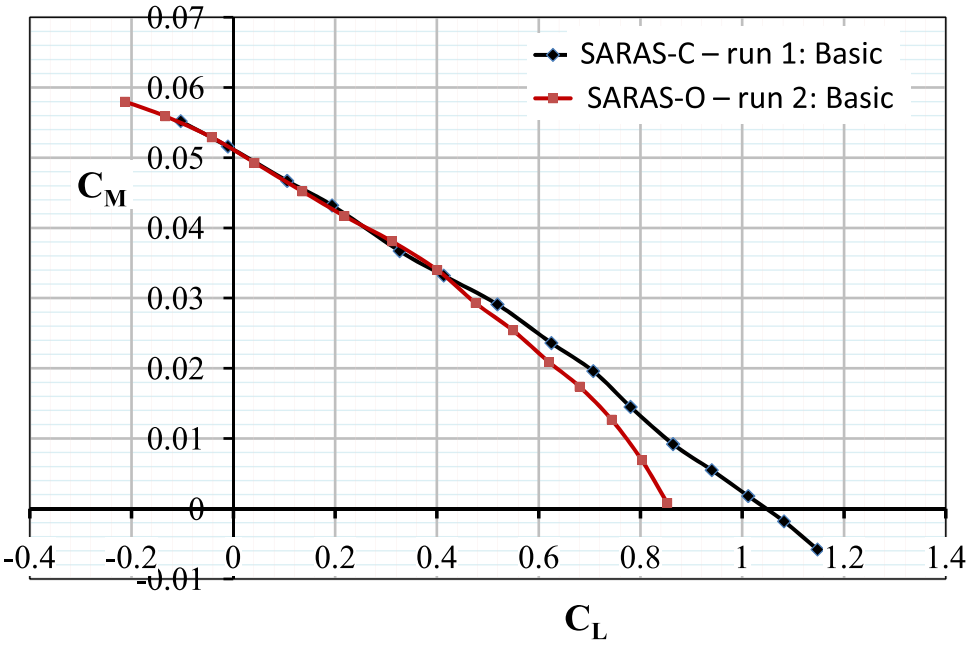

Figure 6.13: Comparison of pitching moment variation with C_L curves between runs 1 and 2

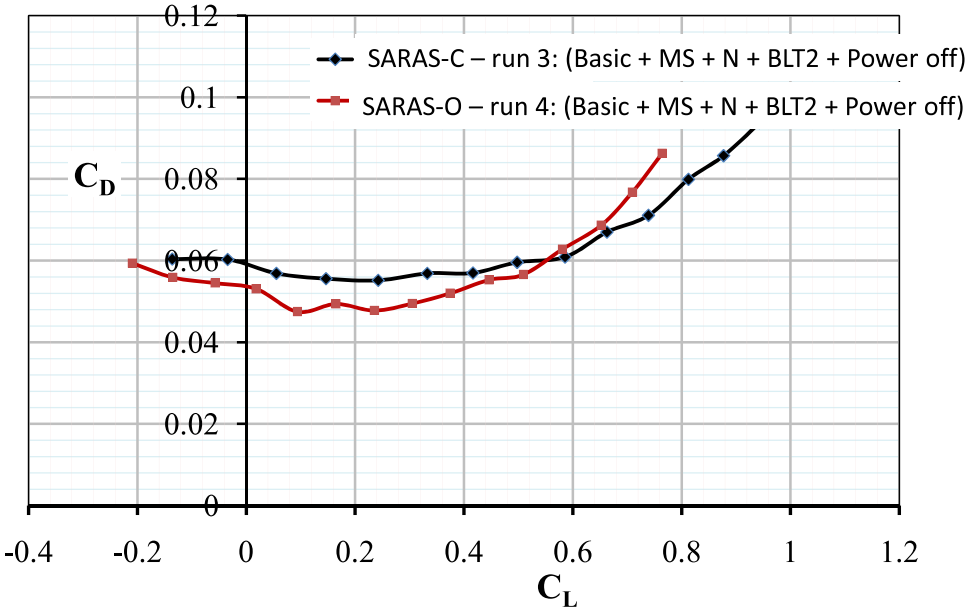

Figure 6.14: Comparison of drag polar between runs 3 and 4

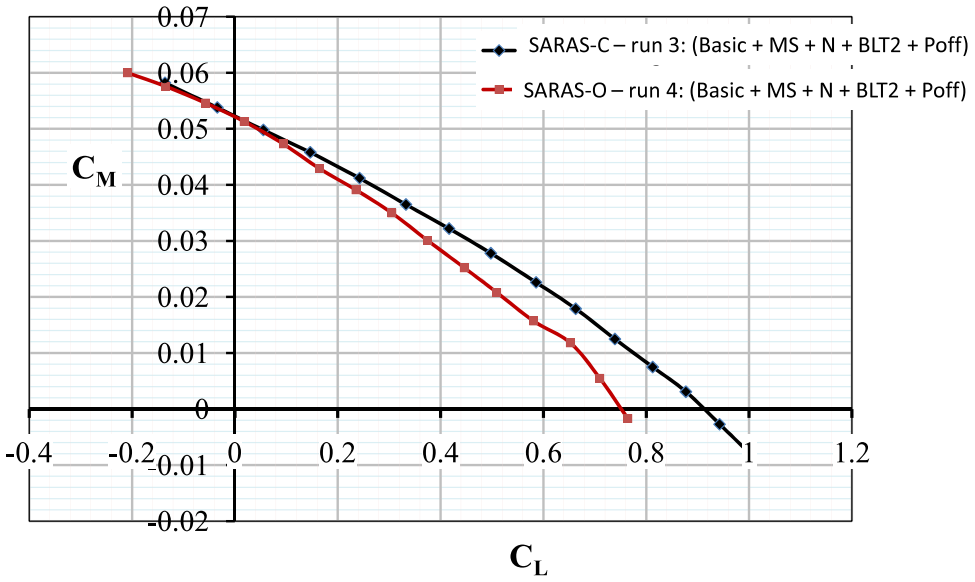

Figure 6.15: Comparison of pitching moment variation with C_L curves between runs 3 and 4

velocities, (ii) local Reynolds number based on larger wing chords are higher in outboard regions of the wing because of large chords and could lead to lower skin friction drag, (iii) lower parasite drag of optimal wing as evidenced by fig. 6.12 even at $C_L = 0$ on the basic configuration, possibly related to trasitional flow at low tunnel Reynolds numbers and (iv) constructive interference between fuselage and wing. Investigations to explain higher C_D reductions than predicted for the wing alone are currently in progress.

But one fact that gets established in the light of this study is that the theory and optimization process embedded in PROWING is technically robust.

From 6.17 it can be seen that the longitudinal stability behaviour of both Saras-O and Saras-C are not very different.

Figures 6.18, 6.20 show a comparison of drag polar and $C_M - C_L$ variation between runs 7 and 8 (power on, no BLT). It can be seen from figure 6.18 that the drag of Saras-O at $C_L = 0.4$ is lower by about 20% compared to the Saras-C; it remains lower upto $C_L \approx 0.68$, and becomes higher thereafter. From fig. 6.20 it can be seen that the longitudinal stability behaviour of both Saras-O and Saras-C are the same till about $C_L = 0.6$.

Another way of data analysis that helps to check for consistency and seek better understanding of the results is now presented. We consider the drag coefficient C_D at $C_L = 0.4$ and the contribution of a boundary layer trip to the drag.

Fig. 6.21 first displays values of C_D at $C_L = 0.4$ for two Saras configurations: one

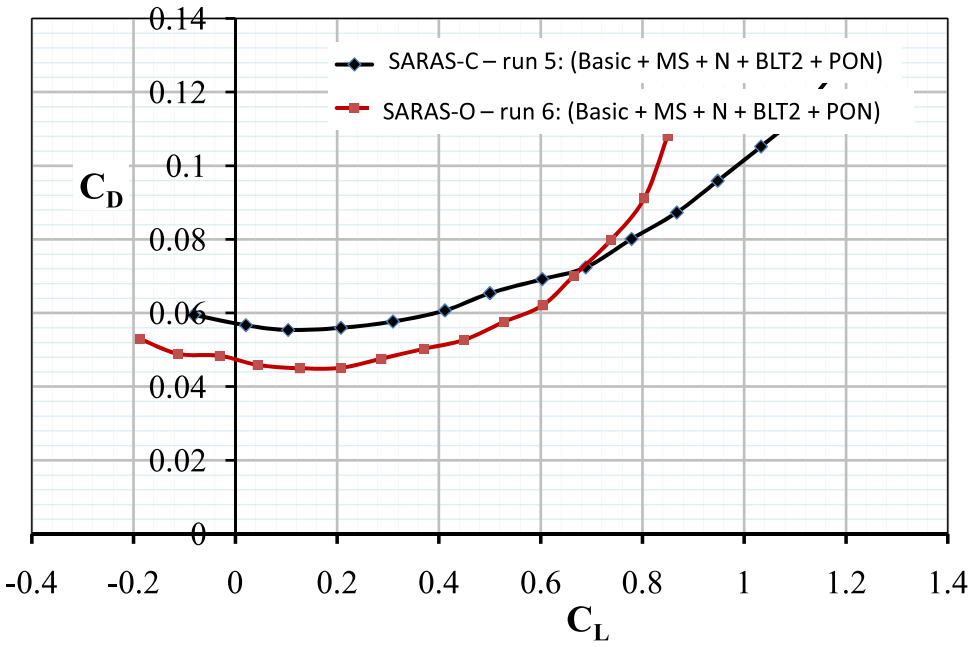

Figure 6.16: Comparison of drag polar between runs 5 and 6

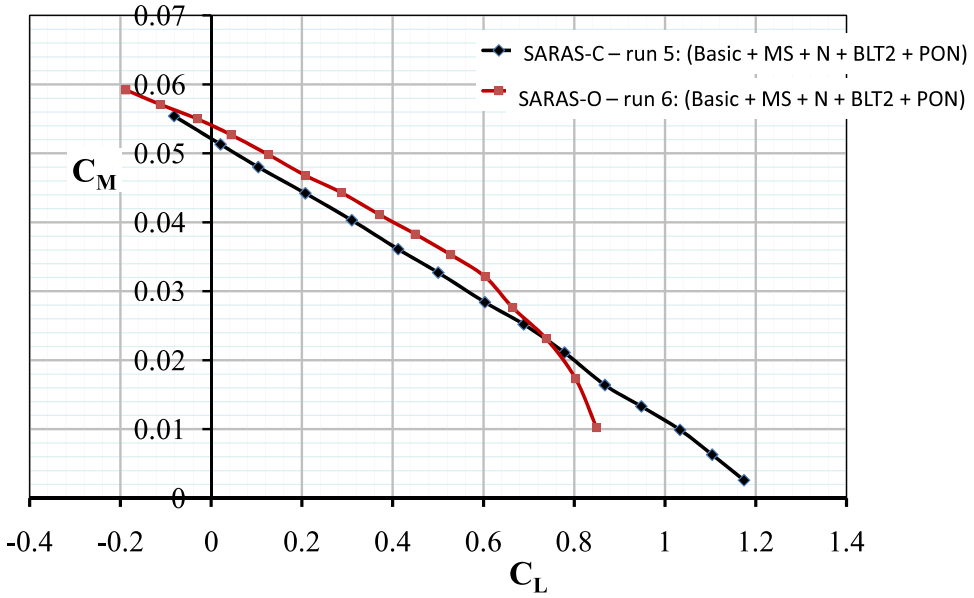

Figure 6.17: Comparison of pitching moment variation with C_L curves between runs 5 and 6

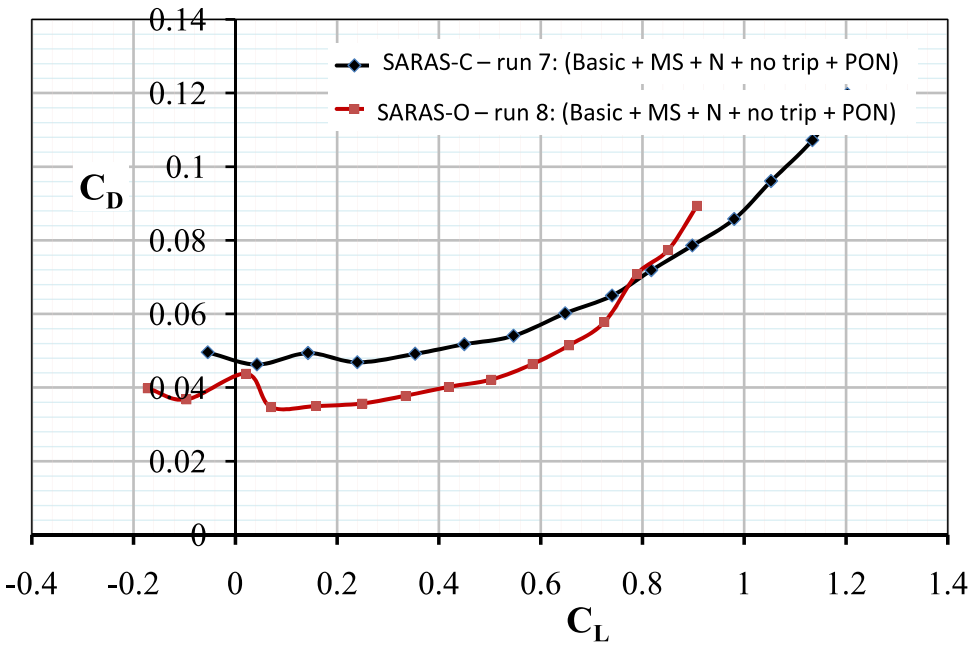

Figure 6.18: Comparison of drag polar between runs 7 and 8

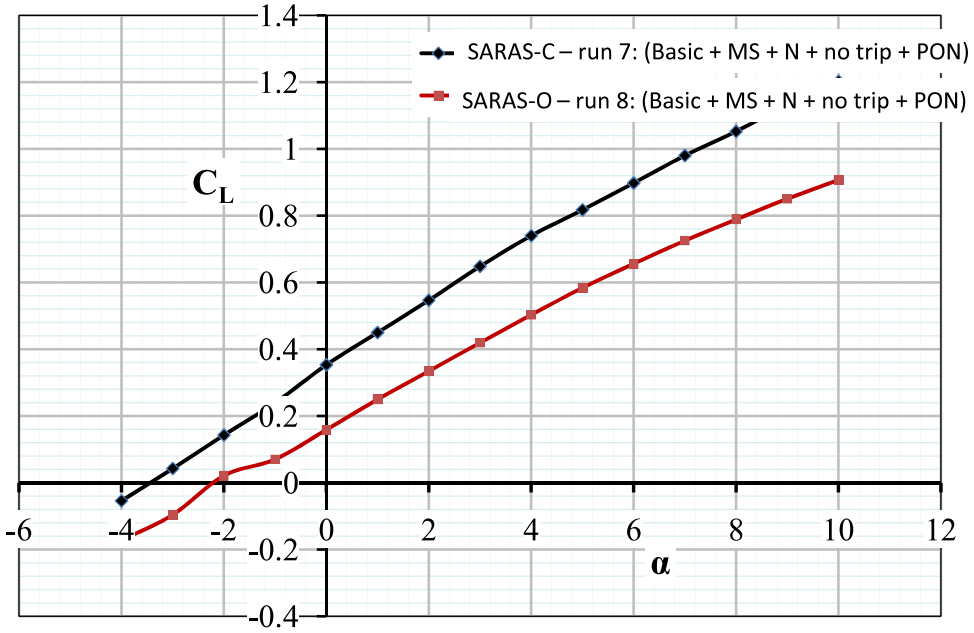

Figure 6.19: Comparison of cl-alpha curves between runs 7 and 8

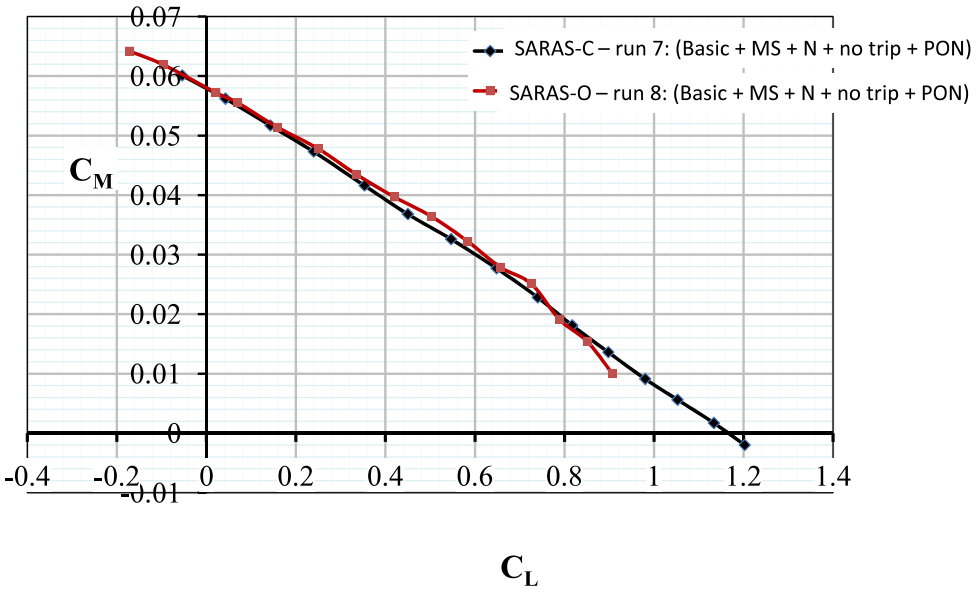

Figure 6.20: Comparison of pitching moment variation with C_L curves between runs 7 and 8

optimized wing (Saras-O) and the other with Saras wing (Saras-C). The figures for values of C_D are taken from the graphs already presented (figs. 6.12, 6.14, 6.16 and 6.18). There are four columns in fig. 6.21, respectively for four test conditions: (i) Basic (ii) no boundary layer trip, power on, (iii) boundary layer trip, power on (iv) boundary layer trip, power off. Differences in entries in each column show the differences between the optimal and control configurations at each test condition, wehreas the differences in the rows indicate the effects of test conditions on drag.

Looking at column 1 (basic), C_D for Saras-O is lower than for Saras-C by 5 units (1unit $= 10^{-3}$), i.e. even without the slipstream the new wing is performing better. When power is turned on, still without a boundary layer trip (column 2), the value of C_D for the optimal wing goes down by 2 units whereas that for Saras-C goes up by 3 units. This suggests that the normal increase in drag that might be expected with power on is absent in the optimal wing. In column 3, with the boundary layer trip and power on, the drag of Saras-O goes up by 11 units and that for Saras-C by 9 units. This must be attributed to the effect of the trip: it is gratifying that the overall effect in either case is very nearly the same. In other words the trip increases the drag by about 10 units in either configuration. It also suggests that the flow is largely laminar without the trip as the test Reynolds number is only 5×10^5 based on mean chord. Reading downwards in column 3 we see that the Saras-O has a lower drag than Saras-C by 9 units. This differential is not too different from the value of 10 units without a trip. Thus it would appear that with or without a trip Saras-O saves about 9.5 units in C_D. It is seen that the figures are largely consistent among themselves.

It is now interesting to look at the zero lift drag (fig. 6.22). The analysis in this case

Table 1: C_D at C_L = 0.4

Test condition → / Configuration ↓	Basic, CLEAN-WING* Fig 6.12 (a)	P. ON, NO TRIP Fig 6.18 (b)	P. ON, TRIPPED Fig 6.16 (c)	P. OFF TRIPPED+ Fig 6.14 (d)
Control	0.047	0.050	0.060	0.056
	+3	+10	+4	
	– 5	– 10	– 9	– 3
New wing	0.042	0.040	0.051	0.053
	–2	+11	–2	

*No engine mount or propeller
+ BLT2

Figure 6.21: C_D values for $C_L = 0.4$

is vitiated by an outlier at nearly zero lift conditions (fig. 6.18). This appears to be an experimental error of some kind although the cause for it has not been found. In the analysis two values of C_D at $C_L = 0$ are used for Saras-O, namely 0.043 (the outlier) and 0.036 (value interpolated between test results on either side). This correspondingly leads to two values for differentials involving no-trip power-on C_D. It is remarkable however, looking at column 3, Saras-O once again has a lower drag than Saras-C, and the tripped power-on drag of Saras-O is lower than that of Saras-C by 11 units, very close once again to the values at $C_L = 0.4$. This incidentally suggests that the optimal wing has an appreciably lower drag, even at nearly zero lift conditions, and that the contributions to the large drag reductions noticed in the tests are due in part to reductions in parasite drag. It is possible that, at the low test Reynolds numbers, transition effects are significant. A plausible explanantion would be the following. At $C_L = 0.4$ the trip is effective, and flow is turbulent all along the chord. At $C_L = 0$, when the pressure gradients are milder, the boundary layer over the shorter chords (where the Reynolds number is only 2.5×10^5 the boundary layer is not fully turbulent, so drag is lower. To check this explanation, further experimental studies on the wing and aircraft are necessary.

6.4 Flow visualization

Flow visualization using tufts was carried out for the Saras-O configuration. Figures 6.23 to 6.35 show flow visualiztion pictures over angles of attack ranging from $-4°$ to $10°$. From

Table 2: C_D at $C_L = 0$

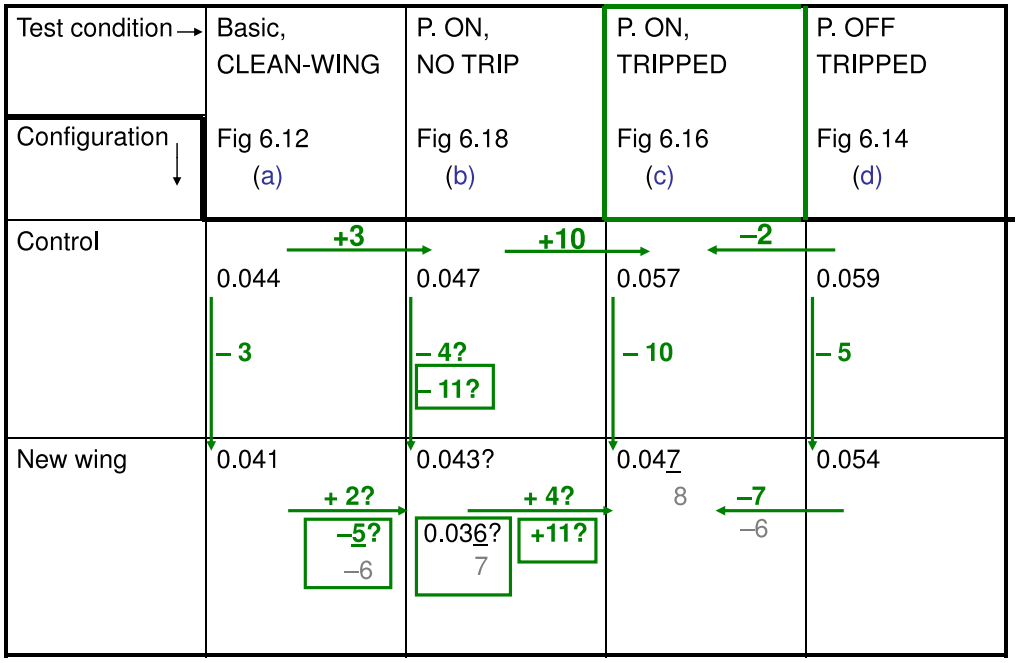

Figure 6.22: C_D values for $C_L = 0$. Boxed values correspond to the outlier point near $C_L = 0$ in fig. 6.18

figure 6.29 it can be seen that a mild separation has occured inboard of the propeller close to the wing root at an angle of attack of 8°. Comparing the drag polar between runs 7 and 8 shown in fig. 6.18 (runs 7 and 8 are chosen since, the boundary layer trip was removed in the flow visualization runs). The drag of Saras-O, compared to Saras-C, is higher beyond $C_L = 0.78$, which corresponds to an angle of attack of 8° from fig.6.19. This flow separation may be prevented by one of the following methods:

- recomputing an optimum wing design having a weighted cost function, one representing cruise and the other representing take-off/landing,
- by locally modifying the wing design by better wing body blending / selecting other aerofoil sections

Investigations along these directions are currently in progress.

6.5 Conclusion

Wind tunnel studies have shown that the optimal wing has substantially lower drag at the design C_L of 0.4. The drag is lower drag upto $C_L \approx 0.78$ for the case without boundary layer trip and upto $C_L \approx 0.6$ for the case with boundary layer trip. Flow visualization with tufts suggests that the cause for higher drag at higher C_L values ($C_L > 0.6$ and $C_L > 0.78$ with and without boundary layer trip respectively) may be separation. Studies to prevent flow separation are currently in progress but are beyond the scope of the present

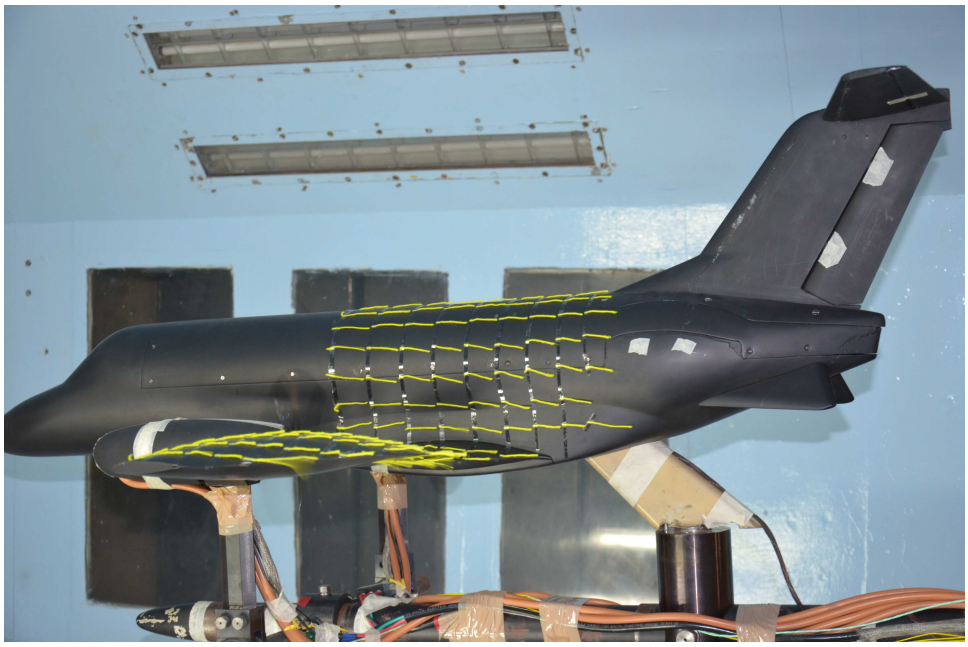

Figure 6.23: Flow visualization for SARAS-O at $-4°$

thesis. These results, along with CFD simulations, confirm that the theory and optimizer embedded in PROWING is technically robust and should be useful for preliminary design.

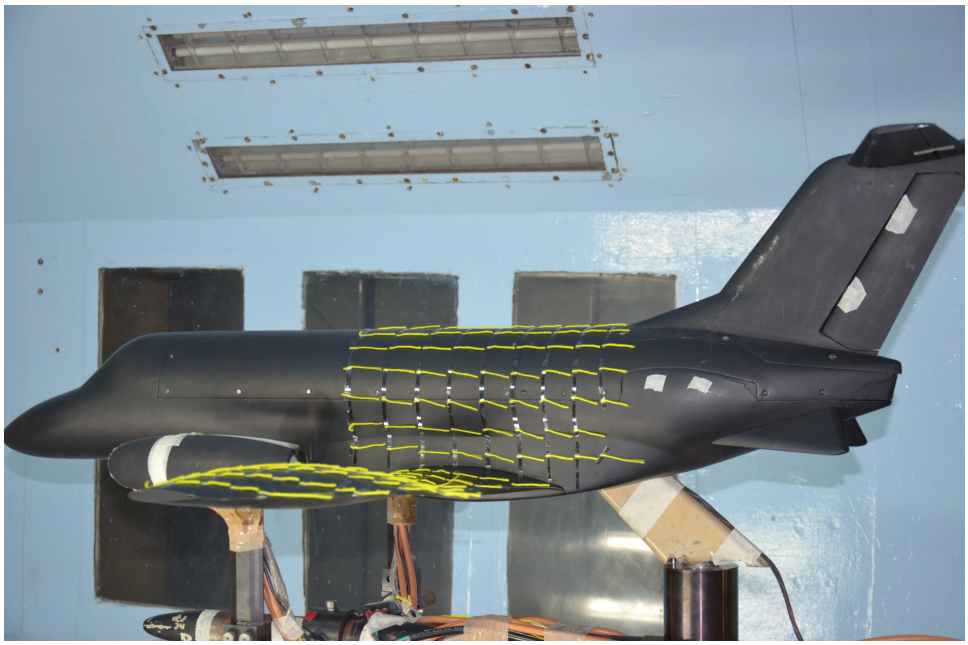

Figure 6.24: Flow visualization for SARAS-O at $-2°$

Figure 6.25: Flow visualization for SARAS-O at $0°$

Figure 6.26: Flow visualization for SARAS-O at 2°

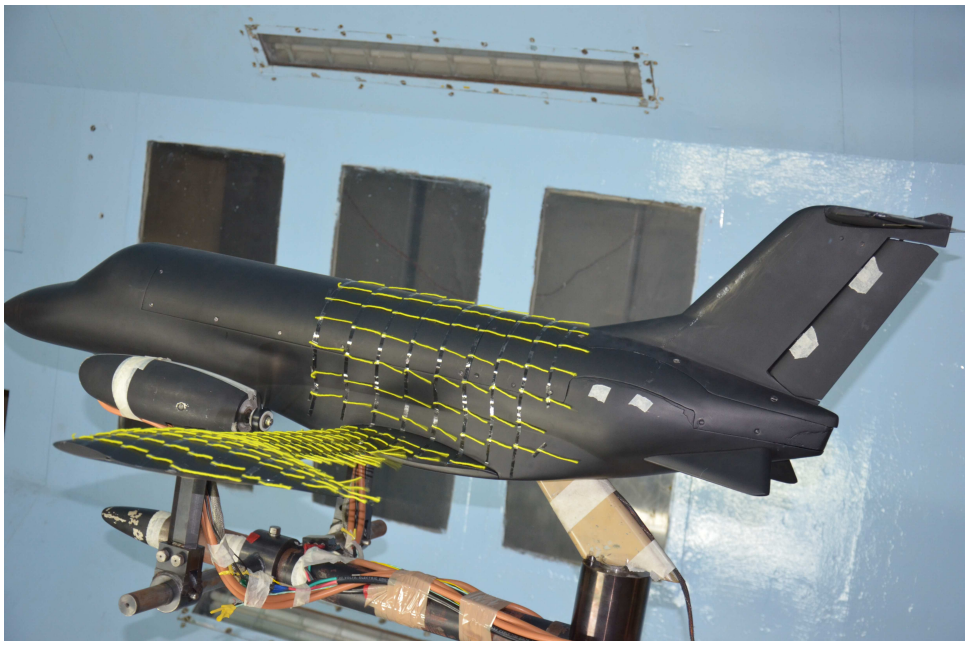

Figure 6.27: Flow visualization for SARAS-O at 4°

Figure 6.28: Flow visualization for SARAS-O at 6°

Figure 6.29: Flow visualization for SARAS-O at 8°

Figure 6.30: Flow visualization for SARAS-O at 10°

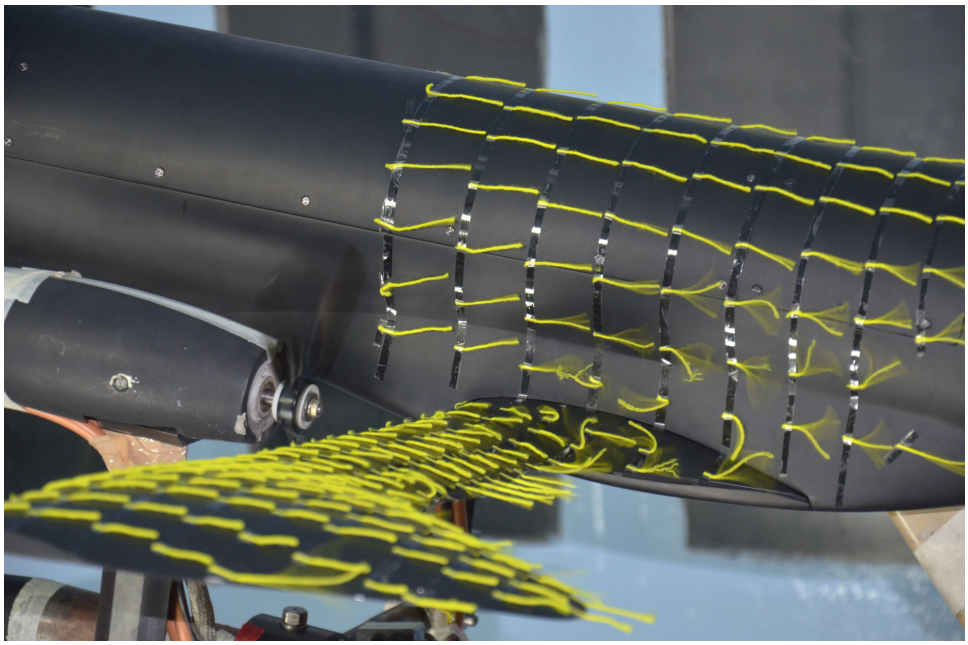

Figure 6.31: Flow visualization for SARAS-O at 10° (zoomed view)

Figure 6.32: Flow visualization for SARAS-O at 12°

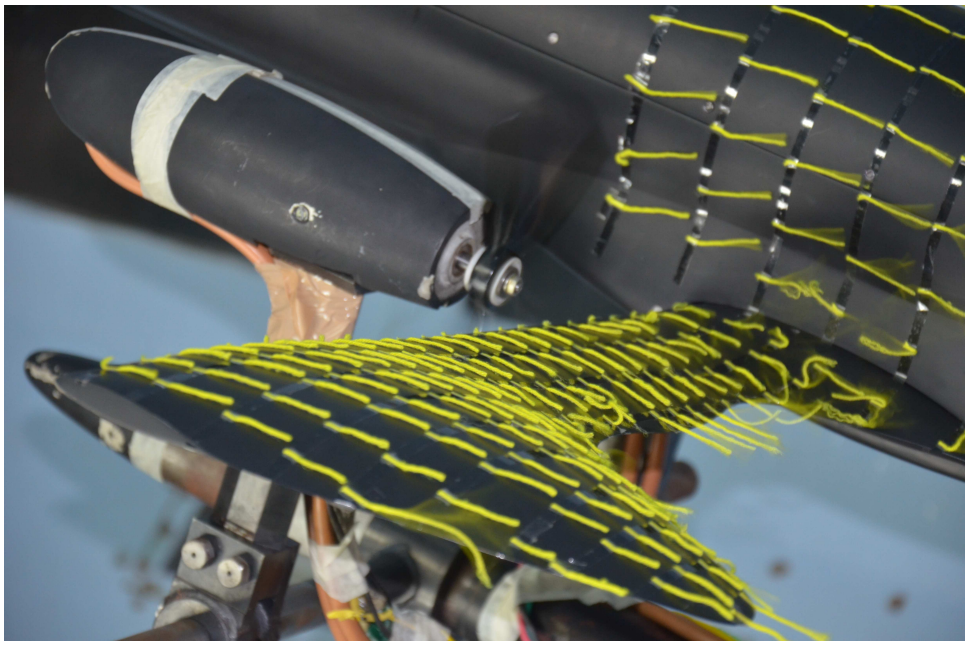

Figure 6.33: Flow visualization for SARAS-O at 12° (zoomed view)

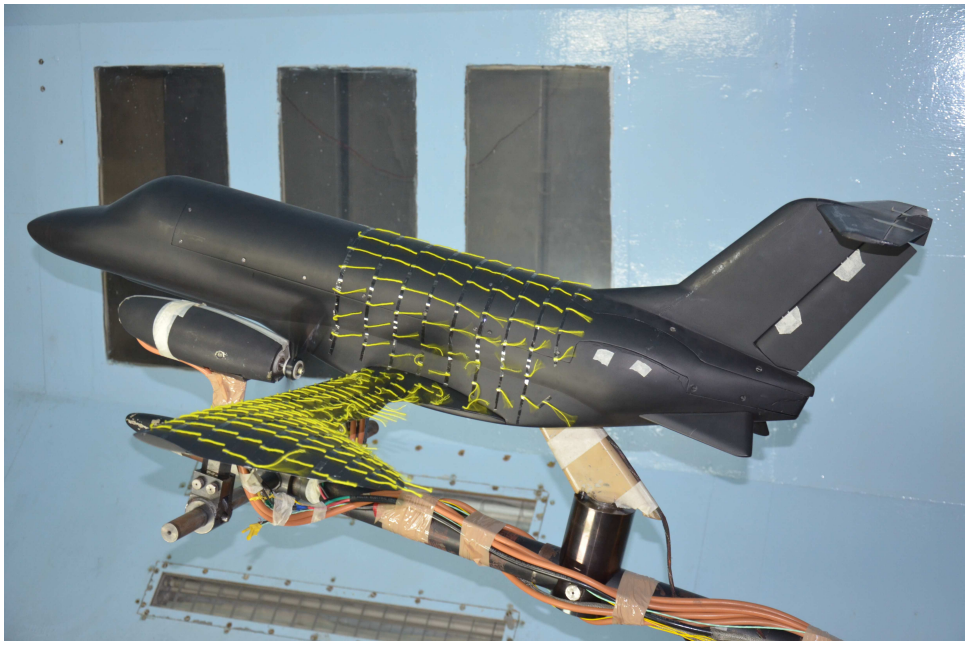

Figure 6.34: Flow visualization for SARAS-O at 14°

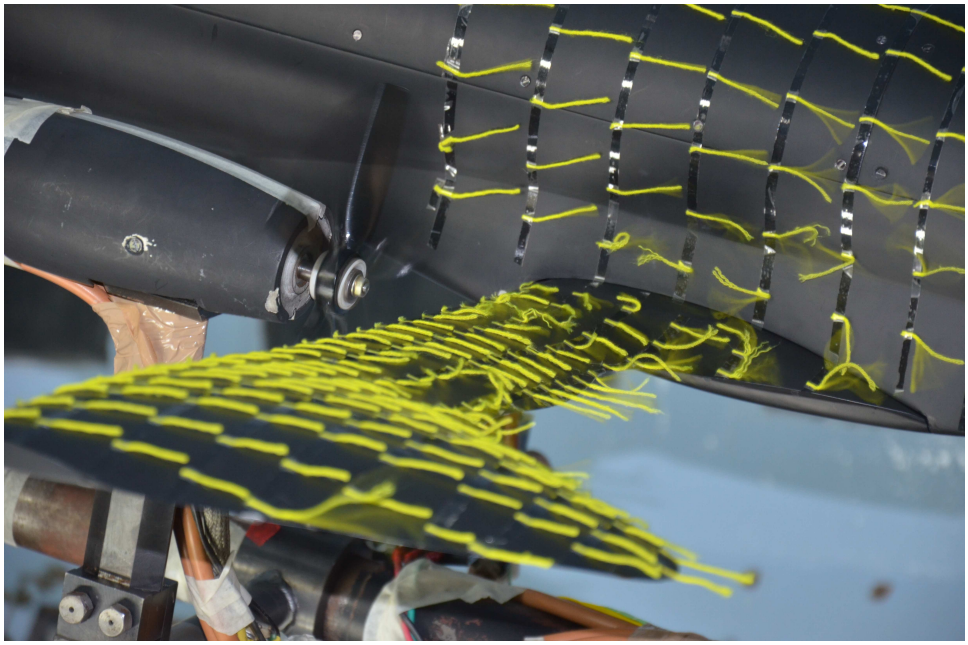

Figure 6.35: Flow visualization for SARAS-O at 14° (zoomed view)

Chapter 7
Conclusion

This thesis has focussed on designing optimal wings for aircraft driven by propellers/rotors in tractor configuration, by modifying the classical lifting-line theory and coupling it to an optimiser. Detailed conclusions have already been provided at the end of each chapter. Herein a summary is provided with suggestions for possible future work.

The optimization problem was formulated in chapter 3. The classical lifting-line theory was modified to account for time averaged propeller slipstream velocities (axial, tangential). An in-house code, PROWING, was developed which coupled the modified lifting-line theory to a constrained optimiser, *fmincon*, available in MATLAB. To obtain smooth wing shapes, the chord and twist distribution of the wing were parameterised using Bézier curves, and the Bézier modes were used as the control variables in the optimization process. The algorithmic implementation was checked using standard test cases. Optimal wing shapes for various cost functions and constraints were generated and are reported in chapter 4.

To check for the scientific robustness of the optimiser, CFD simulations were performed and the results are reported in chapter 5. An in-house Euler code with propeller handling capabilities (PROP-EULER) was developed for the purpose. The propeller was modelled as a rotating actuator disc with distributed sources of axial and angular momentum. The corresponding source densities were estimated using blade-element theory, based on the aerodynamic and geometric characteristics of the propeller blades. The code was validated using standard test cases and was used to solve for the flow over selected optimal wings computed in chapter 4. The results obtained using PROP-EULER and PROWING differed by around 1-2% in induced drag. Thus the high fidelity CFD simulations have confirmed the scientific robustnes of the model embedded in PROWING.

Proof-of-concept wind tunnel tests were performed at the IISc 9ft $\times$ 14ft open circuit wind tunnel in collaboration with C-CADD (Centre for Civil Aircraft Design and Development), NAL, Bangalore and the results are reported in chapter 6. Based on the propeller and the aircraft model available at NAL for the wind tunnel tests, optimal wings were generated using PROWING. These wings were then fabricated and both the control and optimal wings were tested. The tests were conducted at chord based Reynolds num-

ber of 0.5×10^6. The drag data at lift coefficients $C_L = 0$ and $C_L = 0.4$ were analysed. The total drag on the aircraft with optimal wing was lower by 15% at $C_L = 0.4$, which is appreciably better than the PROWING predicted reduction of 6.61%. Although the reasons for higher drag reduction are not entirely clear at this stage, preliminary analysis indicates two plausible candidates: (i) the new wing has appreciably lower profile drag, perhaps due to transition effects, and (ii) there is constructive interference from the fuselage. The tests leave no doubt that the optimal wing design proposed here has an improved aerodynamic performance. Investigations to explain the higher drag reduction obtained in the wind tunnel tests are being planned.

Now that the mathematical correctness of PROWING is established, many optimal wing shapes with a variety of constraints can be generated. To make this wings into reality much more detailed engineering studies have to be carried out and the aerodynamic benefits of the wing shapes must be carefully assessed from a multi-disciplinary view point, including in particular structural parameters and manufacturing technology. The wings with curved trailing edges proposed here should be easier to manufacture with composite materials. Such studies are being carried out currently. An intriguing question concern the fact that drag reduction measured in the wind tunnel tests is higher than predicted. Further numerical and wind tunnel tests are being planned to identify the cause.

An international search report (Restrick 2011) on a draft patent (Narasimha *et al.* 2010) based on the findings of this thesis declared that a wing design having shorter chords in the propeller slipstream and longer chords on either side, as described in this thesis, is the first of its kind as determined from a search carried out in the scientific literature and patent prior art. An Indian patent was filed on 3$^{\text{rd}}$ July 2009, and international patents filed on 5$^{\text{th}}$ July 2010.

Appendix A
Bézier Curves

A brief discussion on Bézier curves is presented in this appendix (http://www.tsplines.com .). These curves are named after Pierre Bézier, working at Renault car company, who invented the curves in the 1960's for design of automobile bodies and surfaces.

To appreciate the special characteristics of Bézier curves, we consider 4 points P_i, $i = 0...3$ as shown in fig. A.1. Each point i has an associated weight w_i, $i = 0...3$. The centre of mass P of these four points is given by

$$P = \frac{\sum_{i=0}^{3} w_i p_i}{\sum_{i=0}^{3} w_i} \tag{A.1}$$

Now suppose the individual weights are assumed to vary as some function of a parameter t, for example by the Bernstein polynomials, $w_0 = 1 - t^3$, $w_1 = 3t(1 - t^2)$, $w_2 = 3t^2(1 - t)$ and $w_3 = t^3$. The variation of these weights for a variation of t between 0 and 1 is shown in fig. A.2. The curve swept by the centre of mass P, shown in fig. A.3, as t varies between 0 to 1, is known as a Bézier curve. When $t = 0$, $w_0 = 1$ and $w_1 = w_2 = w_3 = 0$. This forces the curve to pass through P_0. Also, when $t = 1$, $w_3 = 1$ and $w_0 = w_1 = w_2 = 0$. This forces the curve to pass through P_3. Furthermore, the curve is tangent to the line joining P_0-P_1 and P_2-P_3 and does not pass through all the points. These interesting properties help in getting smooth shapes. This curve is cubic as the weights are cubic polynomials in t. The weights are known as blending functions. In the case of Bézier curves these blending functions are taken as the Bernstein polynomials.

A degree n Bézier curve will have $n + 1$ control points whose blending functions are the Bernstein polynomials as $B_i^n(t)$, given by

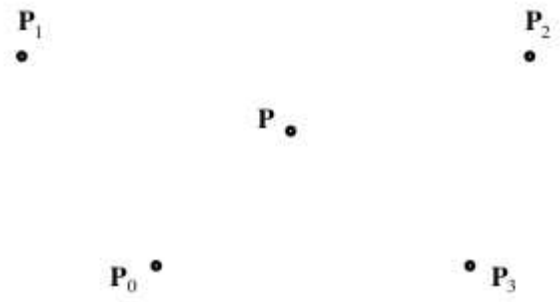

Figure A.1: Four points distributed in a parameter t space with a centre of mass P. Source:(http://www.tsplines.com .)

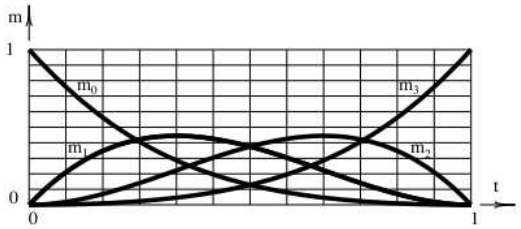

Figure A.2: Variation of masses with t, $0 \leq t \leq 1$. Source:(http://www.tsplines.com .)

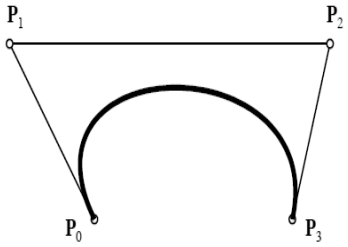

Figure A.3: Cubic Bézier curve. Source:(http://www.tsplines.com .)

$$B_i^n(t) = \binom{n}{i}(1-t)^{n-i}t^i,\ i = 0...n \tag{A.2}$$

The equation for a Bézier curve can now be written as

$$P(t) = \sum_{i=0}^{n} B_i^n(t)P_i \tag{A.3}$$

Fig. A.4 shows a sample of Bézier curves with degrees 1 to 4.

Let us now consider a rectangular wing of aspect ratio $\mathcal{R}$, span b and chord c. If we

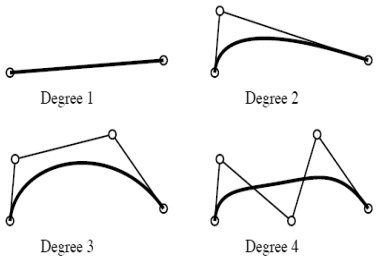

Figure A.4: Bézier curves of degrees 1 - 4. Source:(http://www.tsplines.com .)

take n Bézier modes (in the current work, the masses are called Bézier modes) at equally spaced stations along the span, then the chord at any station y along the span is given by

$$c(y) = \sum_{i=0}^{n} B_i^n(y) w_i \tag{A.4}$$

where w_i is the Bézier mode.

One special property of a Bézier curve is what is called 'variation-diminishing'; i.e. a line drawn through a Bézier curve will intersect it at number of points that is less than or at most equal to the number of intersections with the control polygon. This property is of importance in the present work, and is responsible for the 'smoothness' of the trailing edges in optimal wing designs.

References

Anil, N. 2008 Optimal control of numerical dissipation in modified kfvs (m-kfvs) using discrete adjoint method. PhD thesis, Dept. of Aerospace Engg., IISc, Bangalore, India.

Butterworth-Hayes, P. 2010 Open rotor research revs up. *Aerospace America* pp. 38–42.

Clancy, L. J. 1975 *Aerodynamics*. PITMAN.

Conway, J. T. 1995 Analytical solutions for the actuator disk with variable radial distribution of load. *J. Fluid Mech.* **297**, 327–355.

Deshpande, S. M. 1986 A second order accurate kinetic theory based method for inviscid compressible flows. *NASA Technical Paper* .

Drela, M. & Giles, M. B. 1987 Viscous-inviscid analysis of transonic and low reynolds number airfoils. *AIAA Journal* **25**, 1347–1355.

Farin, G. 2002 *Curves and Surfaces for CAGD*. Academic Press.

Fejer, A. 1945 Lifting line theory in linearly varying flow. PhD thesis, California Institute of Technology.

FLUENT 2003 Fluent 6.3 udf manual. *Fluent Inc. Software* .

GAMBIT 2004 Gambit 2.1 documentation, user's guide. *Fluent Inc. Software* .

Ghosh, A. K., Mathur, J. S. & Deshpande, S. M. 1998 q-kfvs scheme - a new higher order kinetic method for euler equations. *16th International Conference on Numerical Methods in Fluid Dynamics, Lecture Notes in Physics* **515**.

Glauert, H. 1926 *"The Monoplane Aerofoil", The Elements of Aerofoil and Airscrew Theory*. Cambridge University Press, U.K.

Hartman, E. & Biermann, P. D. 1938 The aerodynamic characteristics of full-scale propellers having 2, 3, and 4 blades of Clark Y and R.A.F. 6 airfoil sections. *NACA-report-640* .

Hough, G. R. & Ordway, D. E. 1965 Developments in theoretical and applied mechanics. *Pergamon* **2**, 317–336.

http://www.mathworks.co.uk/help/optim/ug/fmincon.html . fmincon.

http://www.tsplines.com . Bézier curves.

Iglesias, S. & Mason, W. H. 2001 Optimum spanloads incorporating structural weight. *AIAA-5234* .

Jameson, A. 1969 The analysis of propeller-wing flow interaction. *NASA symposium proceedings* pp. 721–749.

Jameson, A. & Yoon, S. 1986 Lower upper implicit schemes with multiple grids for the euler equations. *AIAA* .

Jones, R. T. 1950 Lift for minimum induced drag of wings having given lift and root bending moment. *NACA TN-2249* .

Josy, P. 2009 Propeller slipstream velocities. Private communication.

Karman, T. V. & Tsien, H.-S. 1945 Lifting-line theory for a wing in non-uniform flow. *Ouarterly of Applied Mathematics* pp. 1–11.

Karypis, G. & Kumar, V. 1998 A software package for partitioning unstructured graphs, partitioning meshes and computing fill-reducing order of sparse matrices. *University of Minnesota, Dept. of Computer Science / Army HPC Research Centre* .

Koning, C. 1935 Influence of the propeller on other parts of the airplane structure. *Ed. by Durand, W. F., Aerodynamic Theory* **4**, 361–430.

Kota, H. & Satish, C. 2009 Enhanced regional air transportation in india needs issues and challenges. *Journal of Aerospace Sciences and Technologies* **61**, 32–41.

Kroo, I. 1986 Propeller-wing integration for minimum induced loss. *J. Aircraft* **23**, 561–565.

Lötstedt, P. 1995 Accuracy of a propeller model in inviscid flow. *J. Aircraft.* **32**, 1312–1321.

MATLAB 2007 The Mathworks Inc.

Narasimha, R., Deshpande, S. M., Chandrashekarappa, P. & Rakshith, B. R. 2010 Optimal wing planforms for reducing the induced or total drag of the wing of an aircraft driven by wing-mounted tractor propellers/rotors. *International Patent Application* **PCT/IN2010/000448**.

Narayan, K. Y. 2009 Saras wing geometry details. Private communication.

Panda, G. K., Prabhu, V., Rajendra, G. & Narayan, K. Y. 2012 An experimental investigation of a turboprop wing optimized with propeller slipstream effect included. *NAL PD CA 1204* .

Pierre, S. 2008 Give turboprops their due. *Aviation Week and Space Technology* p. 41.

Prandtl, L. 1918 Theory of lifting surfaces. *NACA TN (From Tech. Ber.)* **9**.

Prandtl, L. 1921 Mutual influence of wings and propeller. *NACA TN No. 74.* .

Praveen, C. 2004 Development and application of kinetic meshless methods for euler equations. PhD thesis, Dept. of Aerospace Engg., IISc, Bangalore, India.

Rajagopalan, R. G. 1989 A numerical study of a wing and propeller in mutual interference. *AIAA* pp. 464–471.

Restrick, K. 2011 Australian patent office. *International Search Report and Written Opinion on Application No. PCT/IN2010/000448* .

Rethorst, S. 1958 Aerodynamics of nonuniform flows as related to an airfoil extending through a circular jet. *Journal of the Aeronautical Sciences* pp. 11–28.

Robert, W. 2011 Aeronautical astigmatism. *Aviation Week and Space Technology* p. 38.

Roosenboom, E. W. M., Stürmer, A. & Schröder, A. 2010 Advanced experimental and numerical validation and analysis of propeller slipstream flows. *J. Aircraft* **47**, 284–291.

Schmitt, V. & Charpin, F. 1979 ressure distributions on the onera m6 wing at transonic mach numbers. *AGARD-AR-138* .

Veldhuis, L. L. M. 2005 Propeller wing aerodynamic interference. PhD thesis, Delft University.

Veldhuis, L. L. M. & Heyma, P. M. 1998 A simple wing optimization code including propeller effects. *Congress of International Council of the Aeronautical Sciences* pp. 13–18.

Veldhuis, L. L. M. & Heyma, P. M. 2000 Aerodynamic optimisation of wings in multi-engined tractor propeller arrangements. *Aircraft Design* pp. 129–149.

Wakayama, S. & Kroo, I. 1995 Subsonic wing planform design using multidisciplinary optimization. *Journal of Aircraft* **32**.

Whitfield, D. L. & Jameson, A. 1983 Three-dimensional euler equation simulation using euler equations. *AIAA* .

Witkowski, D. P., Lee, A. K. H. & Sullivan, J. P. 1989 Aerodynamic interaction between propellers and wings. *J. Aircraft* **26**, 829–836.